

# GRAVITY DRIVEN CHEMICAL DYNAMICS IN FRACTURES

by

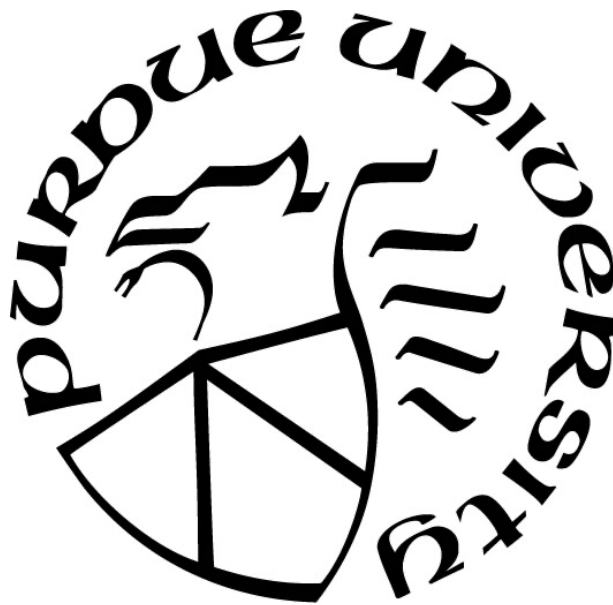
Zhenyu Xu

**A Dissertation**

*Submitted to the Faculty of Purdue University*

*In Partial Fulfillment of the Requirements for the degree of*

**Doctor of Philosophy**



Department of Physics and Astronomy

West Lafayette, Indiana

December 2020

**THE PURDUE UNIVERSITY GRADUATE SCHOOL  
STATEMENT OF COMMITTEE APPROVAL**

**Dr. Laura J. Pyrak-Nolte, Chair**

Department of Physics and Astronomy

**Dr. Paul F. Muzikar**

Department of Physics and Astronomy

**Dr. Oana Malis**

Department of Physics and Astronomy

**Dr. Ken Ritchie**

Department of Physics and Astronomy

**Approved by:**

Dr. John P. Finley

*To my parents*

## ACKNOWLEDGMENTS

This work was supported as part of the Center for Nanoscale Controls on Geologic CO<sub>2</sub> (NCGC), an Energy Frontier Research Center funded by the U.S. Department of Energy, Office of Science, Basic Energy Sciences under Award # DE-AC02-05CH11231.

I would also like to express my deepest gratitude to my advisor, Professor Pyrak-Nolte. Her passion on research, patience in guidance brought me into the rock physics area. She walked me through all of the challenges for these years. I not only received strict scientific training on research, but also became a better person under the influence of her.

Thanks to Qingyun, Mario and Chaoyi for their expertise in experiments. I obtained huge direct help and inspiration from them. Wish I could meet them earlier.

Thanks to my labmates for the discussions, support and encouragement.

Thanks to the secretaries (especially Sandy) for helping me with hassles so I could focus on research.

# TABLE OF CONTENTS

LIST OF TABLES.....	8
LIST OF FIGURES .....	9
ABSTRACT.....	15
CHAPTER 1. BACKGROUND INTRODUCTION.....	16
CHAPTER 2. EXPERIMENTAL METHODS .....	28
2.1 Fluid Components and Chemistry .....	28
2.1.1 Mineral Precipitation from Miscible Reactive Flow.....	28
2.1.2 Non-reactive Miscible Fluids .....	30
2.1.3 Precipitates Composed of CaCO <sub>3</sub> Powder and Water.....	31
2.2 Sample Description .....	32
2.2.1 Variable Aperture Fracture.....	32
2.2.2 Uniform Aperture Fracture.....	33
2.2.3 Fracture Composed of Rough Surface in Contact with a Flat Surface .....	35
2.2.4 3D Printed Uniform Aperture .....	36
2.3 Fluid Pumping System .....	37
2.4 Digital Imaging of Fracture .....	37
2.5 Pixel Edge Length Calibration .....	38
2.6 Acoustic Monitoring.....	38
2.6.1 System Calibration .....	40
2.7 Precipitation Analysis.....	45
2.8 X-ray CT Scan.....	46
CHAPTER 3. GRAVITY DRIVEN CHEMICAL DYNAMICS IN FRACTURES.....	47
3.1 Introduction .....	47
3.2 Non-reactive Mixing in a Variable Aperture Fracture .....	50
3.3 Mixing of Miscible Fluids in a Uniform Aperture Fracture.....	51
3.3.1 Influence of Inclination Angle .....	52
3.3.1.1 Mixing of Non-reactive Miscible Fluids in a Uniform Aperture Fracture.....	52
3.3.1.2 Reactive Mixing of Miscible Fluids in a Uniform Aperture Fracture.....	63
3.3.2 Influence of Aperture .....	72

3.3.2.1	Mixing of Non-reactive Miscible Fluids in a Uniform Aperture Fracture.....	72
3.3.2.2	Reactive Mixing of Miscible Fluids in a Uniform Aperture Fracture.....	78
3.3.3	Influence of Density Contrast .....	79
3.3.3.1	Mixing of Non-reactive Miscible Fluids in a Uniform Aperture Fracture.....	79
3.3.3.2	Reactive Mixing of Miscible Fluids in a Uniform Aperture Fracture.....	84
3.3.4	Influence of Pumping Rate.....	87
CHAPTER 4.	SEISMIC RESPONSE TO $\text{CaCO}_3$ PRECIPITATION IN SYNTHETIC FRACTURES .....	92
4.1	Introduction .....	92
4.2	Simulation Results.....	92
4.2.1	Model Verification on One Solid Uniform Block with Different Properties.....	93
4.2.2	Two Solid Uniform Blocks with Different Properties .....	97
4.2.3	Four Layer Model Representing a Mineral-Filled Fracture in a Rock Matrix.....	100
4.3	Experiment results .....	107
4.3.1	A Uniform Aperture Fracture Filled with $\text{CaCO}_3$ Powder and Water .....	107
4.3.2	Reactive Mixing in a Uniform Aperture Fracture.....	107
4.3.3	Pore-filling Precipitation in a Variable Aperture Fracture.....	109
4.3.4	Surface adhering Precipitation in a Variable Aperture Fracture .....	113
CHAPTER 5.	CONCLUSION AND FUTRUE WORK.....	117
APPENDIX A.	WAVE PROPAGATION THEORY .....	120
A.1	Wave Propagation in Elastic Material.....	120
A.1.1	Boundary Conditions.....	121
Welded Boundaries .....		121
Solid-Fluid Boundaries .....		122
Free Surface.....		122
Non-Welded Boundaries .....		122
A.2	Reflection and Transmission of Plane Waves on Different Interface .....	123
A.2.1	SH Wave Incident on a Welded Interface.....	123
A.2.2	SH Wave Incident on a Solid-Fluid Interface .....	125
A.2.3	P-SV Wave Incident on a Welded Interface .....	125
A.2.4	P-SV Wave Incident on a Solid-Fluid Interface.....	128

A.3	Reflection and Transmission of Plane Waves in a Layered System .....	129
A.4	SH Wave Propagation in a Layered System.....	131
A.5	P-SV Wave Propagation in a Layered System .....	132
APPENDIX B. IMAGES SHOWING EXPERIMENT REPEATABILITY .....		136
APPENDIX C. OTHER MEASUREMENTS OF FLUIDS PROPERTIES .....		140
REFERENCES .....		142

## LIST OF TABLES

Table 2.1 Solutions for pore filling precipitation.....	29
Table 2.2 Solutions for surface adhering precipitation.....	29
Table 2.3 Solutions for uniform aperture precipitation experiment .....	30
Table 2.4 Solutions for miscible non-reactive fluids mixing.....	31
Table 2.5 Solutions for miscible non-reactive fluids mixing for density contrast.....	31
Table 2.6 Properties of the solidified urethane .....	33
Table 2.7 Properties of the flat polycarbonate sheet.....	34
Table 2.8 Properties of cured 3D printing FLGPBL04 black resin .....	36
Table 3.1 Parameters for studying influence of rough fracture. ....	50
Table 3.2 Component of fluids for color calibration in terms of concentration of Solution 1 .....	58
Table 3.3 Parameters for studying influence of inclination angle. ....	63
Table 3.4 pH indicator color change range.....	63
Table 3.5 Area of blue precipitation .....	67
Table 3.6 Parameters for studying influence of aperture.....	72
Table 3.7 Table of dimensionless numbers.....	77
Table 3.8 Parameters for studying influence of density contrast.....	79
Table 3.9 Width of less dense fluid runlet for different density contrast. ....	83
Table 3.10 Parameters for studying influence of density contrast.....	84
Table 3.11 Parameters for studying influence of pumping rate.....	87
Table 4.1 Parameters for studying influence of matrix properties.....	96
Table 4.2 Transmitted signal maximum amplitude. ....	97
Table 4.3 Transmitted signal maximum amplitude. ....	98
Table 4.4 Parameters for studying influence of matrix properties.....	100
Table 4.5 Parameters for studying influence of precipitate thickness. ....	103
Table A.1 Displacement for incident and scattered waves [28]. ....	125
Table C.1 Component and viscosity measurement of different solutions .....	140
Table C.2 Component and interface tension measurement of different solutions .....	141

## LIST OF FIGURES

Figure 1.1 Comparison of the three types of mineral precipitation patterns at two different time instants. Precipitates preferentially formed (a) from the lower tip; (b) near the inlet and exit region of the fracture; (c) throughout the entire fracture. (From Zhao et al [12]).	20
Figure 1.2 Sketch of displacement of one fluid by a second fluid in a horizontal rectangular channel.	23
Figure 1.3 (left) Flow mixing in different $Rv/g$ in 2D model; (right) Flow mixing in different $Rv/gz$ in 3D model (Cross section of $y=16$ ).	24
Figure 1.4 Influences of $Re$ and $Sc$ on fluid mixing.	26
Figure 1.5 Less dense fluid displacing denser fluid.	26
Figure 1.6 Denser fluid displacing less dense fluid.	26
Figure 2.1 Scanning electron microscope (SEM) image of (left) pore filling precipitates; (right) surface adhering precipitates.	29
Figure 2.2 Casted poly-urethane fracture sample.	33
Figure 2.3 (a) Casted urethane uniform aperture fracture sample; (b) acrylic uniform aperture fracture sample.	35
Figure 2.4 Fracture composed of rough surface in contact with a flat surface.	35
Figure 2.5 3D printed uniform aperture sample.	36
Figure 2.6 Image of the camera and easel.	38
Figure 2.7 Air Force Test Chart used to calibrate the pixel edge length.	38
Figure 2.8 Sketch of experimental set-up.	39
Figure 2.9 Sketch of experimental set-up.	40
Figure 2.10 Sketch of transducer layout for system calibration.	41
Figure 2.11 Maximum amplitude of transmitted signal as a function of time for (a) horizontal and (b) vertical transducer set when there are only transducers.	41
Figure 2.12 Sketch of transducer layout for system calibration with small block sample with a borehole.	42
Figure 2.13 Maximum amplitude of transmitted signal as a function of time for horizontal (red) and vertical (blue) transducer set when a cubic poly-urethane block (49mm*49mm*40mm) with a dry borehole (3mm diameter) was placed between the 2 sets of transducers inside the water tank.	42

Figure 2.14 Maximum amplitude of transmitted signal as a function of time for horizontal (red) and vertical (blue) transducer set when a cubic poly-urethane block (49mm\*49mm\*40mm) with a dry borehole (3mm diameter) and saturated for 17 hours was placed between the 2 sets of transducers inside the water tank. .... 43

Figure 2.15 Maximum amplitude of transmitted signal as a function of time for horizontal (red) and (blue) vertical transducer set when a cubic poly-urethane block (49mm\*49mm\*40mm) with a borehole (3mm diameter) which was saturated with Na<sub>2</sub>CO<sub>3</sub> solution was placed between the 2 sets of transducers inside the water tank. .... 44

Figure 2.16 Maximum amplitude of transmitted signal as a function of time for horizontal (red) and vertical (blue) transducer set when a cubic poly- urethane block (49mm\*49mm\*40mm) with a borehole (3mm diameter) which was saturated with Na<sub>2</sub>CO<sub>3</sub> solution for 20 hours was placed between the 2 sets of transducers inside the water tank. .... 45

Figure 3.1 Precipitate distribution for (a) vertical normal order pore-filling; (b) vertical reverse order pore-filling; (c) vertical normal order surface-adhering; (d) vertical reverse order surface-adhering; (e) horizontal normal order pore-filling; (f) horizontal reverse order pore-filling; (g) horizontal normal order surface-adhering; (h) horizontal reverse order surface-adhering. .... 48

Figure 3.2 Gray scale image of non-reactive mixing in fracture composed of rough surface in contact with a flat surface. .... 51

Figure 3.3 (left) Digital images from non-reactive miscible fluid mixing experiments. (right) Processed images from non-reactive miscible fluid mixing experiments. Fluids have been represented with 5 range concentration of Solution 1: Yellow: <25%; Orange: 25%-50%; Olive: 50%-75%; Cyan: 75%-100%; Blue:~100%. Each row shows images from a different fracture inclination angle (15°- 90°). Each column represents different times during the experiments (25, 50, 75, 167 and 250 mins after start pumping both fluids). Aperture is 2 mm; pumping rate is 0.17 ml/min for both Solution 1 and 2; density contrast is 1111/1031.8. .... 53

Figure 3.4 Comparison of runlet geometry from the invasion of nonreactive miscible fluids in fractures inclined at 15° to 90° for T=250 minutes after the simultaneous invasion of two fluids. Aperture is 2 mm; pumping rate is 0.17 ml/min for both Solution 1 and 2; density contrast is 1111/1031.8. .... 55

Figure 3.5 Area of runlets as a function of angles of inclination. The blue points represent the mean area with an error bar of standard error of mean (SEM). Red line is the fitted curve. Aperture is 2 mm; pumping rate is 0.17 ml/min for both Solution 1 and 2; density contrast is 1111/1031.8.... 55

Figure 3.6 Values of space between the ripples at angles 15° to 90° at T=83.33 minutes and T=250 minutes. Aperture is 2 mm; pumping rate is 0.17 ml/min for both Solution 1 and 2; density contrast is 1111/1031.8. .... 57

Figure 3.7 Fracture area fraction of different concentration fluids in terms of Solution 1 by weight over time for different inclination angles. Aperture is 2 mm; pumping rate is 0.17 ml/min for both Solution 1 and 2; density contrast is 1111/1031.8. .... 59

Figure 3.8 Fracture Area Fraction at T=250 minutes for different inclination angles. Aperture is 2 mm; pumping rate is 0.17 ml/min for both Solution 1 and 2; density contrast is 1111/1031.8.... 60

Figure 3.9 (a) Fluids mixing in a horizontal fracture (inclination angle  $0^\circ$ ); (b) Fluids mixing in a vertical fracture (inclination angle  $90^\circ$ ); (c) Fluids mixing in a fracture with an inclination angle between  $0^\circ$  and  $90^\circ$ ..... 62

Figure 3.10 Images of reactive miscible fluids mixing with different angles of inclination at time  $T=25, 50, 75, 167, 250$  minutes. Aperture is 2 mm; pumping rate is 0.17 ml/min for both Solution 1 and 2; density contrast is 1111/1031.8..... 66

Figure 3.11 Fracture Area Fraction of precipitate amount change over time relative to the time when reaction front reached the entire fracture plane. Aperture is 2 mm; pumping rate is 0.17 ml/min for both Solution 1 and 2; density contrast is 1111/1031.8..... 67

Figure 3.12 Fracture Area Fraction of precipitate amount change in the end of experiments for different inclination angles. Aperture is 2 mm; pumping rate is 0.17 ml/min for both Solution 1 and 2; density contrast is 1111/1031.8..... 69

Figure 3.13 (a)-(f) Unprocessed images of precipitation for  $\theta=60^\circ$ . (g)-(l) Area of precipitation change relative to reference image for  $\theta=60^\circ$  in three colors. White means the area with less precipitation compared to reference image. Purple means the amount of precipitation on the area is unchanged. Yellow means the area with more precipitation. (a) (g) Time=104.17 minutes; (b) (h) Time=166.67 minutes; (c) (i) Time=197 minutes and 25 seconds; (d) (j) Time=197 minutes and 30 seconds;(e) (k)Time=197 minutes and 35 seconds;(f) (l) Time=250 minutes. Aperture is 2 mm; pumping rate is 0.17 ml/min for both Solution 1 and 2; density contrast is 1111/1031.8.... 71

Figure 3.14 (a) Digital images from non-reactive miscible fluid mixing experiments (b) Processed images from non-reactive miscible fluid mixing experiments. Fluids have been represented with 5 range concentration of Solution 1: Yellow: <25%; Orange: 25%-50%; Olive: 50%-75%; Cyan: 75%-100%; Blue:~100%. Each row shows images from a different aperture. Each column represents different times during the experiments (25, 50, 75, 167 and 250 mins after start pumping both fluids). Inclination angle is  $90^\circ$ ; pumping rate is 0.17 ml/min for both Solution 1 and 2; density contrast is 1111/1031.8. .... 73

Figure 3.15 Fracture area fraction of different concentration fluids in terms of Solution 1 by weight over time for different apertures. Inclination angle is  $90^\circ$ ; pumping rate is 0.17 ml/min for both Solution 1 and 2; density contrast is 1111/1031.8. .... 74

Figure 3.16 Fracture Area Fraction at  $T=250$  minutes for different apertures. Inclination angle is  $90^\circ$ ; pumping rate is 0.17 ml/min for both Solution 1 and 2; density contrast is 1111/1031.8. .... 75

Figure 3.17 Shape of less dense fluid at different aperture and pump rate of Solution 2. Inclination angle is  $90^\circ$ ; pumping rate of Solution 1 is 0.17 ml/min  $\blacklozenge$ ; density contrast is 1111/1031.8. .... 77

Figure 3.18 Precipitate distribution in horizontal fracture (inclination angle  $\theta=0^\circ$ )with different apertures: (a) 0.5mm; (b) 1mm; (c) 2mm. and in vertical fracture (inclination angle  $\theta=90^\circ$ ) with different apertures: (d) 0.5mm; (e) 1mm; (f) 2mm. .... 78

Figure 3.19 (left) Digital images from non-reactive miscible fluid mixing experiments. (right) Processed images from non-reactive miscible fluid mixing experiments. Fluids have been represented with 5 range concentration of Solution 1: Yellow: <25%; Orange: 25%-50%; Olive: 50%-75%; Cyan:75%-100%; Blue:~100%. Each row shows images from a different density contrast. Each column represents different times during the experiments (25, 50, 75, 167 and 250 mins after start pumping both fluids). Inclination angle is 90°; aperture is 2 mm; pumping rate is 0.17 ml/min for both Solution 1 and 2.....	80
Figure 3.20 Fracture area fraction of different concentration fluids in terms of Solution 1 by weight over time for different density contrast. Inclination angle is 90°; aperture is 2 mm; pumping rate is 0.17 ml/min for both Solution 1 and 2.....	81
Figure 3.21 Fracture Area Fraction at T=250 minutes for different density contrast. Inclination angle is 90°; aperture is 2 mm; pumping rate is 0.17 ml/min for both Solution 1 and Solution 2.	82
Figure 3.22 Less dense fluid runlet of different density contrast. Inclination angle is 90°; aperture is 2 mm; pumping rate is 0.17 ml/min for both Solution 1 and 2.....	83
Figure 3.23 Different stages of the uniform aperture fracture precipitation after start pumping both solutions for $\rho_1/\rho_2=1.07$ : (a) 800s; (b) 1600s; (c) 2000s; (d) 19440s; for $\rho_1/\rho_2=1.04$ : (e) 800s; (f) 1600s; (g) 2400s; (h) 19440s; for $\rho_1/\rho_2=1$ : (i) 480s; (j) 600s; (k) 1240s; (l) 19440s. Inclination angle is 90°; aperture is 2 mm; pumping rate is 0.17 ml/min for both Solution 1 and 2.....	85
Figure 3.24 (left) Digital images from non-reactive miscible fluid mixing experiments. (right) Processed images from non-reactive miscible fluid mixing experiments. Fluids have been represented with 5 range concentration of Solution 1: Yellow: <25%; Orange: 25%-50%; Olive: 50%-75%; Cyan:75%-100%; Blue:~100%. Each row shows images from different pumping rates of Solution 2. Each column represents different times during the experiments (25, 50, 75, 167 and 250 mins after start pumping both fluids). Inclination angle is 90°; aperture is 2 mm; pumping rate is 0.17 ml/min for Solution 1; density contrast is 1111/1031.8. The case of 1.36ml/min pumping rate missing last image because it ran out of fluid due to the size limit of syringe (300 ml). .....	88
Figure 3.25 Fracture area fraction of different concentration fluids in terms of Solution 1 by weight over time for different pumping rates of Solution 2. Inclination angle is 90°; aperture is 2 mm; pumping rate is 0.17 ml/min for Solution 1; density contrast is 1111/1031.8.....	89
Figure 3.26 Fracture Area Fraction at T=250 minutes for different pumping rate of Solution 2. Aperture is 2 mm; pumping rate is 0.17 ml/min for Solution 1; density contrast is 1111/1031.8.	90
Figure 4.1 (a) One solid block model; (b) Two solid uniform blocks model; (c) Two solid uniform blocks form 3 layers model; (d) Four-layer model. ....	95
Figure 4.2 (left) Density's influence on transmitted signal in one-layer medium; (right) Acoustic velocity's influence on transmitted signal in one-layer medium. ....	95
Figure 4.3 Thickness' influence on transmitted signal in one-layer medium. ....	96
Figure 4.4 Transmitted signal as a function of density of block 2. The density of block 1 was set to 3000 kg/m <sup>3</sup> and the wave velocity of block 1 and 2 are 4000 m/s. ....	99
Figure 4.5 Transmitted signal as a function of properties of block 2 for impedance matching. The density of block 1 is 3000 kg/m <sup>3</sup> and wave velocity of block 1 is 4000 m/s.....	99

Figure 4.6 Critical lines for maximum amplitude of transmitted signals as a function of matrix material (red line overlaps the black line). The lines show the boundary between transmitted amplitude that is smaller and larger than the amplitude of the input signal. ....	101
Figure 4.7 Trend of transmitted waveform change with matrix material's properties. Blue signal is for $V_p(\text{matrix material})=1100$ m/s. Red signal is for keeping $V_p(\text{matrix material})=1100$ m/s while increasing $\rho(\text{matrix material})$ . Black signal is for increasing $V_p(\text{matrix material})$ while keeping $\rho(\text{matrix material})$ unchanged. ....	102
Figure 4.8 Transmitted signals for water saturated (blue), 0.2 mm thickness of precipitate filled (red) and 0.4 mm thickness of precipitate (black) in a 0.5 mm fracture. ....	103
Figure 4.9 Transmitted signals for water saturated (blue), 0.3 mm thickness of precipitate filled (red) and 0.9 mm thickness of precipitate filled (black) 1 mm fracture. ....	104
Figure 4.10 Transmitted signals for water saturated (blue), 0.6 mm thickness of precipitate filled (red) and 1.4 mm thickness of precipitate filled (black) 1.5 mm fracture. ....	105
Figure 4.11 Normalized maximum amplitude of transmitted signal as a function of normalized thickness of fracture. ....	105
Figure 4.12 Transmitted signal through black resin-water-black resin and black resin- $\text{CaCO}_3$ powder and water mixture-black resin samples. ....	107
Figure 4.13 Sketch of (a) direct wave transmission through layers of media; (b) transmission wave with once reflection on the fracture .....	108
Figure 4.14 Comparison between experimental signal and simulated signal. ....	108
Figure 4.15 X-ray CT scan of mineral precipitation formed in the uniform aperture fracture. .	109
Figure 4.16 Transducer layout. ....	109
Figure 4.17 Individual signals during the saturation period (blue), reaction period (red) and the end of the experiment (black) of the pore-filling precipitation for transducer 2 and 9 in normal order (a) (c) vertical and (b) (d) horizontal fracture, and pore-filling precipitation for transducer 2 and 9 in reverse order (e) (g) vertical and (f) (h) horizontal fracture, respectively. ....	110
Figure 4.18 Maximum amplitude of transmitted signals as a function of time for transducer 2 for (a) normal order pore-filling precipitation and (b) reverse order pore-filling precipitation. ....	112
Figure 4.19 Individual signals during the saturation period (blue), reaction period (red) and the end of the experiment (black; pink in(a)) of the normal order surface adhering precipitation for transducer 2 and 9 in (a) (c) vertical and (b) (d) horizontal fracture, respectively. ....	113
Figure 4.20 FFT of the signals at normal order surface-adhering experiment for transducer 2. The frequency components are corresponding to Figure 4.19 (a). ....	115
Figure 4.21 Maximum amplitude of transmission signals as a function of time for transducer 2 for (a) normal order surface adhering precipitation and (b) reverse order surface adhering precipitation. ....	115
Figure 5.1 Sketch of the boundary. ....	121

Figure A.1. Notation for the four possible reflection/transmission coefficients for incident SH-wave (redraw from [28]).	123
Figure A.2 The complete system of incident and scattered plane P-SV waves, in terms of which the scattering matrix can quickly be found. Short arrows show the direction of particle motion; long arrows show the direction of propagation (redraw from [28]).	126
Figure A.3 Incident and scattered plane waves across two half spaces and one welded interface.	129
Figure A.4 Waves travel through the medium.	130
Figure A.5 Complete components for possible incident P-SV waves with reflection and transmission.	132
Figure B.1 Fracture area fraction of different concentration fluids in terms of Solution 1 by weight over time for different inclination angles. Aperture is 2 mm; pumping rate is 0.17 ml/min for both Solution 1 and 2; density contrast is 1111/1031.8.	137
Figure B.2 Fracture area fraction of different concentration fluids in terms of Solution 1 by weight over time for different apertures. Inclination angle is 90°; pumping rate is 0.17 ml/min for both Solution 1 and 2; density contrast is 1111/1031.8.	138
Figure B.3 Fracture area fraction of different concentration fluids in terms of Solution 1 by weight over time for different pumping rates of Solution 2. Inclination angle is 90°; aperture is 2 mm; pumping rate is 0.17 ml/min for Solution 1; density contrast is 1111/1031.8.	139
Figure C.1 CSC Scientific Tensiometer-Du Nouy	141

## ABSTRACT

Global warming is considered to result from excessive emission of CO<sub>2</sub> caused by human activity. The security of long term CO<sub>2</sub> capture and sequestration on the subsurface depends on the integrity of caprocks. Natural and engineered subsurface activities can generate fractures in caprocks that can lead to CO<sub>2</sub> leakage. Reactive fluids that flow through a fracture may seal a fracture through mineral precipitation or open a fracture through dissolution. It is extremely useful to CO<sub>2</sub> storage to understand the behavior of reactive fluids that generates mineral precipitation that can seal a fracture. Experiments on non-reactive and reactive fluid mixing were performed to explore gravity-driven chemical dynamics that control the mixing and spatial distribution of mineral precipitates. Fracture inclination, fracture apertures, fluid pumping rates, and density contrasts between fluids were studied for their effects on fluid mixing. From non-reactive fluid mixing experiments, a less dense fluid was found to be confined to a narrow path (runlet) by the denser fluid under the influence of gravity. Fracture inclination angle affected the shape of the less dense fluid runlet. As the angle of inclination decreased, the area of the less dense runlet increased. Improved mixing and a potentially larger area of precipitation formation will occur during reactive fluid mixing when the fracture plane is perpendicular to gravity. Fracture aperture affected the time evolution of the mixing of the fluids, while pumping rate affected fluid mixing by controlling the relative velocities between the two fluids. The fact that the spatial distribution of the two fluids, instead of the fracture roughness, dominated the fluid mixing sheds light on the potential behaviors of reactive fluids mixing in fractures. The location for the majority of precipitation formation and the transport of precipitates can be accordingly predicted from knowledge of the properties of the two reactive fluids and the orientation of the fracture.

From a small study on wave propagation across fractures with precipitates, simulation results showed that the impedance difference between the matrix material and the precipitate affects the transmitted signal amplitude. Both the aperture and fraction of aperture filled with precipitates affect signal amplitude.

## CHAPTER 1. BACKGROUND INTRODUCTION

Global climate change has long been a controversial problem, but the mainstream opinion is that current global warming is a result of large amounts of greenhouse gas (such as CO<sub>2</sub>) emissions [1]. The current CO<sub>2</sub> emission rate is far beyond the natural rate of carbon recycling. One goal of the international agreement on climate change adopted in Paris 2015 is to limit the temperature increase to ‘well below’ 2°C and to pursue ‘efforts’ to limit such an increase to 1.5°C [2]. According to The International Energy Agency (IEA)’s estimate, the world needs to capture and store almost 4,000 million tons per annum (Mtpa) of CO<sub>2</sub> in 2040 to meet the 2°C requirement and will require much more to be stored to achieve 1.5°C. However, by the end of 2016, only 33.9 Mtpa CO<sub>2</sub> were captured and stored by Carbon Capture and Sequestration (CCS) projects globally [3]. The large gap between the needed and actual storage stimulates more and more scientists and engineers to find efficient and economically acceptable ways for CCS.

Methods for CO<sub>2</sub> sequestration and storage can be generally categorized by three processes: biological, physical and chemical [4]. Biological sequestration includes photosynthesis and other methods that rely on a biological body to transfer free CO<sub>2</sub> into a stabilized carbonate. Physical methods usually involving injecting CO<sub>2</sub> into other media such as the sea or underground to trap the CO<sub>2</sub> inside those media. Chemical processes utilizing different material, mainly metal oxide, to react with CO<sub>2</sub> to produce a stabilized carbonate. In practice, these methods are not independent. For example, the dominant method for sequestering CO<sub>2</sub> is subsurface injection. The CO<sub>2</sub> is not only trapped underground, but also interacts with saline aquifers and complicated minerals in the rock units such that it may become stabilized by forming a carbonate mineral.

Recently, the CarbFix site in Iceland [5] showed a successful transfer of CO<sub>2</sub> into carbonate minerals in only 2 years, much faster than the prevailing view that such a transfer would take

hundreds of years. They injected CO<sub>2</sub> mixed with H<sub>2</sub>S (Hydrogen sulfide) and water into a basaltic (composed of SiO<sub>2</sub> (Silicon dioxide), Al<sub>2</sub>O<sub>3</sub> (Aluminum oxide), FeO (Iron(II) oxide), CaO (Calcium oxide), MgO (Magnesium oxide), Fe<sub>2</sub>O<sub>3</sub> (Iron(III) oxide), Na<sub>2</sub>O (Sodium oxide), TiO<sub>2</sub> (Titanium dioxide) etc.) subsurface site, and monitored the conversion process using C14 isotope as the tracer. The mechanism that lead to the success of this trial project is complicated, but is considered to be caused by the dissolution of CO<sub>2</sub> in water, that causes relatively rapid dissolution of basalt and releases metal ions into solution for mineralization, and also the dissolution of pre-existing carbonate minerals onsite, which neutralized the CO<sub>2</sub> enriched water by forming HCO<sub>3</sub><sup>-</sup> (hydrogen carbonate). The success of this project gives hope for a promising future for this CCS method.

Fractures are common in the subsurface, and their presence affects a wide range of subsurface activities such as oil production, geothermal energy production, underground water protection, and also CO<sub>2</sub> sequestration. Fractures in nature can be open, closed, partially or fully sealed from mineral precipitation. Laubach & Ward [6] found that fractures (joints) in Middle Triassic to Lower Jurassic La Boca Formation sandstones, in Northeastern Mexico, were filled with mainly quartz, calcite, ferroan calcite, iron oxides, and barite. The Refugio-Carneos fault in the Santa Barbara Basin of Southern California [7] and the Moab fault around Courthouse Rock and Mill Canyon in Utah [8] also have been observed to contain calcium carbonate precipitation along segments of the faults.

The ability to successfully sequester CO<sub>2</sub> in the subsurface greatly depends on caprock integrity. Caprocks are geological units with extremely low (or zero) permeability that trap fluids in the geological units below the caprock. Open or partially open fractures are potential pathways through a caprock. Geological activity, such as tectonic processes or geochemical reaction and

subsurface engineering activities, can generate new fractures in the caprock. Therefore, mineral precipitation plays dual roles in CCS: sealing the fractures to keep CO<sub>2</sub> from leaking and immobilizing CO<sub>2</sub> by precipitation.

Considering the importance of fractures in CCS, methods to remotely monitor changes in fractures are desired. Precipitates in a fracture can fill the pores or adhere to the surface of rock, both of which can increase the contact area and reduce fracture apertures. Compressional and shear waves have been shown to be sensitive to the size and spatial distributions of voids and contact area in a fracture [9], and are therefore a promising tool to monitor fractures. Kendall et al [10] used ultrasonic waves to monitor stationary and sliding surfaces, and were able to successfully distinguished the area of contact.

In the nature, mineral precipitation does not always occur alone; instead, in many situations, it is produced simultaneously with the dissolution of a fracture under the influence of reactive flow. It is of great interest to know under what situation fractures dissolve and seal. Dijk et al [11] investigated the effects of reactive solutes in fractures through numerical modeling, and found that different pairs of Damköhler (Da) and Péclet (Pe) numbers (Da= reaction rate/ diffusion rate, Pe = advection rate/ diffusion rate) give different spatial distribution of precipitates. For example, low Damköhler, typical Péclet numbers (Da=10<sup>-8</sup>, Pe=1) and typical Damköhler, high Péclet numbers (Da=10<sup>-4</sup>, Pe=10<sup>4</sup>; representing the solute transport is dominated by advection) will result in highly uniform spatial distribution of precipitates in the fractures.

For the case of high Damköhler, typical Péclet numbers case (Da=10, Pe=1, representing the solute transport is dominated by surface reaction), the spatial distribution of precipitation is highly non-uniform.

Zhao et al [12] modeled two interacting fluids that flow in different direction in a vertical fault, and observed three types of reaction patterns. Thin lenticular precipitates preferentially form (a) starting at the lower tip of the vertical fracture and continuing accumulating to through the entire fracture when the two fluids flow in parallel as shown in Figure 1.1 (a) left; (b) near the inlet and exit region of the fracture when there is a new fluid produced within an existing fluid flow system by thermal or chemical reactions as shown in Figure 1.1 (b) left; and (c) throughout the entire fracture when one fluid flows in a direction perpendicular to the other fluid's flow direction as shown in Figure 1.1 (c) left. This research indicates that the way fluids mixing can determine the spatial distribution of mineral precipitation.

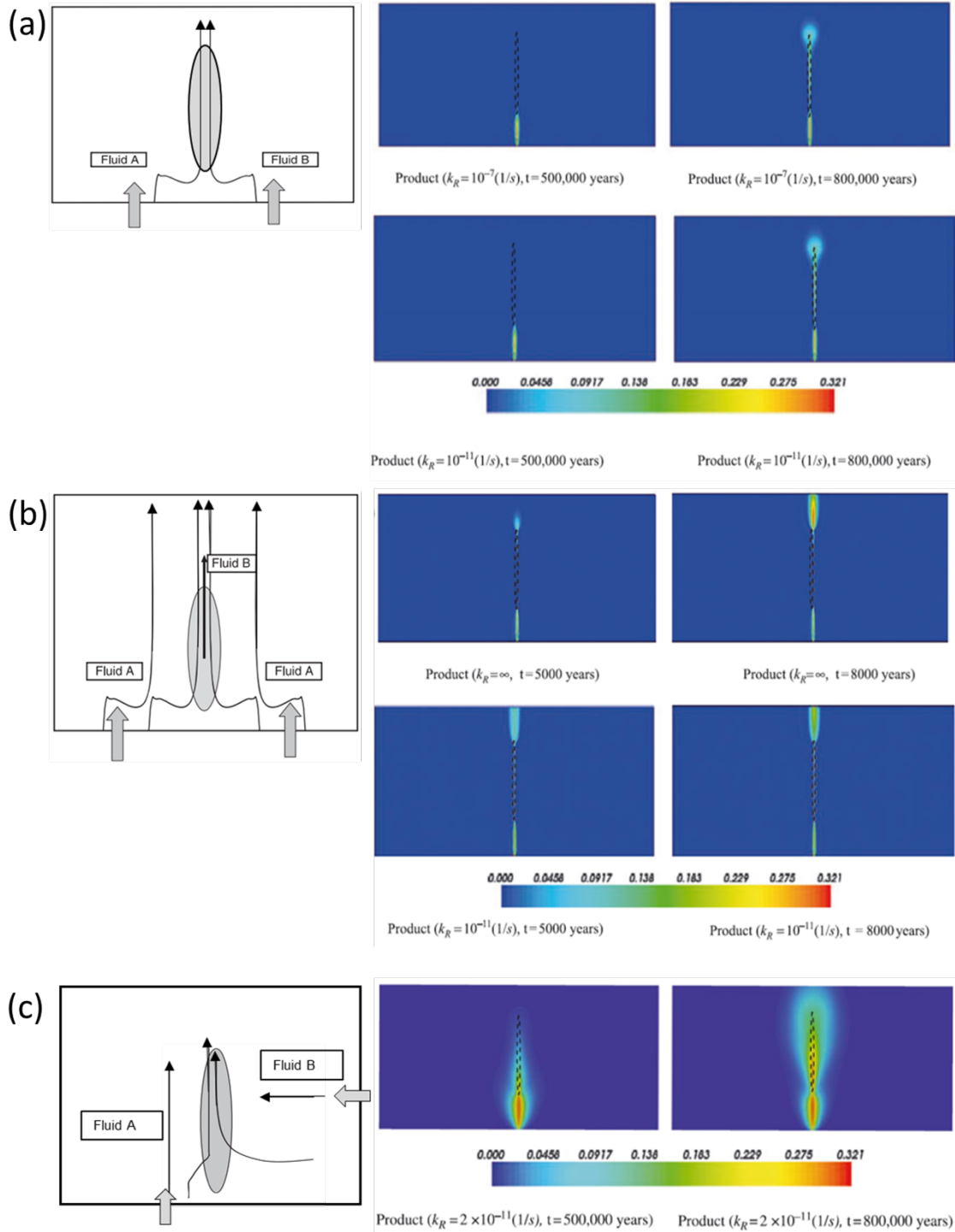


Figure 1.1 Comparison of the three types of mineral precipitation patterns at two different time instants. Precipitates preferentially formed (a) from the lower tip; (b) near the inlet and exit region of the fracture; (c) throughout the entire fracture. (From Zhao et al [12]).

Experimentally, Cao et al [13] and Luquot et al [14] pumped CO<sub>2</sub>-rich brine through fractured samples and they specifically observed that mineral precipitation is promoted by long residence times and smaller initial fracture apertures for low flow rates, because they provide suitable conditions for dissolved Ca<sup>2+</sup> to re-deposit. Arvidson et al [15] investigated dolomite (carbonate mineral composed of calcium magnesium carbonate, e.g, CaMg(CO<sub>3</sub>)<sub>2</sub>) precipitation rate, and found it to be a strong function of solution temperature and composition, and expressed the relation in a simple expression:

$$r = Ae^{-(\epsilon_A/RT)}(\Omega - 1)^n,$$

where  $r$  is the precipitation rate,  $A$  is the pre-exponential frequency factor,  $\epsilon_A$  is the activation energy,  $T$  is the temperature,  $\Omega$  is the estimate of the reaction order. The result from this study implies that “consideration of the relationship between dolomite and calcite in terms of activation energies suggests that small increases in temperature would yield significant increases in dolomite precipitation rate relative to calcite.” [15]

From this brief literature review, there are many factors that affect mineral precipitation. Temperature, fracture aperture, flow rate, reaction rate, diffusion rate, etc., all of which influence the precipitation rate, spatial distribution, and the amount of precipitate in a fracture. Among them, diffusion and reaction rates are the most important factors that tend to dominate precipitation. It is apparent that better mixing of the reactive fluids and longer residence time would generate more precipitate. Thus, the diffusion and reaction rate, along with flow rate, together control the precipitation by eventually altering the mixing of the fluids and reaction time.

Fluid mixing is extremely important in this study because it is directly related to the formation, transportation and distribution of mineral precipitation. Understanding how fluids mix

can help predict the behavior of the mineral precipitation generated from reactive flow. Density contrast, flow rate, channel geometry, etc. all affect a fluids' behavior. The simplest case for two fluids mixing is: fluid 1 rests on top of fluid 2. Suppose the fluids have the same viscosity, but different densities, e.g.  $\rho_1 > \rho_2$ . Initially a flat interface forms between the fluids. After time, due to gravity, fluid 1 sinks and fluid 2 rises. The interface would become unstable and fingers of low density fluid would appear. This behavior is the Rayleigh-Taylor (RT) instability [16]. After long enough time, the two fluids would mix well only due to the influence of gravity. If the density of the fluids reversed, where  $\rho_1 < \rho_2$ , then the interface would always be flat under gravity. Fluid 1 and 2 would still mix due to diffusion but at a much slower rate.

Viscosity affects mixing when there is relative motion between the two fluids. A simple but typical system for studying two fluids mixing with relative motion is the displacement of one fluid by a second fluid in a horizontal rectangular channel (Hele-Shaw cell). Tchelepi [17] investigated the influences of viscosity and density in both 2D and 3D models. He defined a viscous-to-gravity ratio

$$R_{v/g_z} = \frac{\bar{v} \Delta \mu}{k_z \Delta \rho g} \frac{H}{L}$$

where  $v$  is the mean Darcy velocity in the x direction,  $k_z$  is the characteristic permeability in z direction (can be obtained numerically) (2D case only has x and z directions) (Figure 1.2),  $\mu$  is viscosity difference,  $\rho$  is the density difference, H is the height and L is the length of the channel, to determine whether viscosity or buoyancy (gravity) dominates the flow. When the mixing is completely dominated by gravity, the displacing fluid (with a smaller density) formed a “gravity tongue” covering top of the channel (Figure 1.2). While if the mixing is totally dominated by viscosity, “fingers” appeared from the displacing fluid towards the displaced fluid. When using

$R_{v/gz}$  as a standard to judge the fluid behavior, he found that when  $R_{v/gz} < 2$ , both 2D and 3D model show gravity overrides viscosity; when  $2 < R_{v/gz} < 10$ , 2D model shows a gravity tongue but recedes as  $R_{v/gz}$  increase, while 3D model still shows gravity dominates; when  $10 < R_{v/gz} < 20$ , in 2D model, viscous fingering dominates the displacement with slight interference from buoyancy, while 3D model shows a dominant fingered gravity tongue; when  $R_{v/gz} > 20$ , viscous fingering completely dominates 2D model and in 3D model, fingered gravity tongue break up and gradually became completely fingering dominates as  $R_{v/gz}$  increases (Figure 1.3). This study provided a numerical range for predicting how two fluids mix with different density contrast and viscosity difference, and also reveals that in viscosity dominant mixing, 2D simulation cannot capture the real displacement behaviors, thus 3D simulation is necessary. In the experiments in this thesis,  $R_{v/gz}$  is in the range of  $< 2$ .

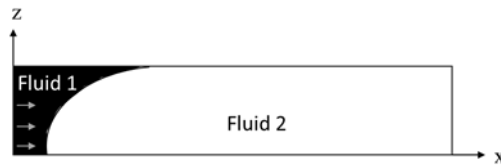


Figure 1.2 Sketch of displacement of one fluid by a second fluid in a horizontal rectangular channel.

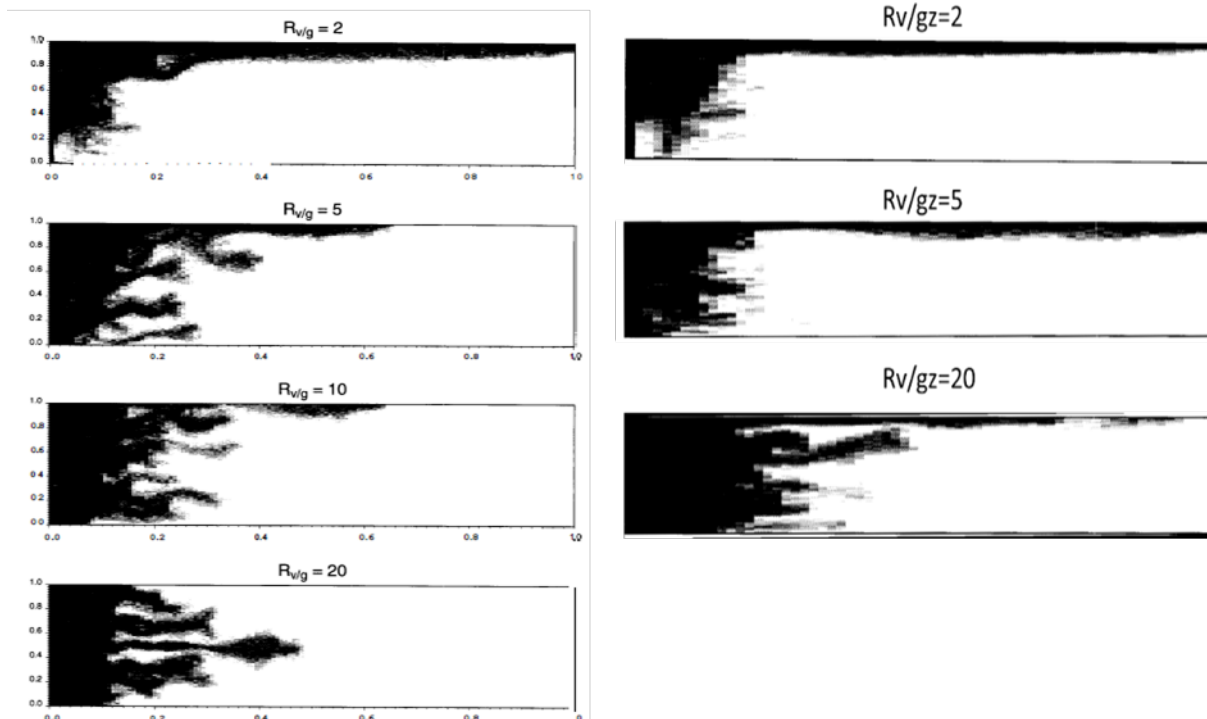


Figure 1.3 (left) Flow mixing in different  $Rv/g$  in 2D model; (right) Flow mixing in different  $Rv/gz$  in 3D model (Cross section of  $y=16$ ).

When considering the influence of flow rate relative to the channel, Reynolds number ( $Re$ ) is used which is the ratio of inertial forces to viscous forces, and is expressed as  $Re = \frac{\rho u L}{\mu}$ , where  $u$  is velocity of the fluid with respect to an object, and  $\rho$  is the density, and  $L$  is the characteristic length,  $\mu$  is the viscosity. Usually when  $Re$  is large, inertial forces dominate, resulting in turbulence.

Another useful dimensionless number is the Schmidt number ( $Sc$ ).  $Sc$  is the ratio of momentum diffusivity to the mass diffusivity.  $Sc$  is important in a convective system based on momentum and mass diffusion. It can be expressed as  $Sc = \frac{\mu}{\rho D}$ , where  $D$  is the diffusion coefficient. Large Schmidt number means that momentum transport dominates over diffusion transport. Peclet number  $Pe = uL/D$  is the ratio of advective transport rate to diffusive transport rate, and is also the product of  $Re$  and  $Sc$ . When  $Pe$  is large, the transport is dominated by advection.

A 2D three-layered model (fluid 1-mixing layer- fluid 2) simulation was performed by Sahu et al [18] to study effects of Re and Sc on fluid displacement. A previous study [19] showed that fluid mixing was driven by Kelvin-Helmholtz (KH) instabilities. KH instabilities occur along the interface between two fluids when there is a difference in velocity between two fluids [20]. In the model, the fluid in the channel is initially at rest. During the displacement, a velocity difference exists across the interface. The effect of Re is illustrated by fixing the viscosity ratio to 30 and  $Sc=100$ , and increasing Re from 100 to 500, resulting in a change from smooth edged displacement flow to an intricate flow pattern with many instabilities (Figure 1.4 left). Large Re results in instabilities. Meanwhile, the influence of Sc was shown by comparing two cases when  $Sc=1$  and 10 while keeping the other parameters unchanged. When  $Sc=1$ , the displacing fluid has smooth edge, but with a wider mixing layer. When Sc increases to 10, instabilities appear (Figure 1.4 right) and momentum dominates transport. In another work [21] focused on the influence of a density contrast on the same fluid displacement scenario, when a less dense fluid displaced a denser fluid (Figure 1.5), the less dense fluid forms a shape similar to the gravity tongue mentioned above (Figure 1.2). While conversely, if a denser fluid displaced a less dense fluid, the denser displacing fluid would form a “reversed” gravity tongue in the lower part of the channel (Figure 1.6). They also investigated the effect of an inclined channel on fluids stability. In the case of a less dense fluid displacing a denser fluid, instability was controlled by the less dense fluid injection direction relative to gravity. When the inclination angle of the fracture was between  $0^\circ$  and  $90^\circ$ , the flow was more unstable than for the case when the inclination angle was between  $-90^\circ$  and  $0^\circ$ . The situation is opposite in the case of a denser fluid displacing a less dense fluid: negative inclination angle led to more unstable flow than positive angle. It is easy to understand that when gravity helps

in the displacement of a fluid, more instabilities arise. On the other hand, if gravity hinders the displacing fluid movement, the flow is more stable.

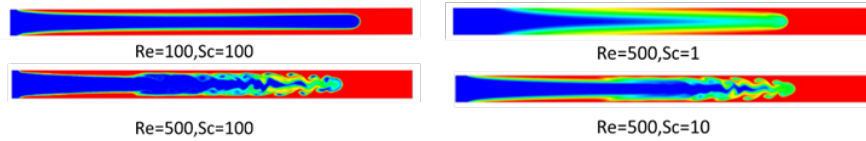


Figure 1.4 Influences of Re and Sc on fluid mixing.

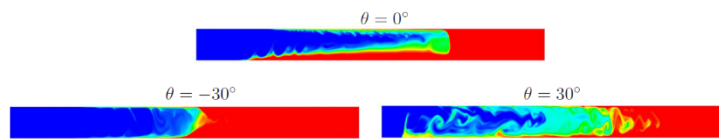


Figure 1.5 Less dense fluid displacing denser fluid.

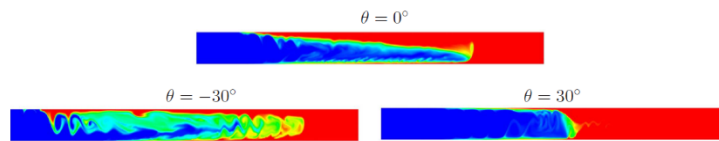


Figure 1.6 Denser fluid displacing less dense fluid.

Natural fractures in rock do not have uniform aperture distributions. As mentioned above, a 2D model might not be able to capture the fluid behavior in 3D case. Furthermore, all the simulation studies mentioned above all dealt with the situation that one fluid initially occupied the fracture apertures, and then was displaced by a second fluid. In reality, two fluids can flow into a fracture at the same time. Therefore, in this Ph.D study, how two fluids simultaneously flow into a uniform aperture fracture was studied. In the experiments, Re is 1.3, in a low Re range to avoid turbulence. Sc was on the order of  $10^4$ , for momentum dominated transport. Optical images were taken from the plane parallel to the fracture plane, to capture the fluid behavior.

The main focus of this thesis work is on fluid (both non-reactive and reactive) mixing experiments in fractures. Interests of study is to explore the effect of gravity driven mixing on the

spatial distribution of fluids and precipitates. Instead of doing experiments on rough fractures, the simplest and most common model Hele-Shaw cell was used in fluid mixing. The experimental methods are given in Chapter 2, and results and discussions on fluid mixing are in Chapter 3. At the same time, exploration of the effect of precipitates on compressional wave propagation was also performed and the results are given in Chapter 4. Finally, conclusion and future works are presented in Chapter 5.

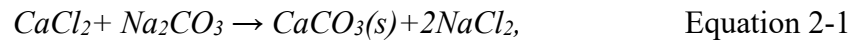
## CHAPTER 2. EXPERIMENTAL METHODS

### 2.1 Fluid Components and Chemistry

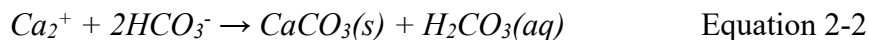
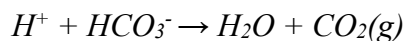
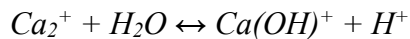
#### 2.1.1 Mineral Precipitation from Miscible Reactive Flow

In the reactive experiments, two approaches were used to induce mineral precipitation of calcium carbonate ( $\text{CaCO}_3$ ) in a fracture through the mixing of the two solutions.

One formulation generated pore-filling precipitates (also known as homogeneous precipitation) that form out of solution (see Figure 2.1 (left)). For pore-filling precipitation, **Solution 1** was a 1 mol/L concentration calcium chloride ( $\text{CaCl}_2$ ) aqueous solution and **Solution 2** was a 0.3 mol/L concentration sodium carbonate ( $\text{Na}_2\text{CO}_3$ ) aqueous solution (see Table 2.1, and Table 2.3). The reaction is:



A second formulation was used to create surface adhering precipitation (also known as heterogeneous precipitation) (see Figure 2.1 (right)). **Solution 1** was a 1 mol/L concentration calcium chloride ( $\text{CaCl}_2$ ) aqueous solution and **Solution 2** was a 0.6 mol/L concentration sodium bicarbonate ( $\text{NaHCO}_3$ ) aqueous solution (see Table 2.2). The reaction for these two solutions results in



such that excessive  $\text{CaCl}_2$  leads to an acidic solution, and  $\text{H}^+$ , calcium carbonate ( $\text{CaCO}_3$ ) precipitation, and the production of carbon dioxide ( $\text{CO}_2$ ) gas.

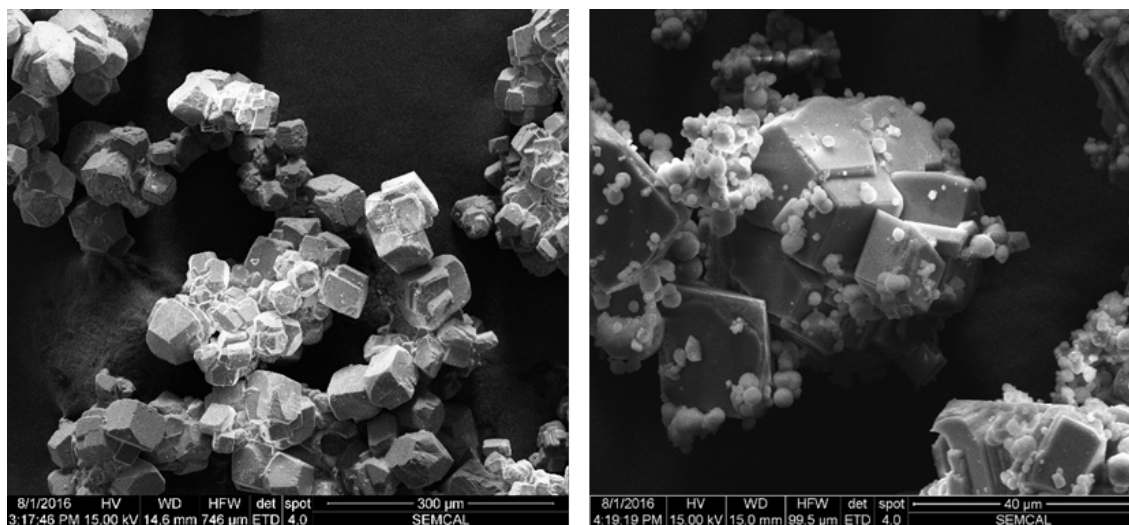


Figure 2.1 Scanning electron microscope (SEM) image of (left) pore filling precipitates; (right) surface adhering precipitates.

Table 2.1 Solutions for pore filling precipitation

<b>Pore Filling Precipitates</b>					
	<b>Component</b>	<b>Molarity (mol/L)</b>	<b>Amount (g)</b>	<b>Density (kg/m<sup>3</sup>)</b>	<b>Viscosity (Pa-s)</b>
Solution 1	CaCl <sub>2</sub> *2H <sub>2</sub> O	1.0	14.7	1111	1.23x10 <sup>-3</sup>
	H <sub>2</sub> O		96.4		
Solution 2	Na <sub>2</sub> CO <sub>3</sub>	0.3	3.18	1032	1.08x10 <sup>-3</sup>
	H <sub>2</sub> O		100		

Table 2.2 Solutions for surface adhering precipitation

<b>Surface Adhering Precipitates</b>					
	<b>Component</b>	<b>Molarity (mol/L)</b>	<b>Amount (g)</b>	<b>Density (kg/m<sup>3</sup>)</b>	<b>Viscosity (Pa-s)</b>
Solution 1	CaCl <sub>2</sub> *2H <sub>2</sub> O	1.0	14.7	1111	1.23x10 <sup>-3</sup>
	H <sub>2</sub> O		96.4		
Solution 2	NaHCO <sub>3</sub>	0.6	5.04	1050	9.90x10 <sup>-4</sup>
	H <sub>2</sub> O		100		

Table 2.3 Solutions for uniform aperture precipitation experiment

<b>Uniform Aperture Precipitates</b>				
<b>Experiment</b>	<b>Solution</b>	<b>Component</b>	<b>Molarity (mol/L)</b>	<b>Density (kg/m<sup>3</sup>)</b>
1	1	CaCl <sub>2</sub>	1.0	1111
	2	Na <sub>2</sub> CO <sub>3</sub>	0.3	1030
2	1	CaCl <sub>2</sub>	1.0	1111
	2	Na <sub>2</sub> CO <sub>3</sub>	0.67	1071
3	1	CaCl <sub>2</sub>	1.0	1111
	2	Na <sub>2</sub> CO <sub>3</sub>	1.05	1111

### 2.1.2 Non-reactive Miscible Fluids

To understand how fluid mixing occurs inside a fracture and in turn affects the formation of mineral precipitates, non-reactive fluid mixing experiments were also performed. The baseline experimental solutions used for these experiments are listed in Table 2.4. The densities of **Solution 1** and **2** were the same as the solutions used in the pore filling precipitation experiments (see Table 2.1) to eliminate the effects of different densities from these experiments. A small amount of bromocresol green (pH indicator) was added to **Solution 1** to make the 2 solutions distinguishable when mixing together. **Solution 1** appeared to be blue and **Solution 2** was colorless. Against a white background, Solution 2 appeared to be white.

Table 2.4 Solutions for miscible non-reactive fluids mixing

<b>Miscible non-reactive fluids</b>				
	<b>Component</b>	<b>Amount (g)</b>	<b>Density (kg/m<sup>3</sup>)</b>	<b>Viscosity (Pa-s)</b>
Solution 1	Na <sub>2</sub> CO <sub>3</sub>	2.07	1111	1.20x10 <sup>-3</sup>
	NaCl	9		
	Bromocresol green	0.03		
	H <sub>2</sub> O	100		
Solution 2	Na <sub>2</sub> CO <sub>3</sub>	3.18	1031.8	1.08x10 <sup>-3</sup>
	H <sub>2</sub> O	100		

In the experiments studying the effect of a density contrast, the amount of NaCl in **Solution 1** is adjusted, to alter the density as shown in Table 2.5. **Solution 2** is pure water.

Table 2.5 Solutions for miscible non-reactive fluids mixing for density contrast

	<b>Solution 1</b>				<b>Solution 2</b>
	<b>Experiment</b>				
	<b>1</b>	<b>2</b>	<b>3</b>	<b>4</b>	
<b>Na<sub>2</sub>CO<sub>3</sub> (g)</b>	1.84	1.84	1.84	1.84	0
<b>NaCl (g)</b>	9.23	18.13	38.13	78.13	0
<b>Bromocresol green (g)</b>	0.03	0.03	0.03	0.03	0
<b>H<sub>2</sub>O (g)</b>	100	100	100	100	100
<b>Density (kg/m<sup>3</sup>)</b>	1111	1200	1400	1800	1000

### 2.1.3 Precipitates Composed of CaCO<sub>3</sub> Powder and Water

In the experiment with CaCO<sub>3</sub> powder used as the precipitation to fill a uniform aperture fracture, a mixture of CaCO<sub>3</sub> powder and water was used to mimic a precipitate-filled fracture. The fracture was first filled with water, and a transmitted signal was recorded. Then the fracture was filled with a mixture of CaCO<sub>3</sub> powder and water, and transmitted signals were recorded. The

two signals were then compared to determine the effects on transmitted P-waves. Results are given in section 4.3.1

## **2.2 Sample Description**

### **2.2.1 Variable Aperture Fracture**

Poly-urethane casts of an induced fracture in Austin chalk were used in both homogeneous (pore filling) and heterogeneous (surface adhering) mineral precipitation experiments, with the fracture plane oriented either parallel or perpendicular to gravity. When the fracture plane is parallel to gravity, this will be referred to as “vertical”, while “horizontal” refers to a fracture plane that is perpendicular to gravity. The transparency of the poly-urethane enabled direct digital imaging of the fluid distributions and mineral precipitation in the fracture throughout the duration of the experiments. Water absorption by the poly-urethane sample is on the order of 0.3% to 2% by weight [22].

Poly-urethane samples were fabricated as follows: A mold composed of flat acrylic plates was assembled around a sample of Austin chalk with an induced fracture. Alumilite's High Strength 2 silicone rubber was then poured into the space between the wall and the Austin chalk sample. After 24 hours of curing, the Austin chalk was removed from the rubber. The rubber formed a mold of the fracture. Before casting with urethane, the rubber mold was preheated in the oven at 66°C for 30 minutes (Heat is generated when resin A and resin B are mixed, causing the temperature of the mixture to increase. If the mold is not preheated, the mixture near the edge releases heat into the mold and can result in a cast with deformed edges). Next, Alumilite Water Clear casting resin A and resin B were mixed with equal weight and poured into the rubber mold. The mold with the resin was then transferred to a pressure tank, and placed under 20 psi (138 KPa) air pressure. The resin-filled mold was held under pressure for 24 hours while it cured.

The casted-poly-urethane sample measured 100 mm × 100 mm × 78 mm (Figure 2.2). The properties of the solidified poly-urethane are listed in Table 2.6. Two inlet ports were drilled 38 mm apart into the upper half of the fracture sample and day-lighted on the upper fracture surface (Figure 2.2). A slot was cut into the lower fracture surface and a hole was drilled for outlet tubing. The two fracture surfaces were placed in contact, screwed together at the corners, and sealed with DAP silicone rubber sealant to prevent any fluid from leaking into the acoustic imaging water-tank or water from the tank leaking into the sample.

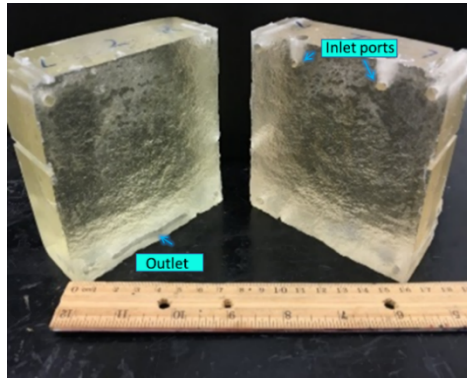


Figure 2.2 Casted poly-urethane fracture sample.

Table 2.6 Properties of the solidified urethane

Property	Value
Hardness, (ASTM D-2240) Shore D	72
Specific Gravity	1.05
Shrinkage (in/in)	0.005
Tensile Strength (ASTM D-638) (psi)	3120
Elongation (in/in)	30-40%

### 2.2.2 Uniform Aperture Fracture

Two casted urethane flat plates were used to form fractures with uniform apertures. The plates were casted using the same formulation as described in section 2.2.1 but with a different mold. These samples were used to study fluid plume development caused by a density contrast

between the fluids during the chemical reactions. The sample size was 100 mm × 100 mm × 78 mm (Figure 2.3).

For the non-reactive fluid mixing experiments, to ensure a flat surface, 0.5 inch thick flat transparent polycarbonate (PC) sheets were used (from McMaster-Carr). The properties of the PC sheets are listed in Table 2.7. Two inlet ports were drilled 38 mm apart into the upper half of the sample and a slot was cut into the lower fracture surface and a hole was drilled into the side to connect a tube to the outlet (Figure 2.3). The edges of two fracture surfaces were separated by PTFE (Polytetrafluoroethylene) films or sheets, to create uniform apertures of 0.5 mm, 1 mm and 2 mm. Then the two fracture surfaces were screwed together, and sealed with PDMS (Polydimethylsiloxane) and DAP silicone rubber sealant.

Table 2.7 Properties of the flat polycarbonate sheet

<b>Property</b>	<b>Value</b>
Hardness (Rockwell M)	95
Density (kg/m <sup>3</sup> )	1190.23
Thickness Tolerance (mm)	-1.651 to +0.635
Tensile Strength (psi)	8000
Water Absorption	0.50%

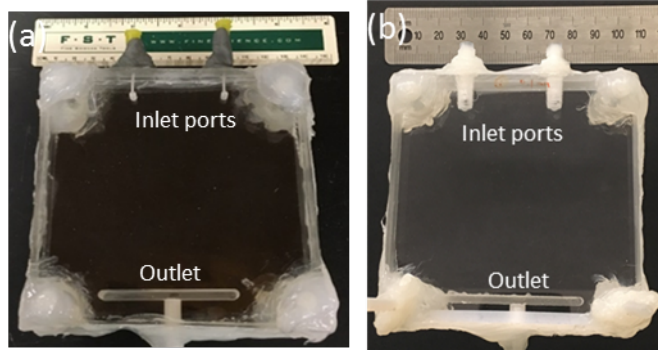


Figure 2.3 (a) Casted urethane uniform aperture fracture sample; (b) acrylic uniform aperture fracture sample.

### 2.2.3 Fracture Composed of Rough Surface in Contact with a Flat Surface

One flat smooth PC plate and one casted poly-urethane rough fracture surface were placed in contact to form a fracture. To examine the effect of large-scale roughness on fluid mixing behavior, both sides of the rough fracture were used to make 2 separate samples with roughness that were inverse of each other. Two inlet ports were drilled 38 mm apart into the smooth PC sheet and a slot was cut into the rough urethane fracture surface and a hole was drilled into the side to connect a tube to the outlet (Figure 2.4).

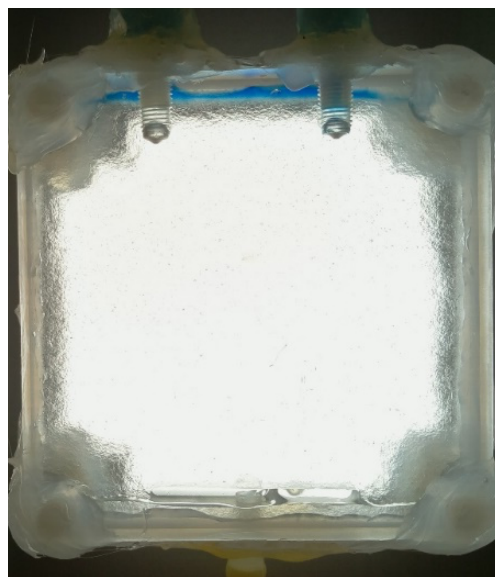


Figure 2.4 Fracture composed of rough surface in contact with a flat surface.

### 2.2.4 3D Printed Uniform Aperture

Form 2 3D printer from Formlabs was used to print uniform aperture sample to enable mixture of  $\text{CaCO}_3$  powder and water filling fracture experiment and also reactive mixing experiment. FLGPBL04 black resin was used to print the sample. The properties of the cured resin is shown in Table 2.8. The fracture sample is shown in Figure 2.5.

Table 2.8 Properties of cured 3D printing FLGPBL04 black resin

Property	Value
Tensile Strength (ASTM D-638) (psi)	9380
Elongation at Failure	6.2%
Water Absorption	<1%
Density ( $\text{kg/m}^3$ )	1500
P-wave Velocity (m/s)	2729



Figure 2.5 3D printed uniform aperture sample.

### 2.3 Fluid Pumping System

Two Harvard Apparatus syringe pumps were used to introduce two solutions simultaneously into a fracture. The pumps were connected to the two inlet ports on the sample with 1/8 inch diameter PFA tubing and 1/16 inch MNPT Swagelok fittings. One 200 mL syringe contained **Solution 1** and the other syringe contained **Solution 2** (see Table 2.1, Table 2.2 and Table 2.3). The fracture was initially saturated with either **Solution 1** or 2, depending on the experiments, and then allowed to equilibrate (with the pump off) for 2 hours. Then the two solutions were simultaneously pumped into the fracture at the desired constant flow rate for 5 hours to enable mixing and the formation of mineral precipitates. After 5 hours, the pumps were turned off.

### 2.4 Digital Imaging of Fracture

A custom-built digital optical imaging system was used to record images of the fracture prior to, during and after flowing both solutions into the fracture. The system consisted of a Spy camera for a Raspberry Pi with a native resolution of 5 Megapixels yielding 2592 x 1944 pixel images, a Daylight Wafer 1 Light Box for backlighting, a Digi-Pas DWL-80E Digital Leveler to measure the angle of inclination, and a Digi-Sense Traceable lighter meter to ensure the illumination is always the same. The camera was connected to a Raspberry Pi Model B+ with 512MB RAM. The images were recorded every 5 seconds and stored as jpeg files directly to a 128 GB flash drive. In the experiments without acoustic emission, the spy camera was mounted on a rod fixed to an easel, to ensure that the distance between the camera and the fracture plane was the same for all experiments (see Figure 2.6).

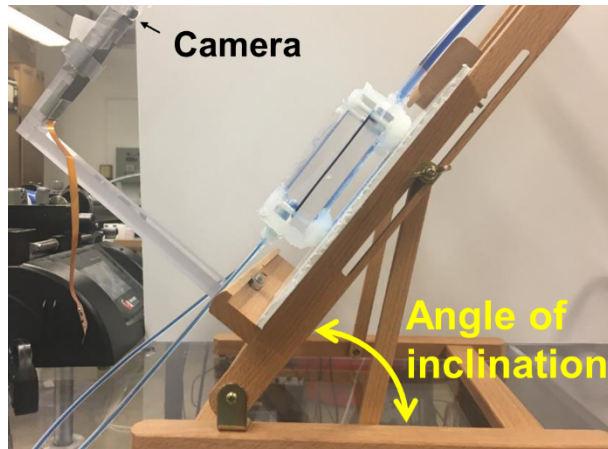


Figure 2.6 Image of the camera and easel.

## 2.5 Pixel Edge Length Calibration

To convert the pixel length into metric units, calibration experiments were performed using an Air Force Test Chart (MIL-STD-150A, 1951 USAF resolution test chart, Figure 2.7). The pixel edge length was determined to be  $65.96 \mu\text{m}/\text{pixel}$ .

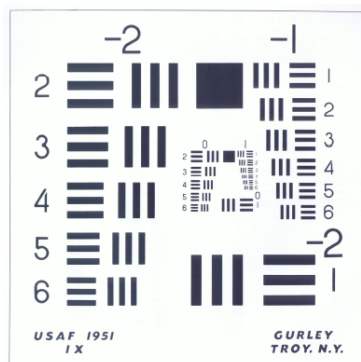


Figure 2.7 Air Force Test Chart used to calibrate the pixel edge length.

## 2.6 Acoustic Monitoring

Even though optical imaging can provide information on precipitate distribution, this is not possible in rock. Acoustic measurements were made to determine if precipitate formation/distribution can be inferred from signal amplitude, arrival time and/or other attributes.

After the poly-urethane sample absorption of water (see section 2.6.1), any observed changes in the acoustic signals were a result of modification of the fracture response from fluid distributions and mineral precipitation.

Compressional waves (acoustic) were used to monitor the fracture during and after precipitate formation. Experiments were performed using either  $\text{CaCO}_3$  powder as the precipitate to fill a uniform aperture fracture, or through reactive mixing in uniform aperture fracture. Contact piezoelectric transducers (Olympus Panametrics-NDT V103, 1 MHz central frequency) were used to receive and send acoustic waves (Figure 2.8). The source transducers were excited with a squared pulse from an Olympus 5077PR pulse generator, using 400V excitation with a 1 kHz repetition frequency. After propagating through a sample, the signals were digitized using a National Instruments PXI-5122 digitizer and stored on a computer for analysis. A custom-built relay box switched the recording between transmitted signals and reflected signals. A sampling rate of 100 M samples/sec was used to obtain 0.01 microseconds/point.

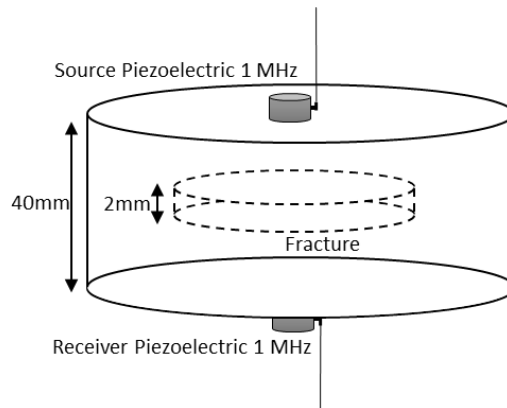


Figure 2.8 Sketch of experimental set-up.

In the experiments with reactive fluids mixing in a rough fracture, acoustic signals were generated and recorded by two arrays of water-coupled piezoelectric transducers (Olympus

Panametrics-NDT V303, 1 MHz central frequency) (Figure 2.9). The arrays contained 1 source transducer and 13 receivers. All the transducers in the system were submerged in water to ensure repeatable coupling to the sample during the entire length of the experiment. Transmitted and reflected signals were collected alternately every 7.5 seconds prior to invading the fracture with the two solutions, during the 5 hours of invasion of both solutions, and for 2 hours after the pump was turned off.

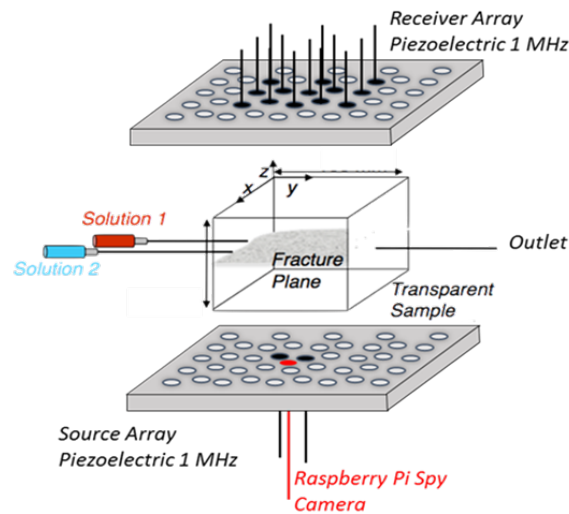


Figure 2.9 Sketch of experimental set-up.

### 2.6.1 System Calibration

As mentioned in section 2.2, poly-urethane absorbs water. A series of experiments were performed to determine the effect of water absorption on acoustic wave transmission.

#### *Only Transducers in Water*

For system calibration and the experiments, water coupled piezoelectric transducers (Olympus Panametrics-NDT V303, 1 MHz central frequency) were used to determine sources of potential error in the experiments (see Figure 2.10). One set of transducers was placed horizontally,

while the other set was placed vertically in a large tank containing only water. First, experiments were performed with no sample to test the variability in the signal over time because the fluid mixing experiments last 5 hours. Signals were recorded every 5 seconds.

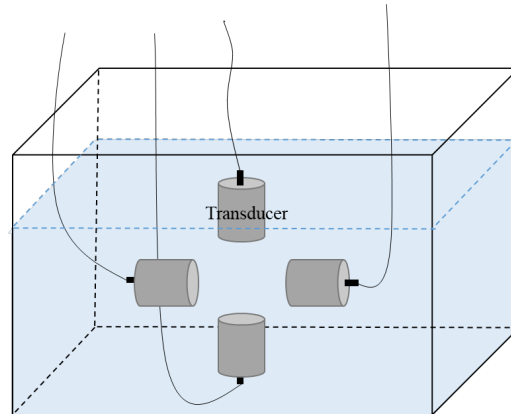


Figure 2.10 Sketch of transducer layout for system calibration.

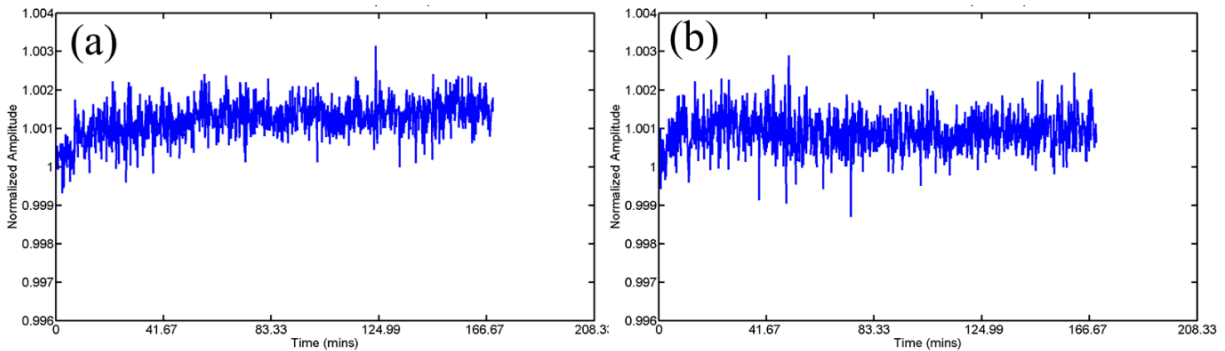


Figure 2.11 Maximum amplitude of transmitted signal as a function of time for (a) horizontal and (b) vertical transducer set when there are only transducers.

From the maximum amplitude of the transmitted waves, it was determined that the system takes ~20 minutes to equilibrate to achieve an amplitude that varies by less than 1% (Figure 2.11), indicating that there were small but measurable systematic effects from the pulse generator, transducers and the PXI.

### *Non-presoaked Small Block with a Dry Borehole*

The second set of calibration experiments used a small cubic poly-urethane block (49mm\*49mm\*40mm) with a borehole (3mm diameter) that was placed between the 2 sets of transducers inside a water tank (see Figure 2.12). The borehole was kept dry during the entire process to determine the effect of external water absorption on the acoustic signals. Again signals were recorded every 5 seconds.

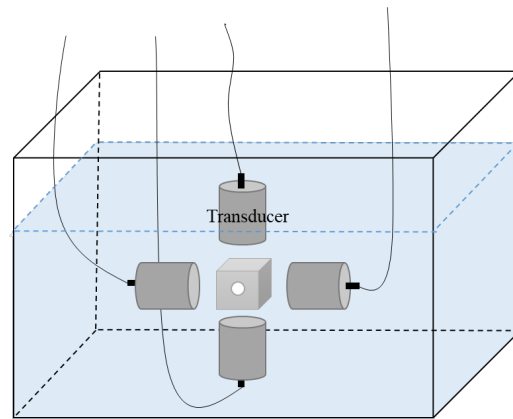


Figure 2.12 Sketch of transducer layout for system calibration with small block sample with a borehole.

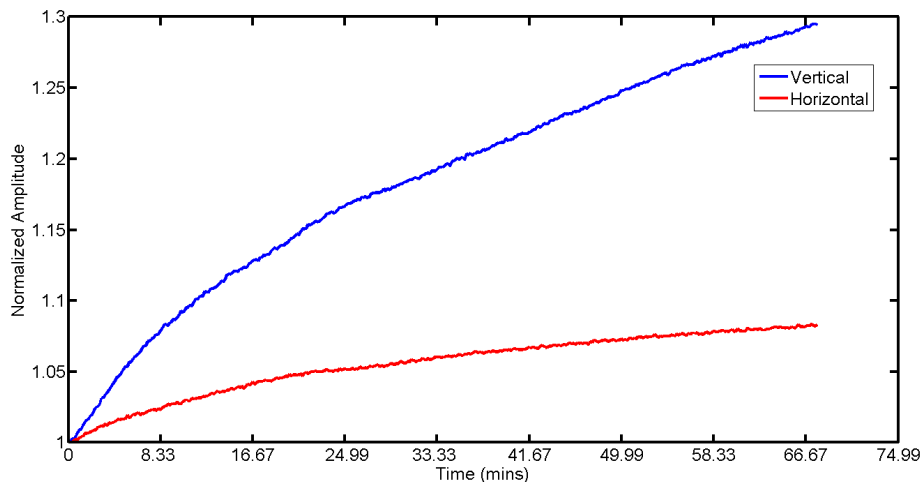


Figure 2.13 Maximum amplitude of transmitted signal as a function of time for horizontal (red) and vertical (blue) transducer set when a cubic poly-urethane block (49mm\*49mm\*40mm) with a dry borehole (3mm diameter) was placed between the 2 sets of transducers inside the water tank.

The maximum amplitude of the transmitted signals was found to increase up to 30% with time as observed in both the horizontal and vertical measurements, and equilibrium was not attained (see Figure 2.13).

### ***Pre-soaked Small Block with a Dry Borehole***

A small cubic poly-urethane block with a borehole was placed between transducer arrays in water. The block sample was pre-soaked in water for 17hrs to determine if the effect of surface absorption of water on the acoustic signal could be reduced or eliminated. The hole was kept dry during the entire process. Signals were recorded every 10 seconds.

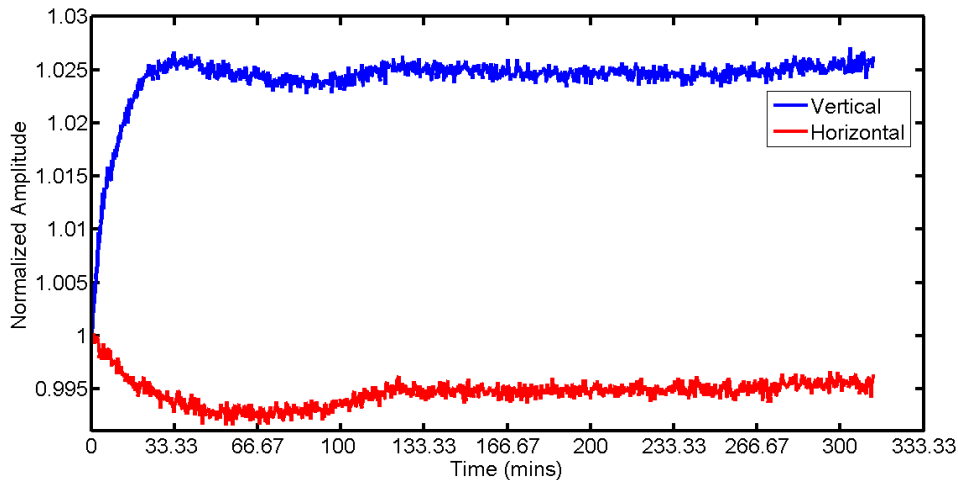


Figure 2.14 Maximum amplitude of transmitted signal as a function of time for horizontal (red) and vertical (blue) transducer set when a cubic poly-urethane block (49mm\*49mm\*40mm) with a dry borehole (3mm diameter) and saturated for 17 hours was placed between the 2 sets of transducers inside the water tank.

The maximum amplitude of transmitted signal equilibrated in roughly 35 minutes. The variation in amplitude was  $\sim 2.5\%$  (Figure 2.14. blue line). Compared with non-pres soaked sample, the change in maximum amplitude of transmission signal was much smaller after pre-soaking the sample. These experiments indicated that all poly-urethane samples used for acoustic testing needed to be presoaked prior to use.

### ***Non-pres soaked Small Block with a Saturated Borehole***

A small cubic poly-urethane block with a borehole was placed between transducer arrays inside a water tank. The hole was initially saturated with  $\text{Na}_2\text{CO}_3$  solution, and then acoustic signals were recorded every 5 seconds over 9 hours.

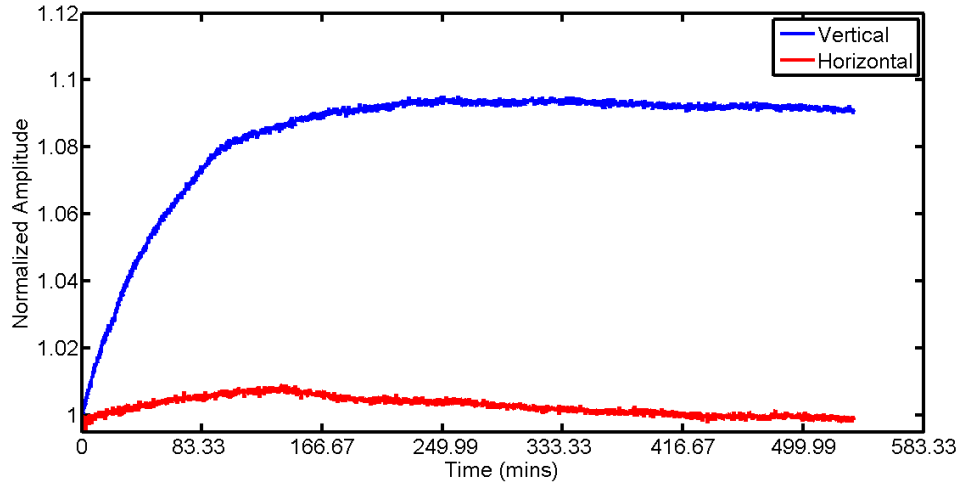


Figure 2.15 Maximum amplitude of transmitted signal as a function of time for horizontal (red) and (blue) vertical transducer set when a cubic poly-urethane block (49mm\*49mm\*40mm) with a borehole (3mm diameter) which was saturated with  $\text{Na}_2\text{CO}_3$  solution was placed between the 2 sets of transducers inside the water tank.

The maximum amplitude of transmitted signal first increased then decreased for horizontal transducers. For the vertical transducers, the amplitude increased until equilibrium was reached. The variation in amplitude was 10% due to the absorption of liquid from the external surface and in the borehole (see Figure 2.15). This experiment and the experiment from the previous section “Pre-soaked Small Block with a Dry Borehole” demonstrated that presoaking of the sample was required to minimize signal artifacts.

### ***Presoaked Small Block with a Saturated Borehole***

A small cubic poly-urethane block with a borehole was placed between transducer arrays in a water tank. The entire sample was submerged in water and the borehole was saturated with

solution for 20 hours before recording any transmitted signals. Signals were recorded every 5 seconds.

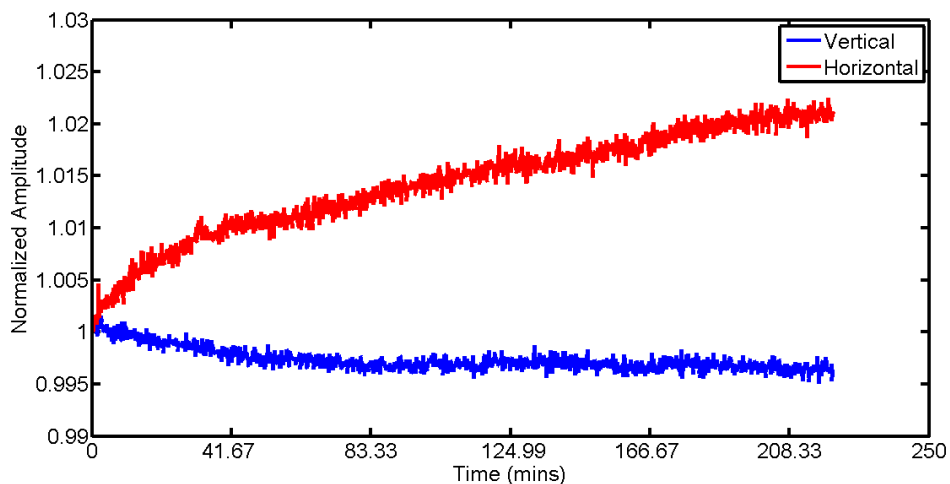


Figure 2.16 Maximum amplitude of transmitted signal as a function of time for horizontal (red) and vertical (blue) transducer set when a cubic poly- urethane block (49mm\*49mm\*40mm) with a borehole (3mm diameter) which was saturated with  $\text{Na}_2\text{CO}_3$  solution for 20 hours was placed between the 2 sets of transducers inside the water tank.

From Figure 2.16, it took 45 minutes for the vertical transducer to equilibrate. For horizontal transducer, the maximum amplitude still increased but appeared to approach an asymptote for 3% increase in amplitude.

Combining the results from the above experiments, it was concluded that, to reduce systematic errors, all samples surfaces were presoaked  $\sim 20$  hours prior to use and signal acquisition was started 45 minutes or more before initiation of chemical reactions.

## 2.7 Precipitation Analysis

The precipitation samples collected from the reactive mixing experiments were sent to Subsurface Energy Materials Characterization and Analysis Lab (SEMCAL) in Ohio State University, to be scanned from 4 to 70 degrees 2-theta with a PANalytical X'Pert Pro X-ray

diffractometer (45 keV accelerating voltage; 40 mA tube current; CuK $\alpha$  radiation) to test the component of the deposit.

SEM scanning was also performed on the precipitation samples to investigate the morphology of the precipitation. SEM samples were prepared by adhering small quantities of precipitate on carbon tape mounted to aluminum stub holders, followed by sputter coating with Au/Pd. Images were acquired using an FEI Quanta 250 field emission gun SEM at Ohio State University.

## **2.8 X-ray CT Scan**

After the experiment of reactive mixing in a uniform fracture, the fracture samples were scanned using Carl Zeiss Xradia 510 X-ray microscope at 80 kV, 7W, to obtain the exact size of the fracture aperture and the thickness of precipitates. Results are shown in section 4.3.1.

## CHAPTER 3. GRAVITY DRIVEN CHEMICAL DYNAMICS IN FRACTURES

### 3.1 Introduction

In the subsurface, reactive fluids can alter fractures from dissolution that erodes the flow path through a fracture and from mineral precipitation that can partially or fully seal fractures. Natural fractures in the subsurface can have different orientations relative to gravity. This research focused on the effect of gravity-driven chemical dynamics on the spatial distribution of mineral precipitates in a fracture. To simplify the problem, potential fluid-rock chemical interactions were eliminated in the experiments by using synthetic fracture.

Experiments showed that the spatial distribution of reaction-induced mineral precipitation ( $\text{CaCO}_3$ ) in a variable aperture fracture varies significantly with the orientation of the fracture plane relative to gravity. For vertical and horizontal variable aperture fractures, two types of reactions and two different conditions were tested. The two types of reactions were pore-filling (homogeneous) and surface adhering (heterogeneous) (see section 2.1.1). The two different conditions tested in the fractures were: (1) initially saturated with **Solution 2** (Normal order); and (2) initially saturated with **Solution 1** (Reverse order). In the pore-filling experiments, the density of **Solution 1** is  $1111\text{kg/m}^3$  and density of **Solution 2** is  $1031.8\text{kg/m}^3$ ; in surface adhering experiments, the density of **Solution 1** is  $1111\text{kg/m}^3$  and density of **Solution 2** is  $1050\text{kg/m}^3$ .

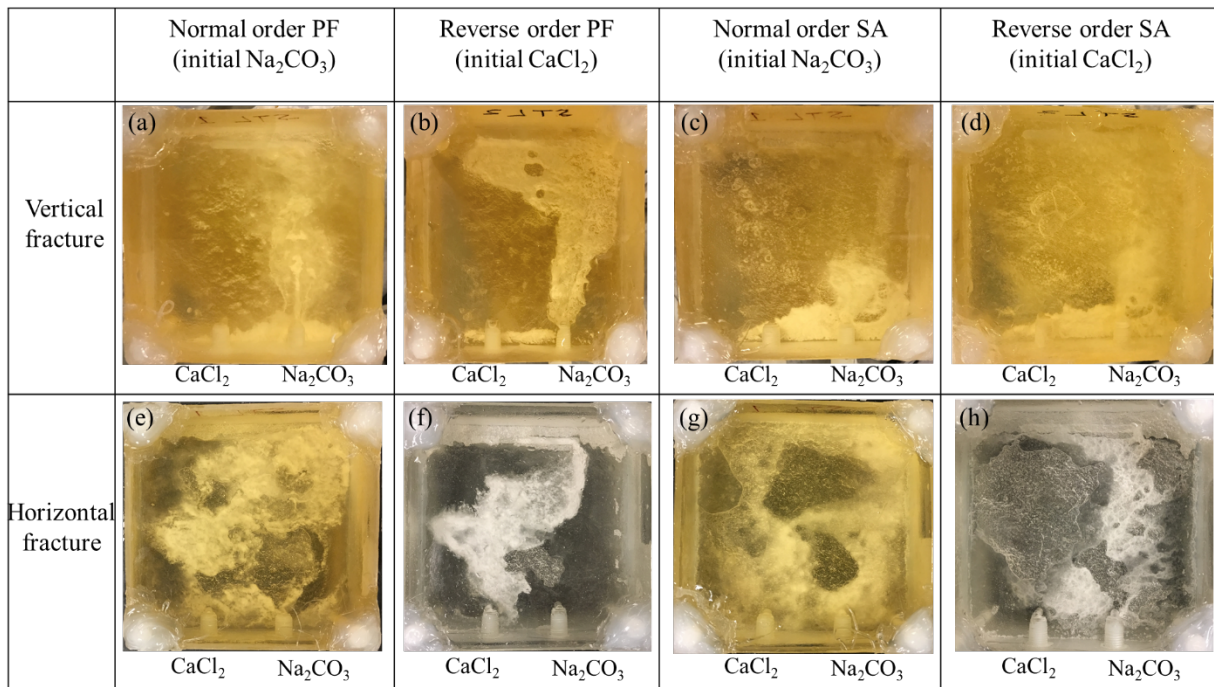


Figure 3.1 Precipitate distribution for (a) vertical normal order pore-filling; (b) vertical reverse order pore-filling; (c) vertical normal order surface-adhering; (d) vertical reverse order surface-adhering; (e) horizontal normal order pore-filling; (f) horizontal reverse order pore-filling; (g) horizontal normal order surface-adhering; (h) horizontal reverse order surface-adhering.

Figure 3.1 shows the precipitate distribution for all of the experimental conditions. In the vertical fracture, the precipitate pattern for both normal order and reverse order pore-filling is very similar to each other. Precipitation mainly occurs on the Na<sub>2</sub>CO<sub>3</sub> side. The difference is that more precipitate accumulated at the bottom of the fracture in normal order pore-filling experiment than in reverse order pore-filling experiment (see Figure 3.1 (a) and (b)). Figure 3.1 (e) and (f) show the normal order and reverse order pore-filling experiments but in a horizontal variable aperture fracture. The precipitation in both cases is more uniformly distributed along the entire fracture surface (reverse order pore-filling experiment covers less area than normal order pore-filling), which is caused by gravity. Recall the “gravity tongue” from reference [21] and Figure 1.5, Figure 1.6. For normal order experiment, the initial saturation **Solution 2** is lighter than later injected **Solution 1**, so under gravity, during the process **Solution 1** forms a “tongue” in the bottom of the

fracture, resulting in better mixing with **Solution 2**. While in the case of reverse order pore-filling, the initial saturated **Solution 1** is heavier than later injected **Solution 2**, causing the injected **Solution 2** to form a “gravity tongue” that is on top of the **Solution 1**, which results in poor mixing compared to the normal case.

As for the normal order and reverse order surface adhering experiments in vertical fracture, the precipitates were distributed on the  $\text{Na}_2\text{CO}_3$  side (see Figure 3.1 (c) and (d)). Due to the generation of  $\text{CO}_2$  gas, few precipitates were formed in the fracture. The gas blocked voids and prevented mixing of the two solutions. In the horizontal fracture, precipitate distribution of the normal order and reverse order surface adhering covers more of the fracture than in the vertical fracture (see Figure 3.1 (g) and (h)). **Solution 2** is lighter than **Solution 1**, such that stratified flow occurs across the fracture plane (i.e. lighter solution rides on top of denser fluid). As the reaction continues, the generated  $\text{CO}_2$  gas tends to occupy the large apertures and prevents precipitate from forming in those voids.

The experiments described above, in general, show that under gravity, miscible reactive solutions with a density contrast mix better in a horizontal fracture than a vertical fracture, and thus the distribution of precipitation is expected to be more uniform along the entire fracture. This occurs because of stratified flow. Furthermore, for the normal order experiments, in which the initial saturated solution is the lighter one, the later injected solution mixes and reacts with the initial solution better under gravity, and thus forms more uniformly distributed precipitation. In the surface adhering precipitation cases, the generation of  $\text{CO}_2$  gas bubbles to some extent influences the formation of precipitates, but the overall trend of the precipitation under gravity is the same as pore filling precipitation.

The spatial distribution of both pore filling and surface adhering precipitation is tremendously affected by the fracture orientation relative to gravity as shown in Figure 3.1. This leads to the question: how do gravity driven dynamics affect the mixing process between 2 miscible fluids? To answer this question, non-reactive mixing experiments were performed to remove the influence of the chemical reaction. The effects of fracture inclination angles, fracture aperture, fluid density contrast, and fluid pumping rate on miscible fluid mixing were studied. But before reviewing the results from those experiments, a preliminary experiment was done to confirm that compare to gravity driven dynamics, the influence of fracture roughness on fluid mixing is negligible.

### 3.2 Non-reactive Mixing in a Variable Aperture Fracture

Fractures composed of a rough surface in contact with a flat surface were used to investigate the influence of fracture roughness on non-reactive mixing. The fluid properties and pumping rates are listed in Table 3.1 along with fracture inclination angle.

Table 3.1 Parameters for studying influence of rough fracture.

<b>Pumping rate (ml/min)</b>	0.17
<b>Density of Solution 1 (kg/m<sup>3</sup>)</b>	1111
<b>Density of Solution 2 (kg/m<sup>3</sup>)</b>	1031.8
<b>Viscosity of Solution 1 (Pa-s)</b>	1.20x10 <sup>-3</sup>
<b>Viscosity of Solution 2 (Pa-s)</b>	1.11 x10 <sup>-3</sup>
<b>Fracture inclination angle (°)</b>	90

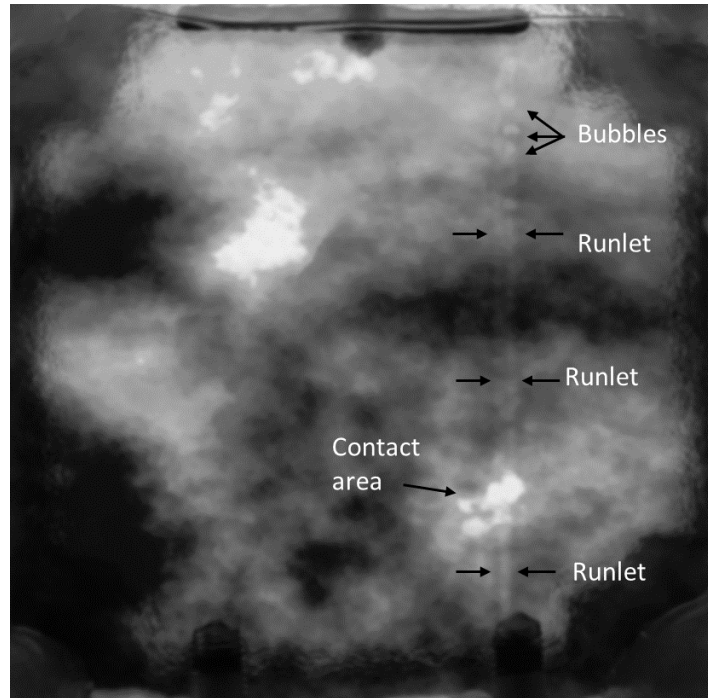


Figure 3.2 Gray scale image of non-reactive mixing in fracture composed of rough surface in contact with a flat surface.

The results from the variable aperture fractures are very similar to the case for a uniform aperture inclined at  $90^\circ$  (in next section). As shown in Figure 3.2, the less dense solution was confined to a small discontinuous runlet composed of small bubbles. This result shows that in these experiments the dominant factor is not the wall roughness or void shape but the density contrast between the fluids.

Next, the effects of fracture inclination angles, fracture aperture, fluid density contrast, and fluid pumping rate on miscible fluid mixing are given to determine the effect of these parameters on the size and extent of the fluid mixing region.

### 3.3 Mixing of Miscible Fluids in a Uniform Aperture Fracture

Fractures can vary in orientation and aperture, and the fluids that flow through them can have different densities and velocities. These are all important factors that may affect fluid mixing

and mineral precipitation distribution. Therefore, in the following experiments, the effects of fracture inclination angles, fracture aperture, fluid density contrast, and fluid pumping rate on miscible fluid mixing were studied.

### **3.3.1 Influence of Inclination Angle**

#### ***3.3.1.1 Mixing of Non-reactive Miscible Fluids in a Uniform Aperture Fracture***

Fractures in the subsurface can have different orientations relative to gravity. The inclination angle of a fracture plane was varied to determine its effects on fluid mixing. In these experiments, the aperture, pumping rate, and density contrast were kept constant. For miscible non-reactive fluids, the fracture plane was initially saturated with a less dense fluid (**Solution 2** in Table 2.4 and whitish regions in Figure 3.3 left). After saturation, both fluids were simultaneously pumped into the fracture plane at the same rate of 0.17 ml/min. **Solution 2** was pumped in through the right port (Figure 3.3 left) while the denser fluid (**Solution 1**), was pumped in through the left port at the same flow rate. Initially, the density contrast between the two fluids resulted in fluid stratification caused by gravity (T= 25 min in Figure 3.3 left most column). For a fracture inclination angle of 90°, as the pumping continued, the denser **Solution 1** confined **Solution 2** to a narrow path or runlet which remained even after **Solution 2** was completely displaced by the denser **Solution 1** from the fracture plane. The runlet increased in width with decreasing fracture inclination angles of 75°, 60°, 45°, 30° and 15° (Figure 3.3 left). For all inclination angles, the runlet stabilized after 167 minutes and did not change in extent for the remaining 133 minutes of an experiment.

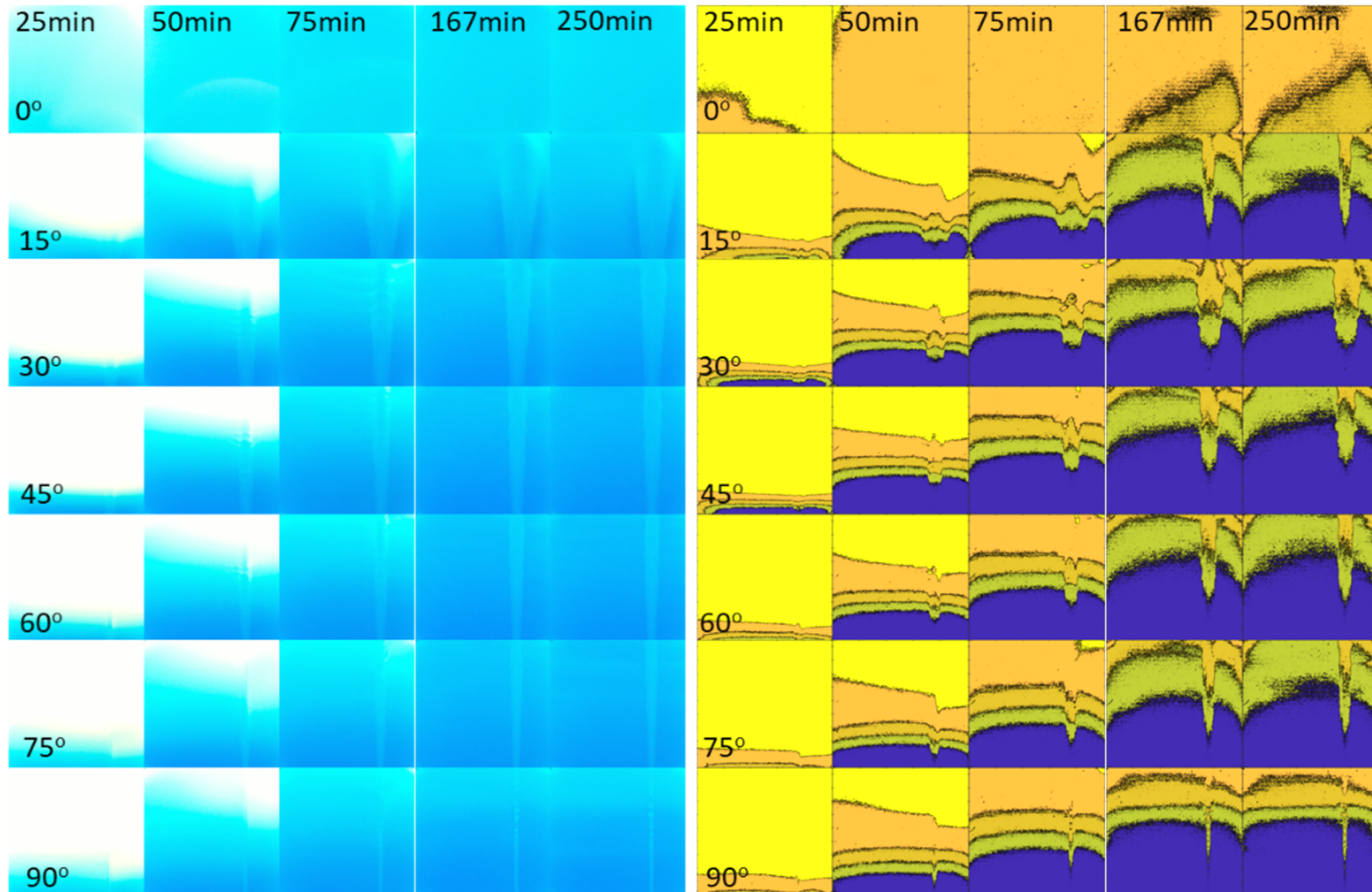


Figure 3.3 (left) Digital images from non-reactive miscible fluid mixing experiments. (right) Processed images from non-reactive miscible fluid mixing experiments. Fluids have been represented with 5 range concentration of Solution 1: Yellow: <25%; Orange: 25%-50%; Olive: 50%-75%; Cyan: 75%-100%; Blue:~100%. Each row shows images from a different fracture inclination angle (15°-90°). Each column represents different times during the experiments (25, 50, 75, 167 and 250 mins after start pumping both fluids). Aperture is 2 mm; pumping rate is 0.17 ml/min for both Solution 1 and 2; density contrast is 1111/1031.8.

These experimental observations demonstrate that for fractures, the mixing and spatial distribution of miscible nonreactive fluids with different densities are affected by gravity through the inclination angle of the fracture plane. The density contrast restricts the less dense fluid to a narrow path, while the miscibility of the fluids results in hydrodynamic instabilities that create bubble-like features along the runlet. For example, for an inclination angle of  $90^\circ$ , discrete bubbles of the less dense solution are observed (Figure 3.3 left, times 50-250 minutes). While for fracture inclinations of  $30^\circ$  and  $60^\circ$ , ripples along the width of the runlet path are observed at 50 and 75 minutes (Figure 3.3 left). In addition, the runlet bifurcates into two branches once the fracture is no longer vertically inclined ( $90^\circ$ ).

Figure 3.4 provides a comparison of the runlet geometry at 250 minutes after the initiation of the simultaneous fluid invasion for the different fracture inclinations. Image processing to enhance the less dense solution in the images was performed using MATLAB by subtracting the background gradient of the fluid density concentration. The area of the less dense solution was evaluated at the different inclination angles to compare to fluid distributions in the reactive miscible fluid case. As the fracture inclination angle decreased, the area of the less dense runlet increased. Figure 3.5 shows the area of runlets as a function of angles of inclination. The change in area with angle of inclination is captured by  $\csc(\theta)$ , which is related to the component of gravity parallel to the fracture plane.

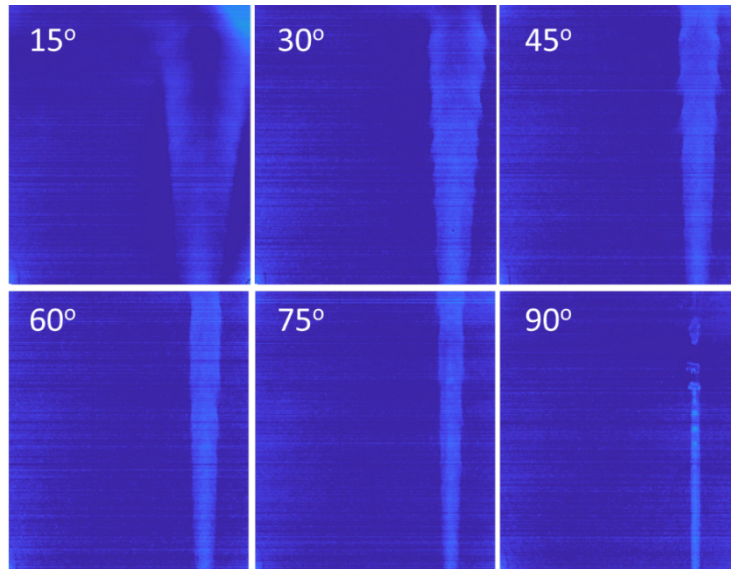


Figure 3.4 Comparison of runlet geometry from the invasion of nonreactive miscible fluids in fractures inclined at 15° to 90° for T=250 minutes after the simultaneous invasion of two fluids. Aperture is 2 mm; pumping rate is 0.17 ml/min for both Solution 1 and 2; density contrast is 1111/1031.8.

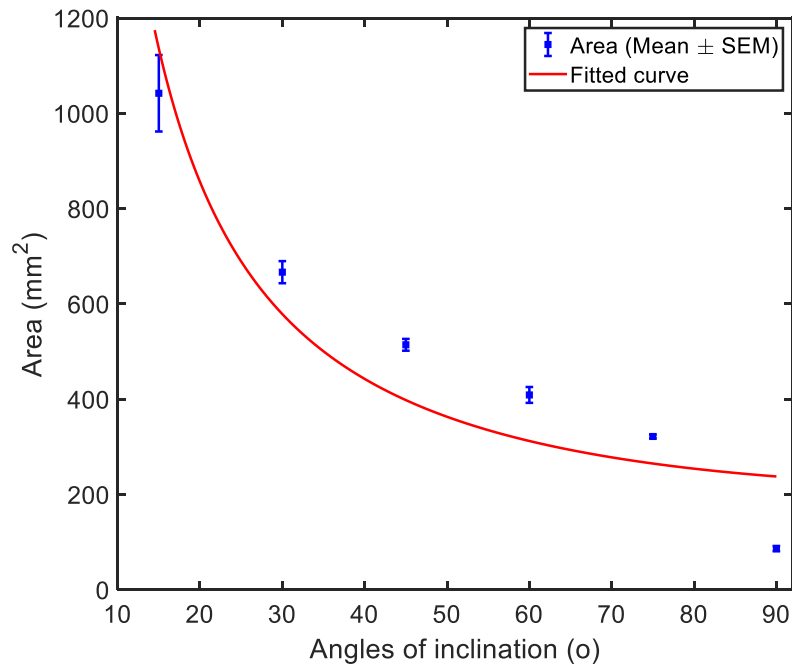


Figure 3.5 Area of runlets as a function of angles of inclination. The blue points represent the mean area with an error bar of standard error of mean (SEM). Red line is the fitted curve. Aperture is 2 mm; pumping rate is 0.17 ml/min for both Solution 1 and 2; density contrast is 1111/1031.8.

Though the two solutions are pumped into the fracture with the same flow rate (0.17 mL/min), the relative velocities of the two fluids differ because of the difference in the size of the areas of the dense fluid and the less dense runlet. The bubble and ripples observed for the 30°- 90° cases are similar to Kelvin-Helmholtz (KH) instabilities. Instabilities along the interface lead to a wavy surface with a wavelength,  $\lambda_b$ , that depends on the aperture,  $b$ . Studies on horizontal Hele-Shaw cells found that the wavelength of KH between two *immiscible* fluids with different densities and viscosities was affected by the aperture of the cell, and for a fixed aperture increased with distance from the inlet [23]. In this study, the  $Pe \sim 10^4$  based on values from the experiment, assuming a  $D$  on the order of  $10^{-10} \text{ m}^2/\text{s}$  [24].

From our data, the bubble and ripple spacing was observed to evolve over time. Figure 3.6 shows the bubble/ripple spacing observed in the runlets for the 15° to 90° cases for times of 83.33 and 250 minutes. The small square in each plot represented the mean, and the left and right boundaries represented the minimum and maximum respectively. At  $T=83.33$  minutes, the average spacing between the ripples for fracture inclinations of 15° to 75° are ranged from 5.87mm to 6.74mm and varied with distance from the inlet. The spacing decreases with distance from the inlet which is contrary to the observations for KH instabilities for *immiscible* fluids (by observing the images in the two sides). For the 90° case, the spacing between the bubble-like features is 3.51mm.

At  $T=250$  minutes, the average spacing was observed to increase to 7.19mm to 9.79mm for 15°,45°,60° and 75°. A decrease from 6.51mm to 6.26mm was observed for 30°. For the 90° case, the spacing between the bubbles reduced to 3.42mm. The measured spacings are greater than the expected wavelength,  $\lambda_b$ , for RT instabilities found by [25] because in addition to the density contrast between the miscible fluids there is also a difference in velocity which may also give rise

to KH instabilities. Both instabilities affect the geometry of the mixing line between the two fluids which is important when the two fluids are reactive.

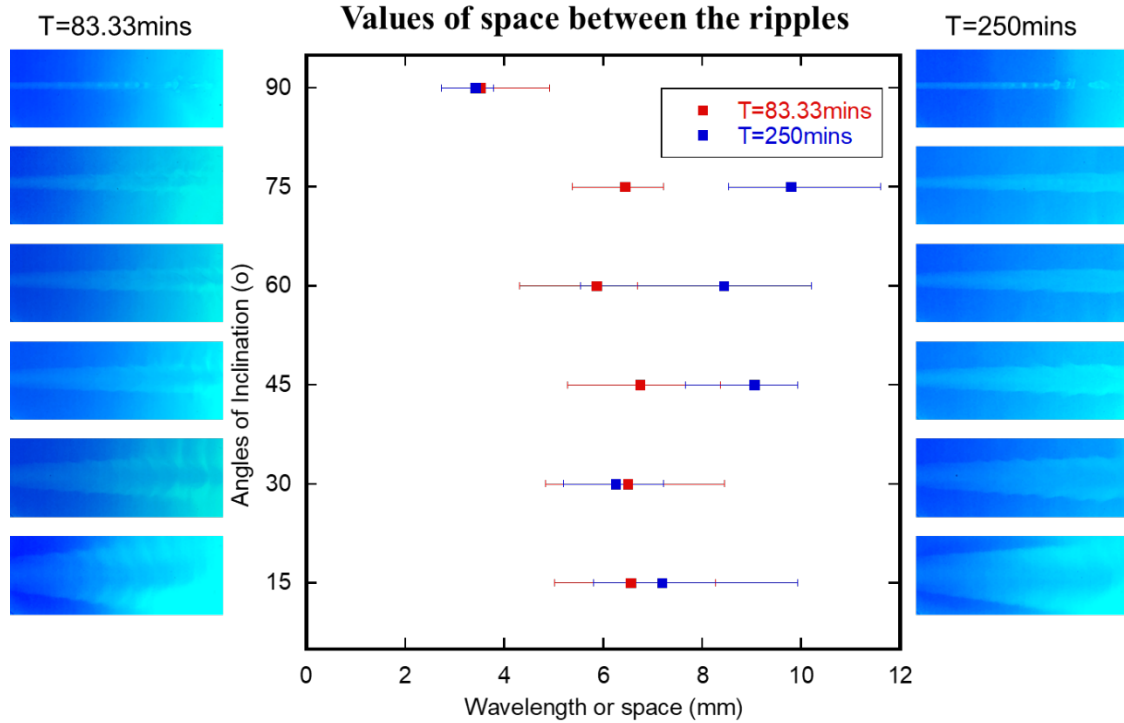


Figure 3.6 Values of space between the ripples at angles 15° to 90° at T=83.33 minutes and T=250 minutes. Aperture is 2 mm; pumping rate is 0.17 ml/min for both Solution 1 and 2; density contrast is 1111/1031.8.

The spatial distribution of fluid concentration across the fracture plane was studied to determine how two fluids mixed over time. Four mixing solutions of **Solution 1** and **2** were used to calibrate for image analysis with concentrations of **Solution 1** of 25%, 50%, 75% and 100% by weight (see Table 3.2). Consider the Lambert-Beer law  $A = \epsilon lc$  [26], where  $A$  is the absorbance,  $\epsilon$  is the molar attenuation coefficient,  $l$  is the optical path length and  $c$  is the concentration of the attenuating species. There is a linear relationship between the intensity of light absorbed by a substance dissolved in a solvent and the concentration of the substance, as well as the path length of the light through the solution. Then for a constant backlit source, the change in the light intensity

that passes through the solution is only affected by the concentration and thickness of the solution. There is no difference between a well-mixed and a poor-mixed fluid in terms of the transmitted-light intensity. For example, fluid A is composed of 50% colorless fluid 2 and 50% blue fluid 1, and are well-mixed such that fluid A is in even blue color. Fluid B, on the other hand, is composed of one layer of 50% colorless fluid 2 on top of one layer of 50% blue fluid 1. The light intensity that passes through fluids A and B would be the same as long as the path of the light that travels in the fluids is the same. Therefore, in later context, when a reference is made to some concentration of mixed fluids, it can either be a well-mixed even color fluid, or possibly a layered fluid. Based on this fact, the ratio of different concentration fluids occupying the fracture over time was obtained. Figure 3.7 shows the fraction of different concentration fluids filling the fracture over time. The bin is in 5-minute increments for the stacked bar graph. The change in the fraction over time for different concentration is affected by the fracture inclination angle.

Table 3.2 Component of fluids for color calibration in terms of concentration of Solution 1

<b>Concentration of mixed fluid in terms of Solution 1 (by weight)</b>	<b>Weight of Solution 1 (g)</b>	<b>Weight of Solution 2 (g)</b>
25%	10	30
50%	20	20
75%	30	10
100%	40	0

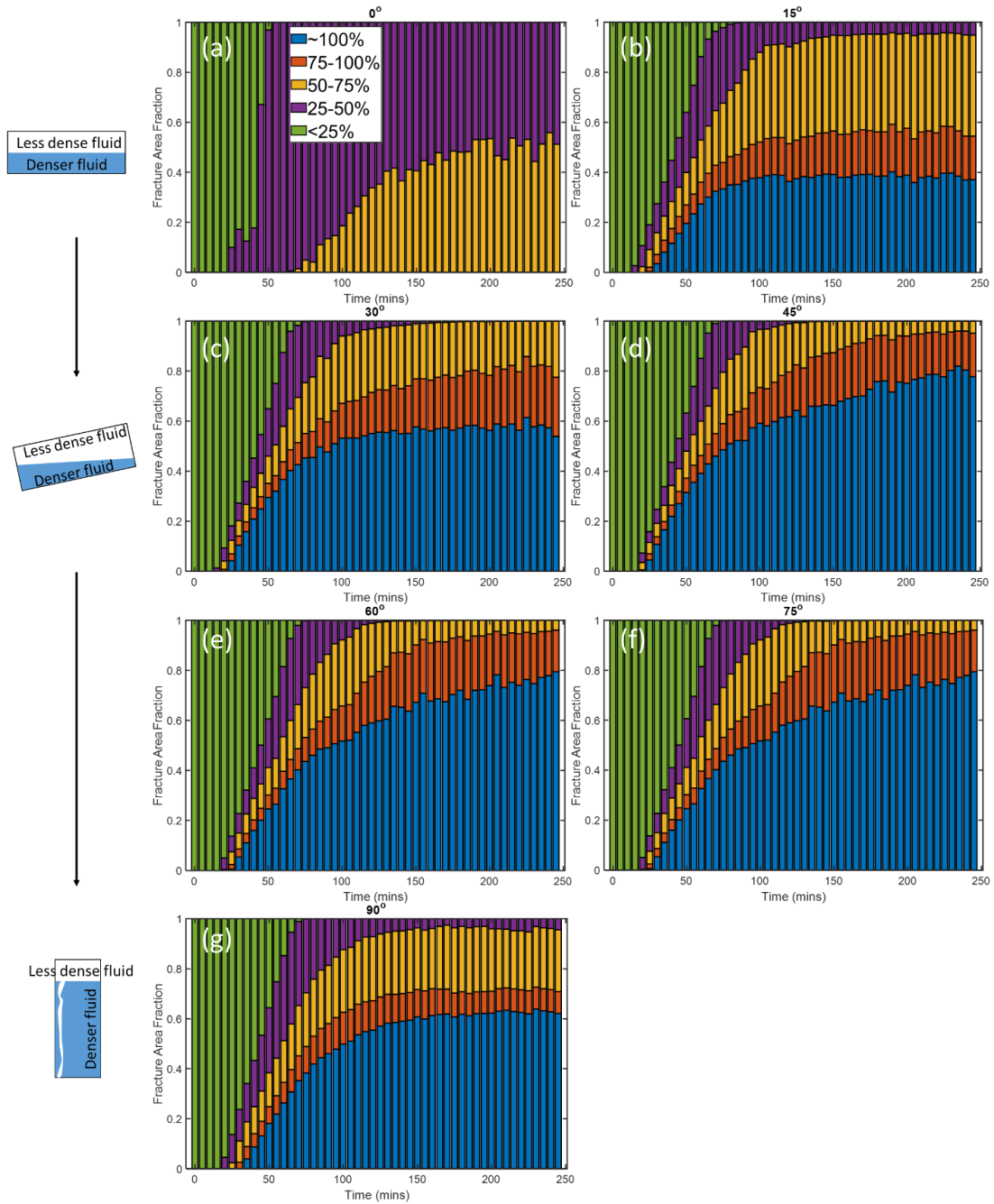


Figure 3.7 Fracture area fraction of different concentration fluids in terms of Solution 1 by weight over time for different inclination angles. Aperture is 2 mm; pumping rate is 0.17 ml/min for both Solution 1 and 2; density contrast is 1111/1031.8.

For an inclination angle of  $0^\circ$ , the fluid with concentration of **Solution 1** <25% initially covered 100% of the fracture plane and soon reduced to 0 after 50 minutes of pumping both fluids.

At the same time, the area of fluid with 25%-50% concentration of **Solution 1** increased from 0 to 100%. As pumping continued, the area of fluid with 50%-75% concentration of **Solution 1** started to increase. Finally, the entire fracture was occupied almost evenly by fluids with concentration 25%-50% and 50%-75% of **Solution 1** (see Figure 3.8), suggesting stratification of flow, i.e. the less dense fluid flowing on top of the denser solution.

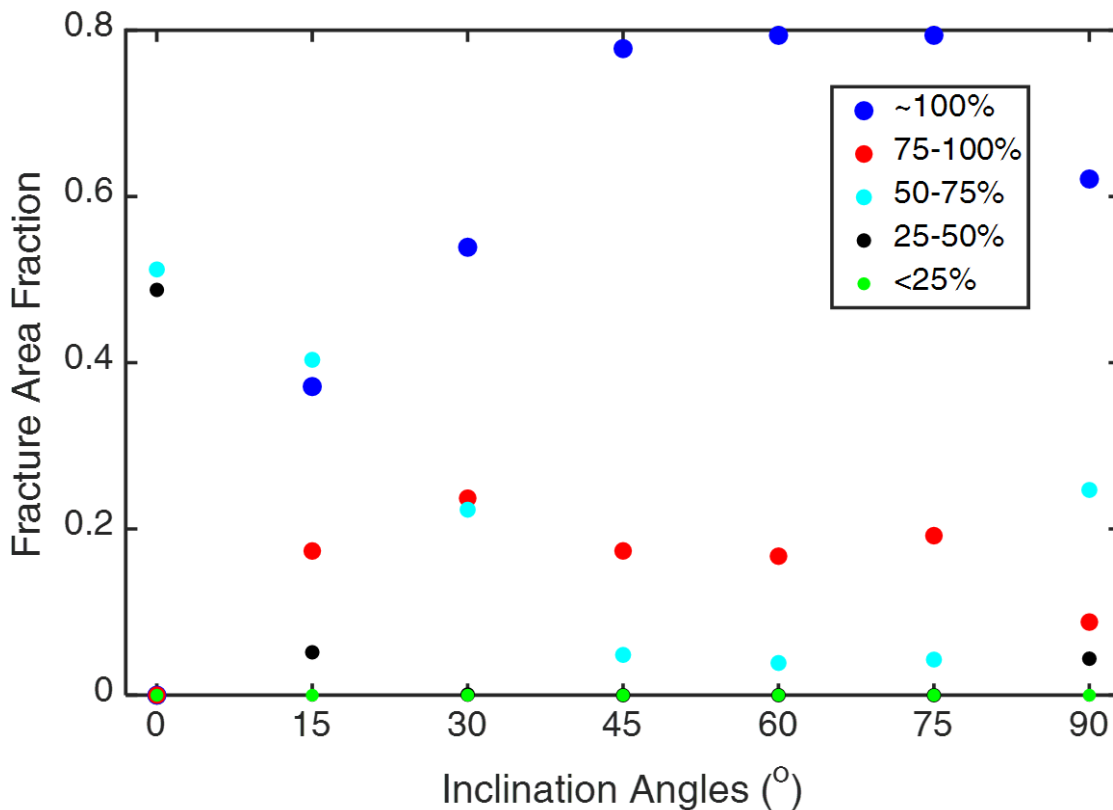


Figure 3.8 Fracture Area Fraction at T=250 minutes for different inclination angles. Aperture is 2 mm; pumping rate is 0.17 ml/min for both Solution 1 and 2; density contrast is 1111/1031.8.

A common behavior for all other fracture inclination angles is that the area of fluid with <25% concentration of **Solution 1** decreased from 100% to 0 within 62 minutes. A fluid with a 25%-50% concentration of **Solution 1** first increased, reached a maximum around 62 minutes and then decreased. The maximum fracture area fraction values are 45.16%, 33.35%, 27.44%, 25.93%,

28.37%, and 35.20% for 15°-90° respectively. Even though varied, these values are not tremendously different, indicating that the change in fluid concentration in this range mainly occurs because **Solution 2** initially saturated the fracture.

Figure 3.8 shows the fraction of different fluid concentration filling the fracture at the end of the experiments (T=250 min). The result indicates that with the increase of inclination angles, fluid mixing decreases. For fluid concentration of 50%-75% for **Solution 1**, it first increased and then decreased in 30°, 45°, 60°, 75° and achieved asymptote in 15° and 90°. From Figure 3.8, the area fraction of fluid in this range decreases with the increase of inclination angles (except 90°. 90° is fundamentally different from other angles from Figure 3.8 thus it would be discussed independently later). The area fraction of fluid with 75%-100% concentration of **Solution 1** at T=250 minutes increases from 0° to 30° and then achieves asymptote. Area fraction of 100% **Solution 1** increased with angles, from 0 at 0° to 80% at 75°. It showed that the effect of inclination angle on fluid mixing is not linear: for example, when  $\theta$  decreased from 75° to 45°, the area almost unchanged, but when  $\theta$  decreased from 45° to 15°, the area drastically decreased around 40%. Considering that the area of less dense fluid runlet decreases with inclination angles, and the edge of the runlet is the interface of two fluids, where mixing occurs, less runlet area leads to worse mixing. So in summary, increase in inclination angle leads to poorer fluid mixing.

Figure 3.9 shows the fluid displacement in 3 different situation:  $\theta=0^\circ$ ,  $\theta=90^\circ$ , and  $0^\circ < \theta < 90^\circ$ . Consider Figure 3.9 (a) at 0°, as the arrow shows, the less dense fluid was pushing horizontally, therefore the angle between buoyancy and fluid movement is 90°. At 90° Figure 3.9 (b), the lower part of the fracture was occupied by the denser fluid, therefore the less dense fluid flow direction is opposite to gravity and the angle between buoyancy and fluid movement is 0°. (c) shows the evolution for a fracture inclination angle between 0° and 90°. In the beginning, less dense fluid

was freely mixing with the less dense fluid initially saturated the aperture (Figure 3.9 (c)). With the continuous pumping of both solutions, denser fluid sinks down and gradually surrounds the less dense fluid. In this case, the buoyancy is upward while the flow direction is parallel to the fracture plane. The angle between buoyancy and fluid movement is acute. The denser fluid confines or restricts the flow path of the lighter fluid.

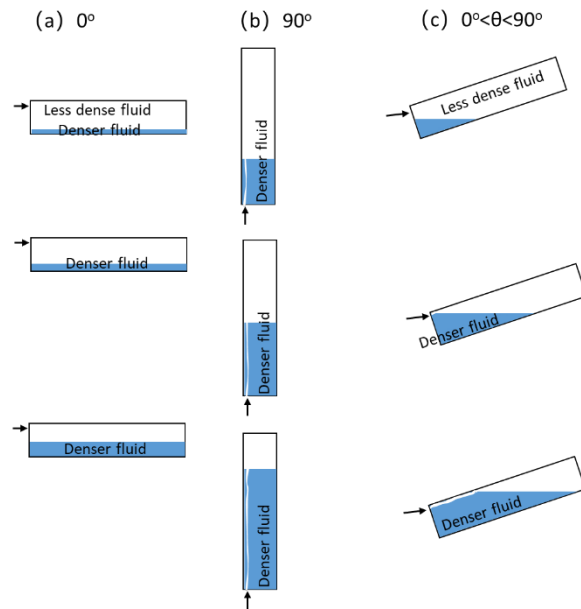


Figure 3.9 (a) Fluids mixing in a horizontal fracture (inclination angle  $0^\circ$ ); (b) Fluids mixing in a vertical fracture (inclination angle  $90^\circ$ ); (c) Fluids mixing in a fracture with an inclination angle between  $0^\circ$  and  $90^\circ$ .

Table 3.3 Parameters for studying influence of inclination angle.

Aperture (mm)	Pumping rate (ml/min)	Density of Solution 1 (kg/m <sup>3</sup> )	Density of Solution 2 (kg/m <sup>3</sup> )	Viscosity of Solution 1 (Pa-s)	Viscosity of Solution 2 (Pa-s)	Fracture inclination angle (°)
2	0.17	1111	1031.8	1.20x10 <sup>-3</sup>	1.11x10 <sup>-3</sup>	0-90, with an interval of 15

### 3.3.1.2 Reactive Mixing of Miscible Fluids in a Uniform Aperture Fracture

The experiments on non-reactive miscible fluids showed that gravity-driven dynamics affected the extent of mixing. Here, reactive fluids are used to see how precipitates distribution are affected under the same gravity-driven dynamics. The miscible *reactive* fluids produce calcium carbonate, CaCO<sub>3</sub>, when mix. Just as for the non-reactive case (section 3.3.1.1) the fracture was initially filled with less dense **Solution 2** (which was dyed with bromocresol green, and therefore is initially blue in color) for the reactive miscible fluids experiments. The denser **Solution 1** was dyed with bromocresol purple, which was initially yellow. When the solutions mixed in a fracture, the pH increased and exceeded 6.8, causing the mixed fluids to turn purple in color (Table 3.4, Figure 3.10).

Table 3.4 pH indicator color change range

Bromocresol purple			Bromocresol green		
pH < 5.2		pH > 6.8	pH < 3.8		pH > 5.4
	⇔			⇔	

The effect of fracture inclination angle on precipitate distribution is manifested in two ways: (1) the spatial distribution of precipitates, and (2) the thickness of the precipitates. For all angles of fracture inclination, mixing between the two fluids occurred across the entire fracture plane because the denser (**Solution 1**) displaced the lighter (**Solution 2**) forming a uniform front. Once

the denser solution reached the outlet, the less dense solution replenished the front leading to continual formation of precipitates along the front. However, depending on the fracture inclination, the precipitates either rained down (i.e. sedimented) from the front and accumulated around the inlet of the fracture, or extended over the entire fracture plane. The sedimentation of the precipitates to regions near the inlet occurred for fracture inclinations of 45° to 90°. While precipitates continually rained down from the front for fractures inclined at 90°, a critical mass of precipitates was required for inclination of 45° to 75° case. When a critical mass was obtained, the precipitates slid down the inclined fracture plane and collected near the inlet of the fracture. This was not observed for fractures inclined at 15° or 30°. This suggests that the coefficient of static friction for the precipitates is between  $\tan(30^\circ)$  and  $\tan(45^\circ)$ , though one must also account for viscous drag forces from the flowing solutions.

The observations from the miscible nonreactive fluids (Figure 3.3) also provide insight into the behavior of the two miscible reactive fluids when simultaneously pumped into a fracture for different angles of inclination. As in the non-reactive case, the less dense fluid was eventually confined to a narrow runlet as the denser fluid filled the fracture. As a result, the precipitation formation was restricted to a narrow path along the less dense fluid runlet once the dense fluid front moved through the sample (Figure 3.10). For the range of inclination angles studied: (1) the thickness of precipitation in the runlet increased with increasing angle, and (2) area of the blue-region of precipitation varied with inclination angles. By measuring the area of blue-region of precipitation in the 15° and 30° case (Figure 3.10), it is found to be consistent with the nonreactive case: area of precipitation is larger in 15° than in 30° (See Figure 3.3). The areal extent of precipitate was not measured for the 45°, 60°, 75° and 90° cases because a considerable amount of the precipitates sedimented towards the bottom of a sample, resulting in a random loss of the area

of blue precipitation. From the observation that the sedimentation of precipitation occurred near the runlet, it suggests that more precipitation formed in those areas. In summary, in a uniform aperture fracture: (1). Unimpeded sedimentation occurs at an inclination angle of  $90^\circ$ ; (2). When the inclination angle  $\theta > 30^\circ$ , precipitates slide down the fracture; (3). When  $\theta$  is between  $45^\circ$ - $90^\circ$ , precipitates collect near the inlet; (4). When  $\theta < 30^\circ$ , precipitates achieve almost complete coverage of the fracture plane.

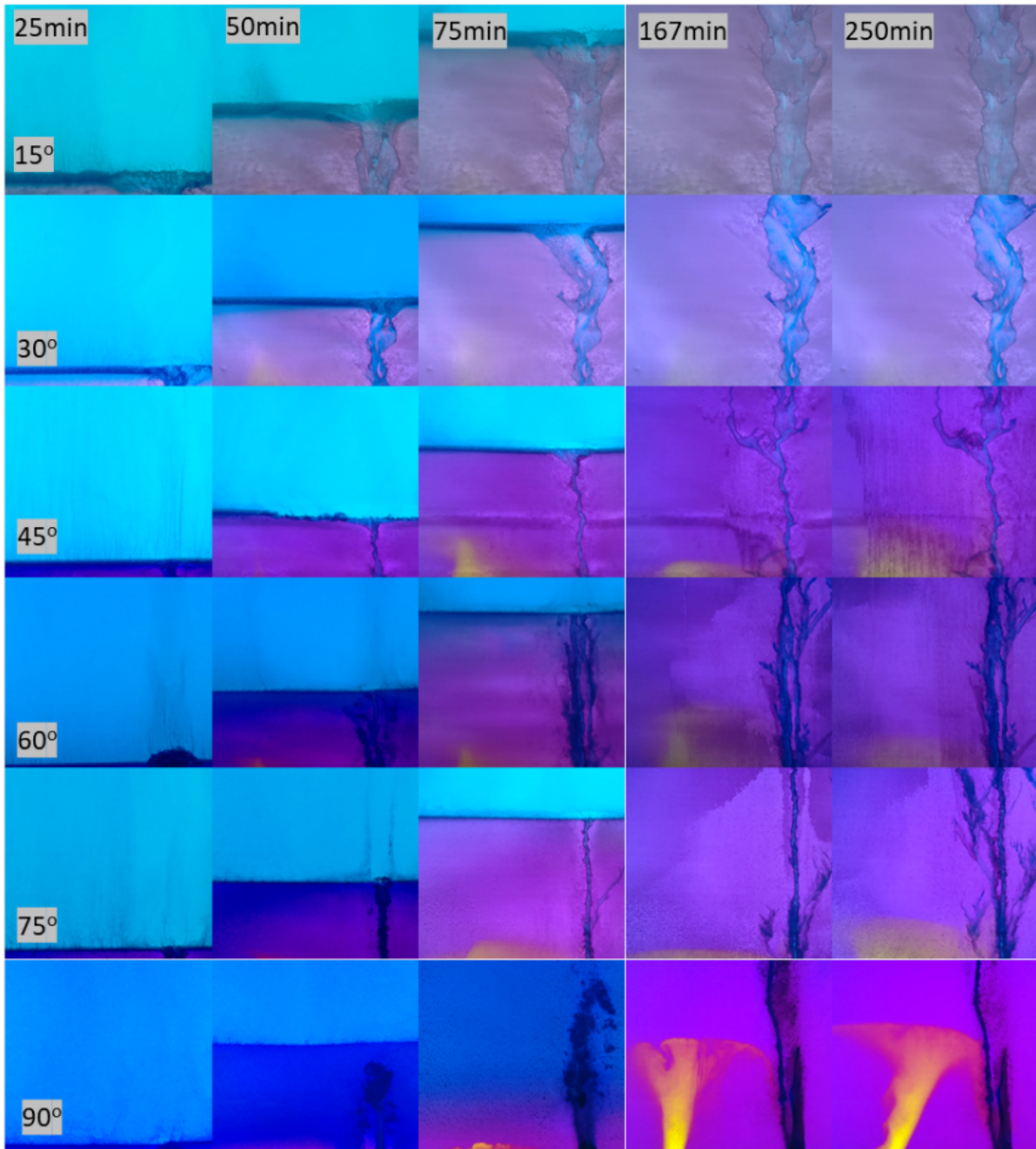


Figure 3.10 Images of reactive miscible fluids mixing with different angles of inclination at time  $T=25, 50, 75, 167, 250$  minutes. Aperture is 2 mm; pumping rate is 0.17 ml/min for both Solution 1 and 2; density contrast is 1111/1031.8

Table 3.5 Area of blue precipitation

Angles of inclination (°)	15	30
Area of blue precipitation (mm <sup>2</sup> )	806.04	451.09

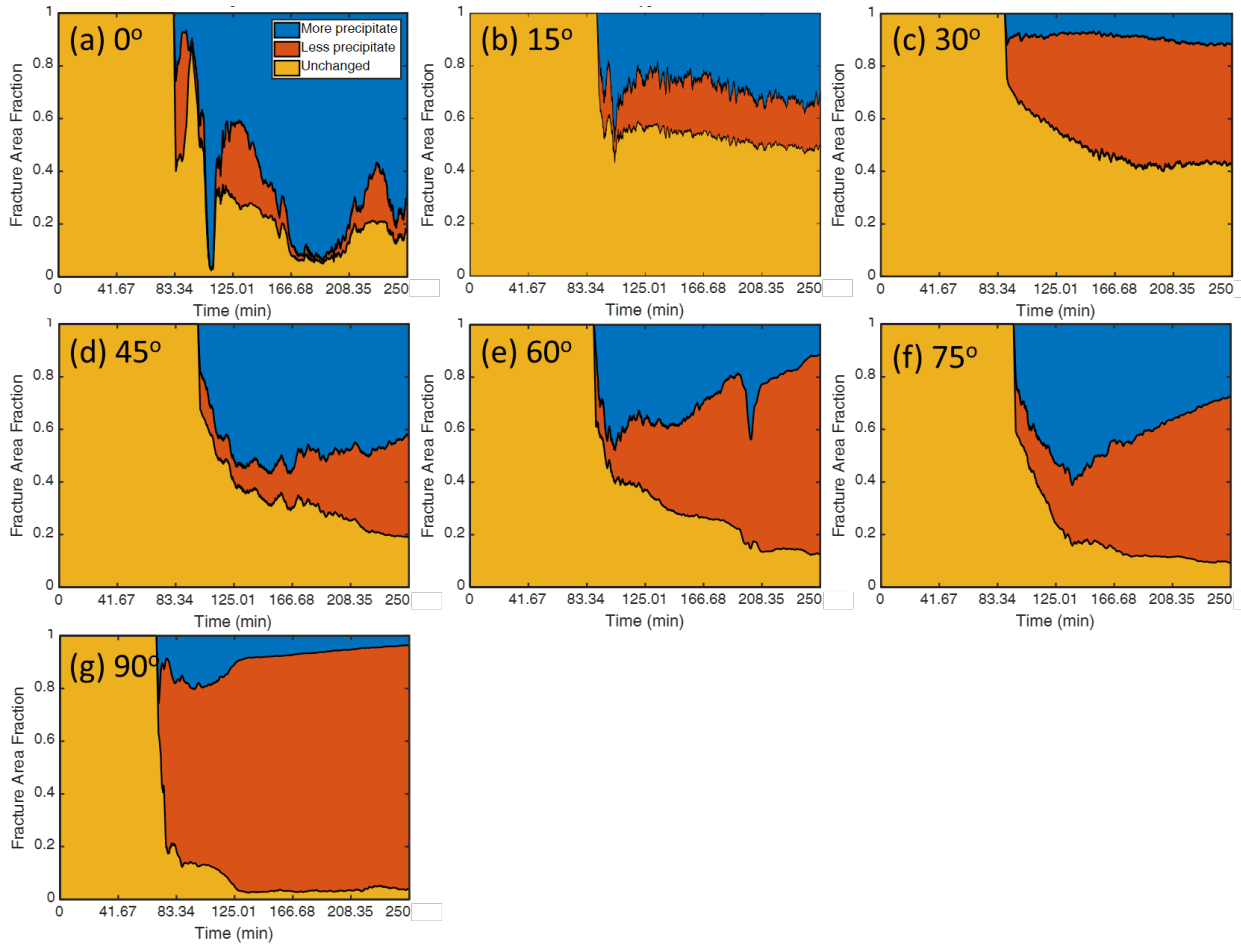


Figure 3.11 Fracture Area Fraction of precipitate amount change over time relative to the time when reaction front reached the entire fracture plane. Aperture is 2 mm; pumping rate is 0.17 ml/min for both Solution 1 and 2; density contrast is 1111/1031.8.

To quantitatively show the change in the amount and spatial distribution of precipitates, the ratio of the area of precipitate at a given time over the area from the time when reaction front reached the entire fracture plane was analyzed (Figure 3.11). The reference image was taken after the reaction front reached the outlet. This reference image was used to subtract the sequential images. Since precipitation blocks light that is transmitted through the fracture, the pixel value

decreases. All negative numbers indicate less precipitation or sedimentation, while positive numbers indicate more precipitation occurred in a region. The analysis classed the subtracted values as either more precipitate, less precipitate, or equal precipitate. Figure 3.12 shows the area fraction of precipitate during the experiments for different inclination angles. Regions with less precipitates increases with inclination angles. At  $\theta=90^\circ$ , the majority of the fracture plane (93%) lost precipitation compared to after the passage of the reaction front (83 min).  $\theta=60^\circ$  is the next angle that also exhibited a large (73.94%) loss of precipitates across the fracture plane, while  $\theta=75^\circ$  showed 62.65% loss of precipitates. The loss of precipitates was significantly lower for  $45^\circ$  (36.99%),  $30^\circ$  (51.07%),  $15^\circ$  (16.72%) and  $0^\circ$  (14.18%). The loss of precipitation is mainly caused by sedimentation especially at large inclination angles. For small inclination angles, for example  $15^\circ$ , the change is relatively small with the areas with more precipitate increasing slightly over time and the areas with less and equal precipitate showing a slight decrease.  $\theta=0^\circ$  is quite different from the other angles. No sedimentation towards the outlet occurs. The precipitate lost mainly arises from transport of precipitates out of the fracture. The majority of the areas (66.19%) have more precipitate compared to the reference image. Recall the simulation results [21] that a gravity tongue of lighter **Solution 2** would form at this angle, which aids the potential for mixing of two solutions over the fracture plane and thus the formation of more precipitates.

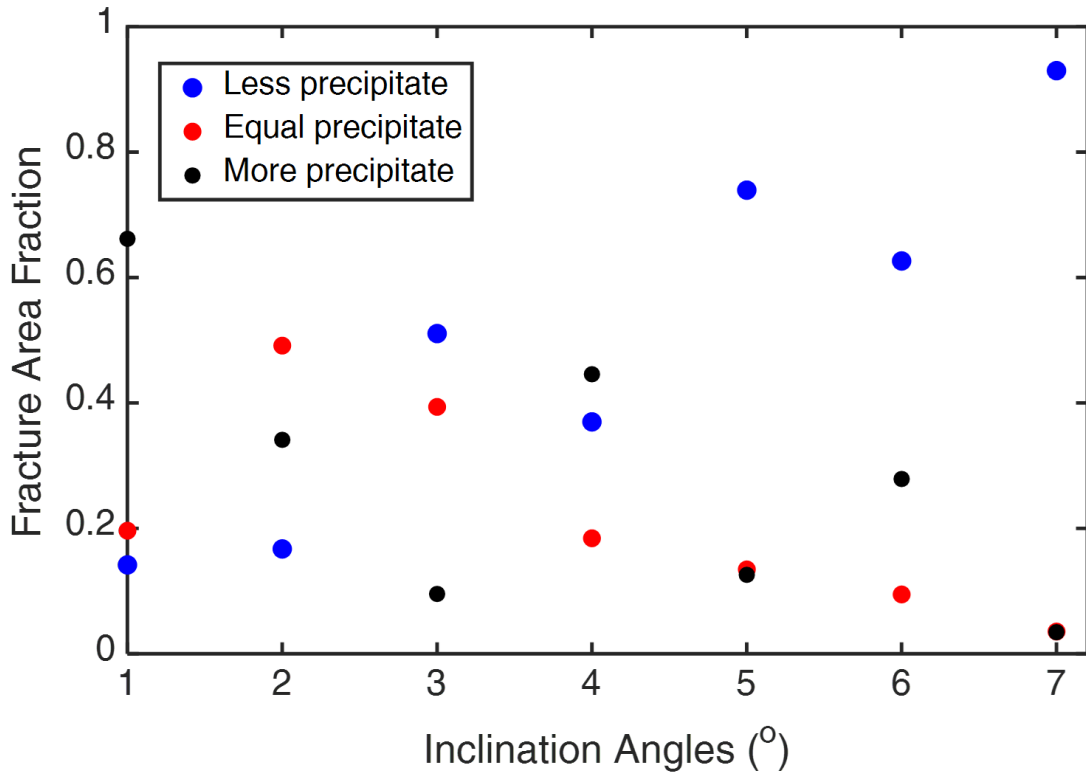


Figure 3.12 Fracture Area Fraction of precipitate amount change in the end of experiments for different inclination angles. Aperture is 2 mm; pumping rate is 0.17 ml/min for both Solution 1 and 2; density contrast is 1111/1031.8.

In order to show more details related to sedimentation, the case  $\theta=60^\circ$  was examined. There is a sudden increase of more than 20% of the area with more precipitates while the overall trend is decreasing in area of more precipitates near 200 minutes (Figure 3.11(e)). A series of representative raw and corresponding processed images from different times are shown (Figure 3.13) to illustrate the change in precipitate distribution over time. Figure 3.13 shows the change in area of precipitates using three colors. White indicates regions with less precipitation compared to reference image. Purple indicates that the amount of precipitate is unchanged. Yellow regions exhibited an increase in precipitation. Figure 3.13 (a) and (g) were at 104 minutes, which show a status that shortly (~15mins) after the reaction front covered the entire fracture. The majority of the fracture (51.35%) has more precipitation, while the region in the runlet lost some precipitation

is because it is still a short time since the reaction started. Figure 3.13 (b) and (h) show the area at 166.67 minutes, when precipitation continues to decrease. It can be seen that the regions near the runlet, the central of the fracture plane, and near the inlet of **Solution 1** lost precipitation. The continuous increase in regions with less precipitates resulted from sedimentation of precipitation after a threshold amount was achieved. The areas with more precipitates are at the side of, and near the center bottom of the fracture plane. Figure 3.13 (c-e) and (i-k) show 3 consecutive images after 197 minutes 20 seconds (197'25", 197'30" and 197'35"). Two vertical strips of precipitates formed from central upper position and continued to grow towards the bottom. Precipitates sedimented downward from the outlet. When the precipitates accumulated at the bottom of the fracture, this resulted in more precipitates in this region near the left bottom part, and thus increased the areas with more precipitation. Figure 3.13 (f) and (l) show the fracture plane at 250 minutes which is near the end of the experiment. The images show that the majority of the fracture plane has less precipitates compared to the reference image. This series of images show that even if more precipitates formed continuously, under gravity, the precipitates can sediment downward and leave the most of the fracture plane unfilled.

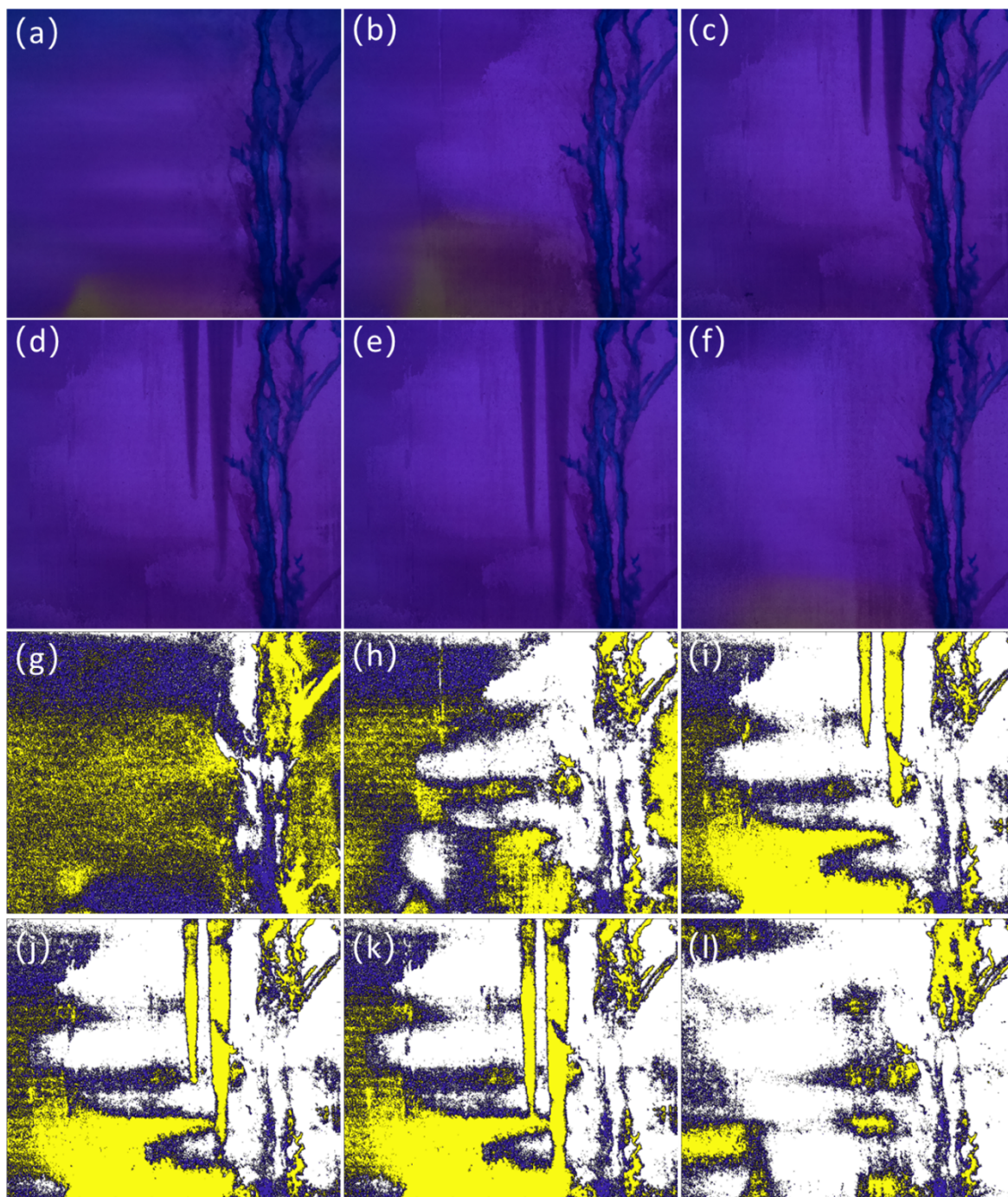


Figure 3.13 (a)-(f) Unprocessed images of precipitation for  $\theta=60^\circ$ . (g)-(l) Area of precipitation change relative to reference image for  $\theta=60^\circ$  in three colors. White means the area with less precipitation compared to reference image. Purple means the amount of precipitation on the area is unchanged. Yellow means the area with more precipitation. (a) (g) Time=104.17 minutes; (b) (h) Time=166.67 minutes; (c) (i) Time=197 minutes and 25 seconds; (d) (j) Time=197 minutes and 30 seconds; (e) (k) Time=197 minutes and 35 seconds; (f) (l) Time=250 minutes. Aperture is 2 mm; pumping rate is 0.17 ml/min for both Solution 1 and 2; density contrast is 1111/1031.8.

### 3.3.2 Influence of Aperture

#### 3.3.2.1 Mixing of Non-reactive Miscible Fluids in a Uniform Aperture Fracture

Another factor that affects the fluid mixing and precipitate distribution is the fracture aperture. To investigate the influence of aperture, all other properties such as pumping rate, density contrast, fracture inclination angle were maintained constant. The parameters are listed in Table 3.6.

Table 3.6 Parameters for studying influence of aperture.

Aperture (mm)	Pumping rate (ml/min)	Density of Solution 1 (kg/m <sup>3</sup> )	Density of Solution 2 (kg/m <sup>3</sup> )	Viscosity of Solution 1 (Pa-s)	Viscosity of Solution 2 (Pa-s)	Fracture inclination angle (°)
1	0.17	1.36	1111	1031.8	1.20x10 <sup>-3</sup>	1.11x10 <sup>-3</sup>
2						
4						

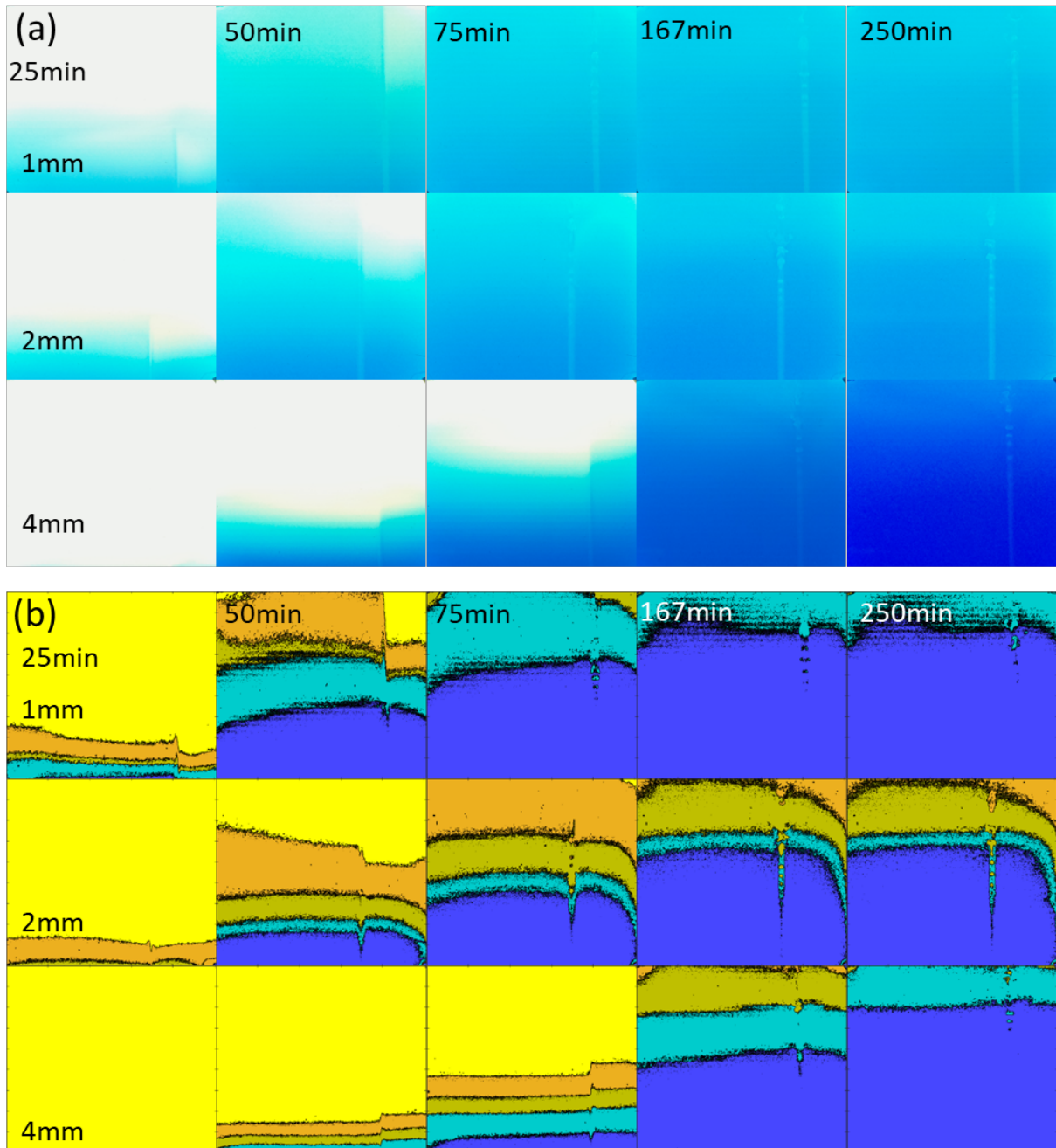


Figure 3.14 (a) Digital images from non-reactive miscible fluid mixing experiments (b) Processed images from non-reactive miscible fluid mixing experiments. Fluids have been represented with 5 range concentration of Solution 1: Yellow: <25%; Orange: 25%-50%; Olive: 50%-75%; Cyan: 75%-100%; Blue: ~100%. Each row shows images from a different aperture. Each column represents different times during the experiments (25, 50, 75, 167 and 250 mins after start pumping both fluids). Inclination angle is  $90^\circ$ ; pumping rate is 0.17 ml/min for both Solution 1 and 2; density contrast is 1111/1031.8.

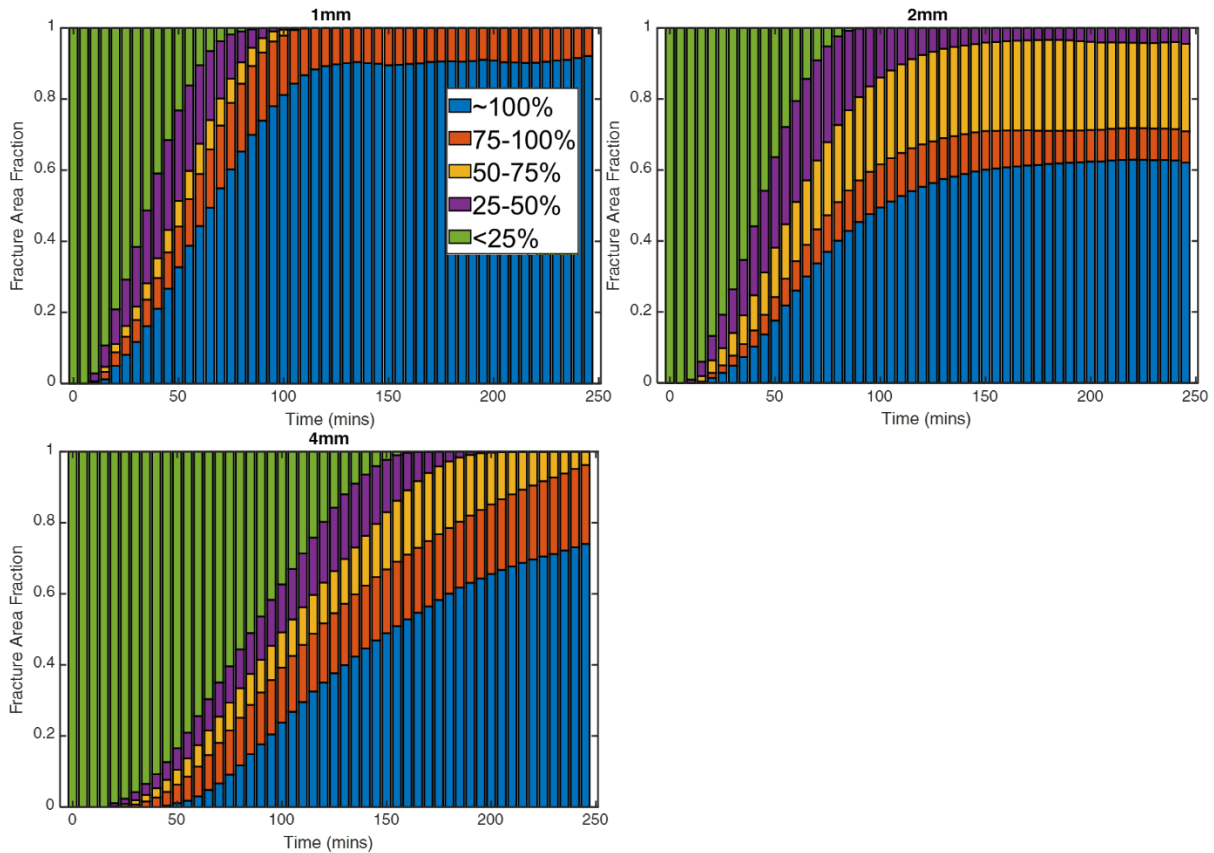


Figure 3.15 Fracture area fraction of different concentration fluids in terms of Solution 1 by weight over time for different apertures. Inclination angle is  $90^\circ$ ; pumping rate is 0.17 ml/min for both Solution 1 and 2; density contrast is 1111/1031.8.

Fluids mixing is very different in the 3 different uniform aperture fractures. From Figure 3.15, in 1mm aperture, initially 100% of the fracture was covered by a fluid concentration of <25% of **Solution 1** and soon was covered with all other concentration fluids other than <25% after start pumping both fluids for about 60 minutes. Except for 75-100% and ~100% concentration fluid, the areas all of other concentration fluids decreased to 0 after 84 minutes. In this case, only ~100% concentration fluid remained occupying more than 90% area until the end of experiment. It showed a poor mixing situation. The narrow aperture cannot provide enough space for two fluids to mix and results in strong confinement of the less dense fluid by the denser fluid. Since the pumping rate is the same for different apertures, the velocities of fluids relative to the aperture are the largest

in 1 mm aperture, which led to smaller fluid resident times, that results in a final fluid with 75-100% and ~100% concentrations of Solution 1 occupying the entire fracture.

In contrast to 1mm aperture case, 2 mm and 4 mm apertures achieved better mixing. Both fractures had more area with concentration other than 75-100% and ~100% in the end. The 2 mm aperture seemed to have the best mixing among the 3 apertures with fluid concentrations of **Solution 1** from 25%-100%. Compared to 4 mm aperture, there was nearly only 75%-100% concentration fluids at the end. Larger aperture and relatively low fluid velocity provided an environment for heavier fluids to accumulate in the aperture from the bottom, and therefore enabled the lighter fluid to be displaced from the fracture. This demonstrated that larger apertures do not lead to better mixing.

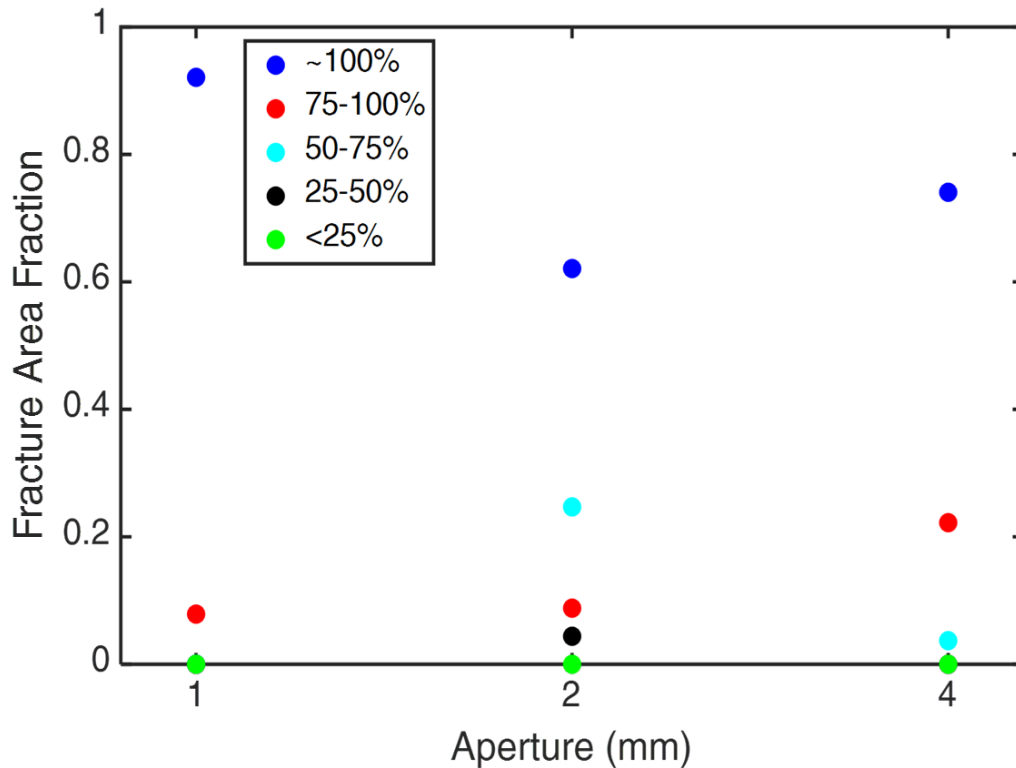


Figure 3.16 Fracture Area Fraction at T=250 minutes for different apertures. Inclination angle is 90°; pumping rate is 0.17 ml/min for both Solution 1 and 2; density contrast is 1111/1031.8.

Another effect of aperture on the fluid mixing is the stability of the less dense fluid runlet. Figure 3.17 shows the runlet of less dense fluid evolves over time in fracture apertures of 1 mm, 2 mm and 4 mm for 2 different flow rates. Images were processed to enhance the runlet geometry by subtracting the background. The formation and stability of the runlet depended on the location of the dense fluid front, fracture aperture and flow rate. After the passage of the denser fluid front, no instabilities were observed in the less dense runlet in the 1 mm aperture fracture, unlike that observed for the 2 & 4 mm aperture fractures. For the high flow rate of 1.36 ml/min in the 2 & 4 mm aperture fractures, the runlet exhibits turbulent features though the Reynolds number is very low (see Table 3.7). The instabilities arise from density and velocity contrasts between the two fluids, and from concentration differences that occur as the two solutions mix.

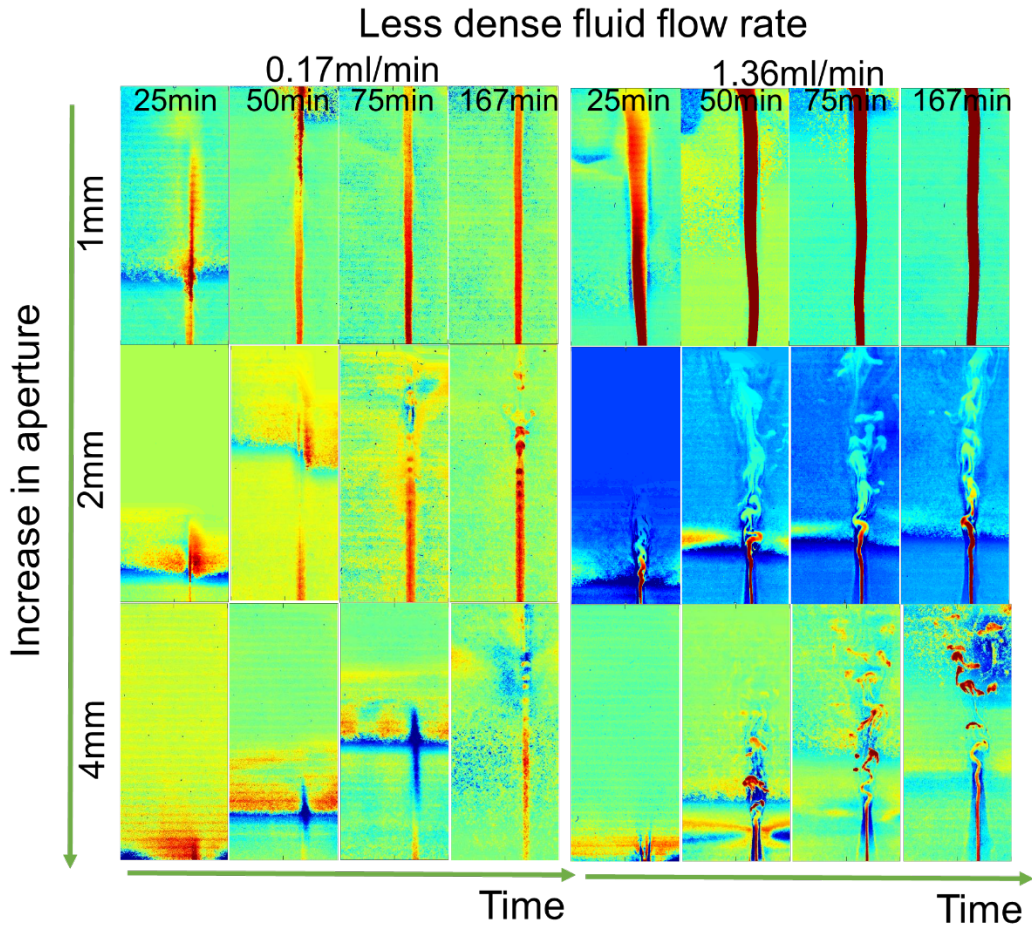


Figure 3.17 Shape of less dense fluid at different aperture and pump rate of Solution 2. Inclination angle is  $90^\circ$ ; pumping rate of Solution 1 is 0.17 ml/min; density contrast is 1111/1031.8.

Table 3.7 Table of dimensionless numbers

	Schmidt (Sc)		Atwood (At)		Viscosity ratio ( $m=\mu_2/\mu_1$ )	
	$1.05 \times 10^4$		0.037		0.9	
Aperture	1 mm		2 mm		4 mm	
Less dense fluid flow rate (ml/min)	0.17	1.36	0.17	1.36	0.17	1.36
Reynolds (Re)	1.34	10.92	1.34	10.82	2.02	16.39
Froude (Fr)	0.0142	0.1154	0.0050	0.0400	0.0027	0.0217
Peclet (Pe)	$1.40 \times 10^4$	$1.14 \times 10^5$	$1.40 \times 10^4$	$1.14 \times 10^5$	$2.12 \times 10^4$	$1.72 \times 10^5$

### 3.3.2.2 Reactive Mixing of Miscible Fluids in a Uniform Aperture Fracture

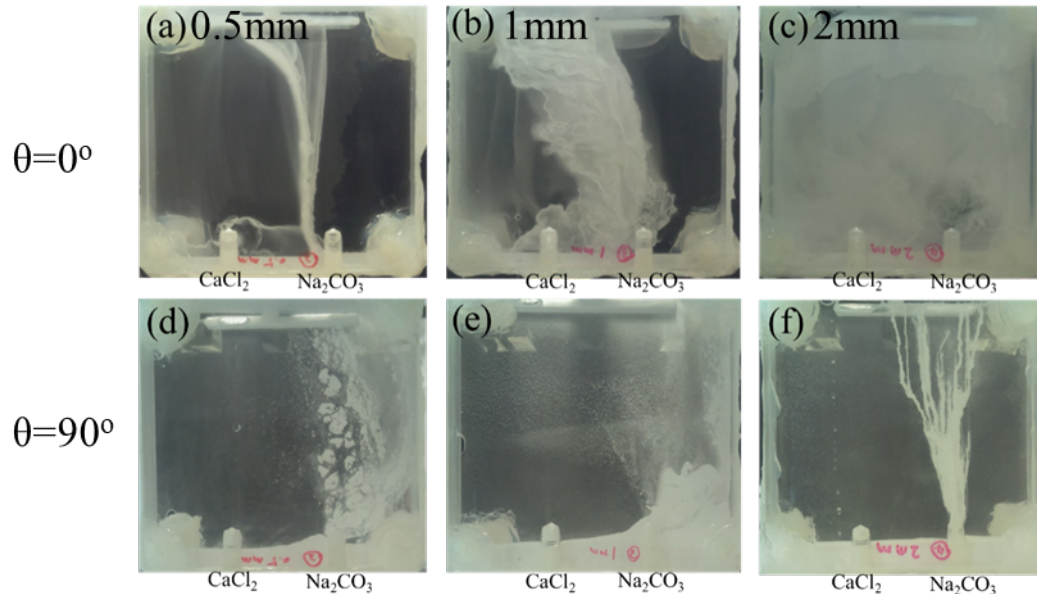


Figure 3.18 Precipitate distribution in horizontal fracture (inclination angle  $\theta=0^\circ$ ) with different apertures: (a) 0.5mm; (b) 1mm; (c) 2mm. and in vertical fracture (inclination angle  $\theta=90^\circ$ ) with different apertures: (d) 0.5mm; (e) 1mm; (f) 2mm.

Reactive mixing experiments were also performed on uniform aperture fracture samples with fracture apertures of 0.5 mm, 1 mm and 2 mm. The fracture was oriented either horizontally (inclination angle  $\theta=0^\circ$ ) or vertically (inclination angle  $\theta=90^\circ$ ), and was initially saturated with  $\text{Na}_2\text{CO}_3$  solution (less dense **Solution 2**). After pumping 50ml  $\text{CaCl}_2$  (denser **Solution 1**) and 50ml  $\text{Na}_2\text{CO}_3$  solutions, precipitate distributions were very different for the different apertures. As for the result of vertical fracture (Figure 3.18), in the 0.5 mm aperture, the precipitate is fragmented; in 1 mm aperture, the precipitate is widely spread and powdery; in the 2 mm aperture, the precipitate is restricted to narrow paths and the good development of runlet appears. The strong fragmented and powdery precipitates in 0.5 and 1 mm aperture fractures are caused by the narrow aperture space. Precipitates formed near the runlet blocked the pathway of **Solution 2** and the pressure built up until **Solution 2** broke the precipitates apart. Then under gravity, the precipitates sedimented to the right bottom of the fracture. This can also be supported by the results from

horizontal fracture experiments. In 0.5 mm and 1 mm horizontal aperture, the precipitate mainly occurred in the middle of two inlet, where the two solutions mixed well. Precipitates blocked the mixing lines so no more precipitates can form in other areas. Figure 3.18 (a) had a smaller area of precipitates than (b), because (b) has a larger aperture, and it takes longer and more precipitates to block the mixing line. While in the 2mm aperture, precipitate spread over the entire fracture plane due to the enough space for less dense fluid **Solution 2** to ride on top of **Solution 1**. The aperture of the fracture and fracture orientation have a significant effect on precipitate distribution by affecting the mixing lines.

### 3.3.3 Influence of Density Contrast

#### 3.3.3.1 Mixing of Non-reactive Miscible Fluids in a Uniform Aperture Fracture

The results shown above are all gravity driven. Gravity plays an important role because there is a density difference between the two fluids. Therefore, it is also important to investigate the effects of the density contrast between the two fluids. All other properties such as aperture, pumping rate, fracture inclination angles were maintained constant in the following experiments.

The parameters are listed in Table 3.8.

Table 3.8 Parameters for studying influence of density contrast.

Aperture (mm)	Pumping rate (ml/min)	Density of Solution 1 (kg/m <sup>3</sup> )	Density of Solution 2 (kg/m <sup>3</sup> )	Fracture inclination angle (°)
		1111	1000	
2	0.17	1200	1000	90
		1400	1000	
		1800	1000	

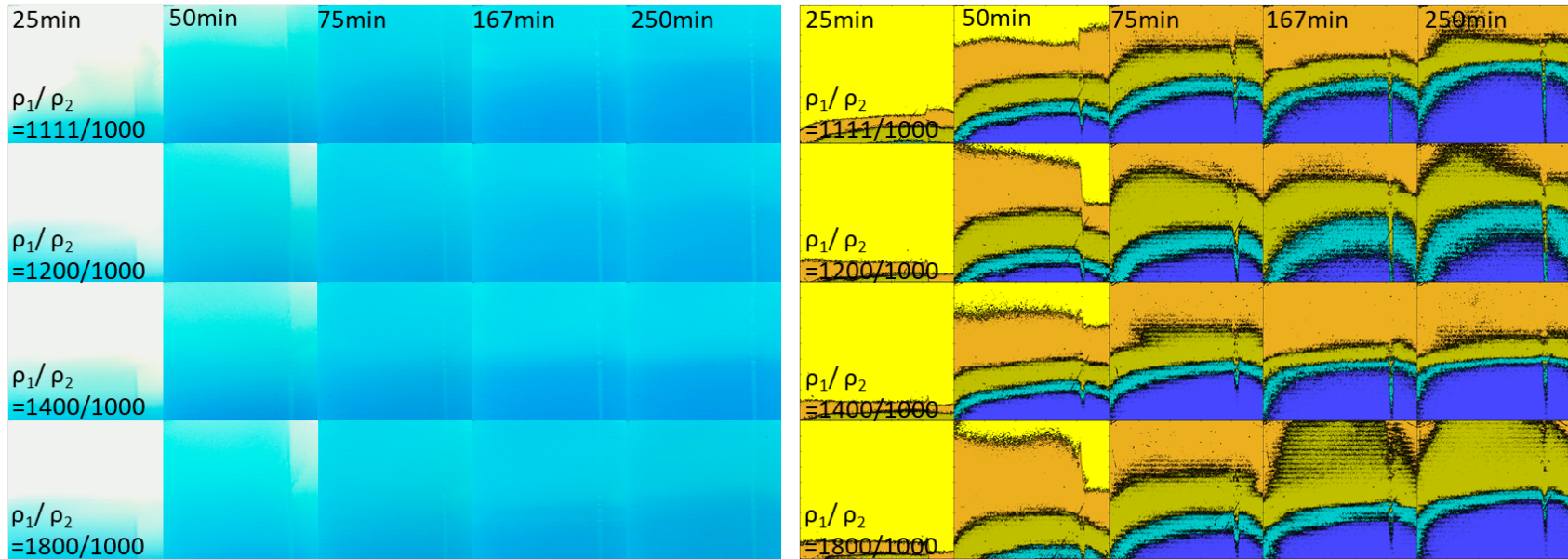


Figure 3.19 (left) Digital images from non-reactive miscible fluid mixing experiments. (right) Processed images from non-reactive miscible fluid mixing experiments. Fluids have been represented with 5 range concentration of Solution 1: Yellow: <25%; Orange: 25%-50%; Olive: 50%-75%; Cyan: 75%-100%; Blue: ~100%. Each row shows images from a different density contrast. Each column represents different times during the experiments (25, 50, 75, 167 and 250 mins after start pumping both fluids). Inclination angle is  $90^\circ$ ; aperture is 2 mm; pumping rate is 0.17 ml/min for both Solution 1 and 2

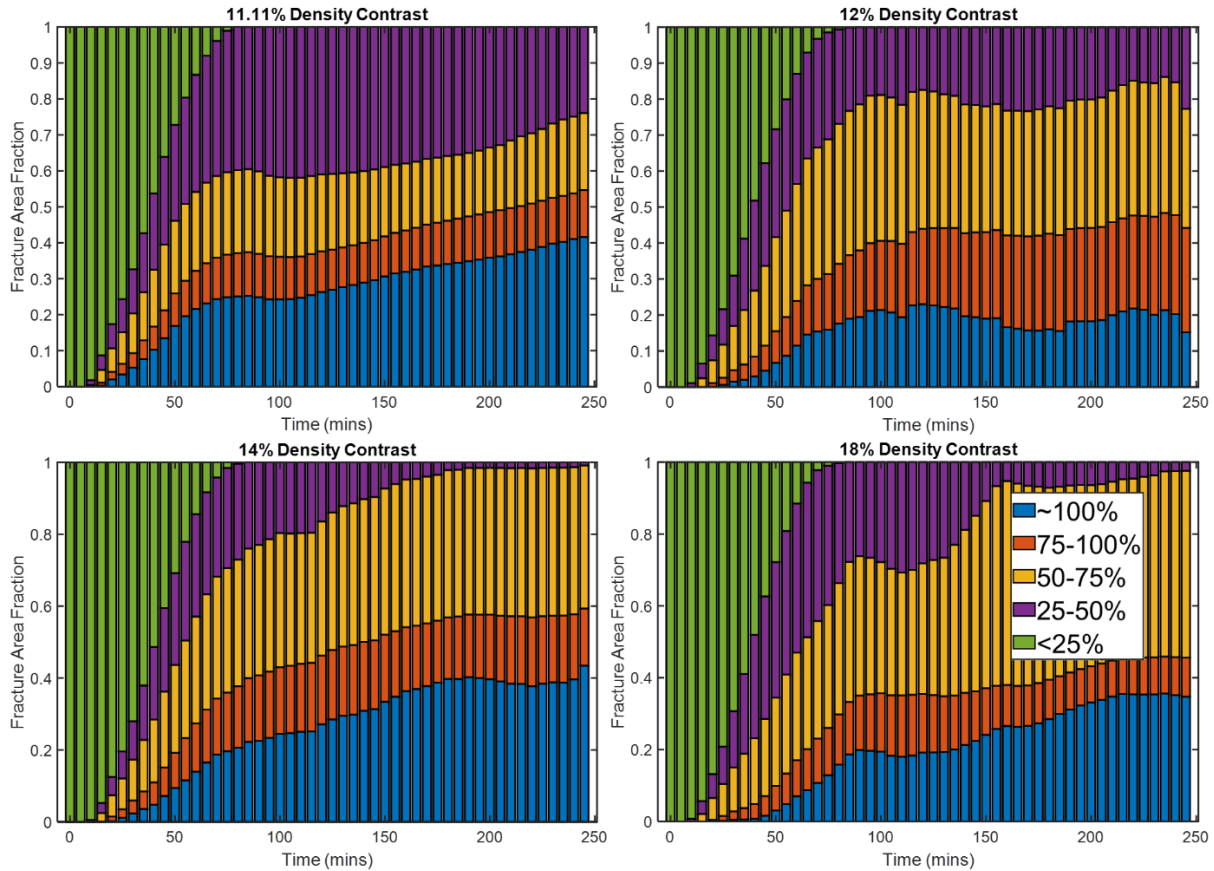


Figure 3.20 Fracture area fraction of different concentration fluids in terms of Solution 1 by weight over time for different density contrast. Inclination angle is  $90^\circ$ ; aperture is 2 mm; pumping rate is 0.17 ml/min for both Solution 1 and 2

Figure 3.20 shows that the density contrast results in different stratification for the different concentration fluids. For an 11.11% density contrast, the majority of the fracture was occupied by fluids with 25-50% and ~100% concentrations of **Solution 1**, while for a 12% density contrast case, fluids with different concentration of **Solution 1** occupied the fracture more evenly. 14% and 18% density contrast had more area of fluid with  $>50\%$  concentration of **Solution 1**.

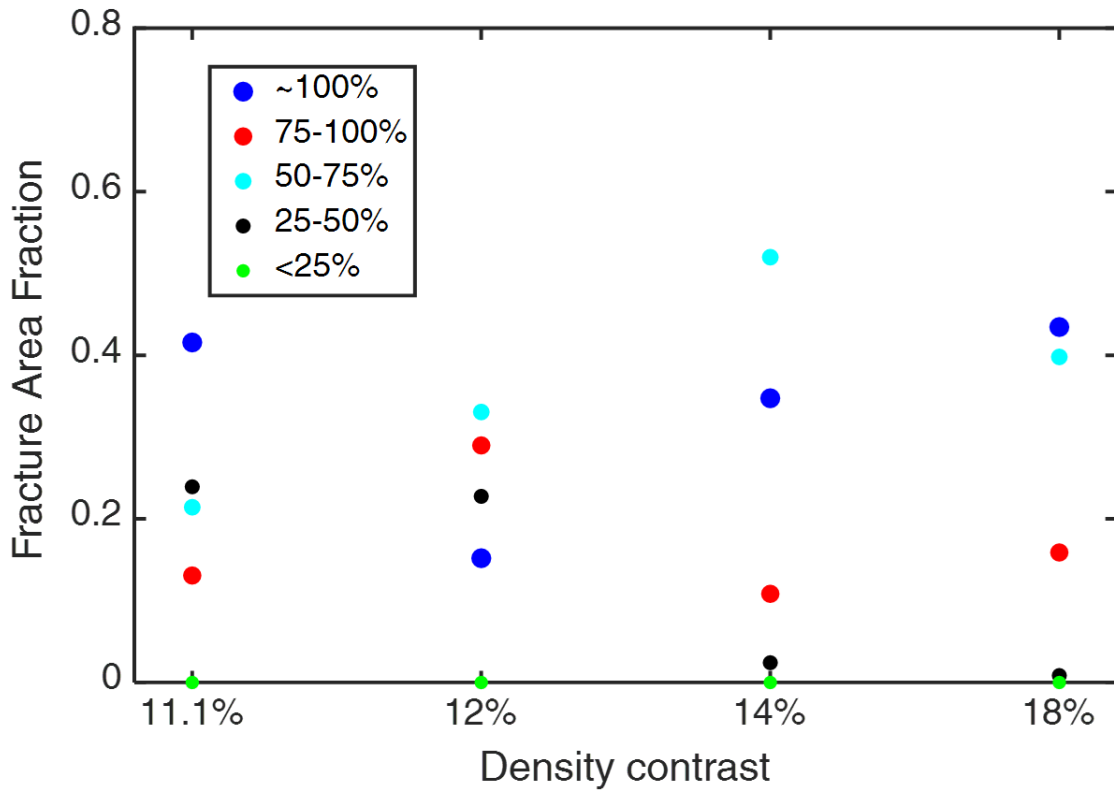


Figure 3.21 Fracture Area Fraction at T=250 minutes for different density contrast. Inclination angle is 90°; aperture is 2 mm; pumping rate is 0.17 ml/min for both Solution 1 and Solution 2.

Another aspect is the width of the less dense fluid runlet. The fact that it is formed due to the density contrast implies that changing the density contrast might affect its property. Therefore, runlet width was measured for fluids with different density contrast. Figure 3.22 and Table 3.9 show the result.

Table 3.9 Width of less dense fluid runlet for different density contrast.

Density of Solution 1 (kg/m <sup>3</sup> )	Density of Solution 2 (kg/m <sup>3</sup> )	Width of less dense fluid runlet (mm)
1111	1000	1.41
1200	1000	1.52
1400	1000	1.58
1800	1000	1.81

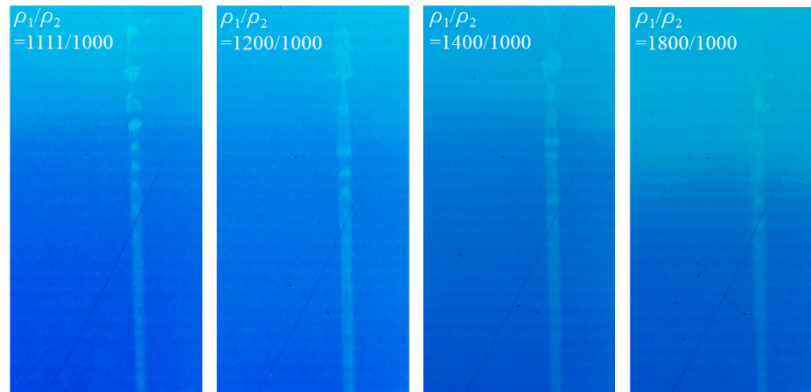


Figure 3.22 Less dense fluid runlet of different density contrast. Inclination angle is 90°; aperture is 2 mm; pumping rate is 0.17 ml/min for both Solution 1 and 2

The result showed that the runlet width increased with the increase in density contrast. This might be caused by the increase in the pressure difference between the less dense and denser fluid, which led to larger diffusion that in turn widened the width of the runlet. Notice that for larger density contrast (e.g. Figure 3.22  $\rho_1/\rho_2=1800/1000$ ), the stratification is also more obvious (by observing the height of deep blue color. Larger density contrast resulted in shorter height of the deep blue color).

### 3.3.3.2 Reactive Mixing of Miscible Fluids in a Uniform Aperture Fracture

Reactive mixing experiments were also performed on uniform aperture fracture samples to determine the effect density contrast of the solutions on precipitate distribution. Parameters are listed in Table 3.10.

Table 3.10 Parameters for studying influence of density contrast.

Aperture (mm)	Pumping rate (ml/min)	Density of Solution 1 (kg/m <sup>3</sup> )	Density of Solution 2 (kg/m <sup>3</sup> )	Fracture inclination angle (°)
		1111	1031.8	
2	0.17	1111	1071	90
		1111	1111	

Experiments show that the density contrast controls the location of the precipitate formation. The fracture was initially saturated with less dense **Solution 2** (Na<sub>2</sub>CO<sub>3</sub>), and then both solutions were pumped into the fracture simultaneously with the same pumping rate. A reaction front was observed (Figure 3.23(a)). This reaction front is a white horizontal line with whitish fingering (Figure 3.23(a)). The reaction front and plumes are only seen during the early stage of the experiment. Once the reaction front reaches the outlet, all of these phenomena cease, and only precipitates continue to accumulate along the mixing line between the two solutions. Three different solution density contrasts were tested: (1).  $\rho_1/\rho_2=1.07$  ( $\rho_1=1111\text{kg/m}^3$ ,  $\rho_2=1031.8\text{kg/m}^3$ ); (2).  $\rho_1/\rho_2=1.04$  ( $\rho_1=1111\text{kg/m}^3$ ,  $\rho_2=1071\text{kg/m}^3$ ); (3).  $\rho_1/\rho_2=1$  ( $\rho_1=1111\text{kg/m}^3$ ,  $\rho_2=1111\text{kg/m}^3$ ). The results are as follows:

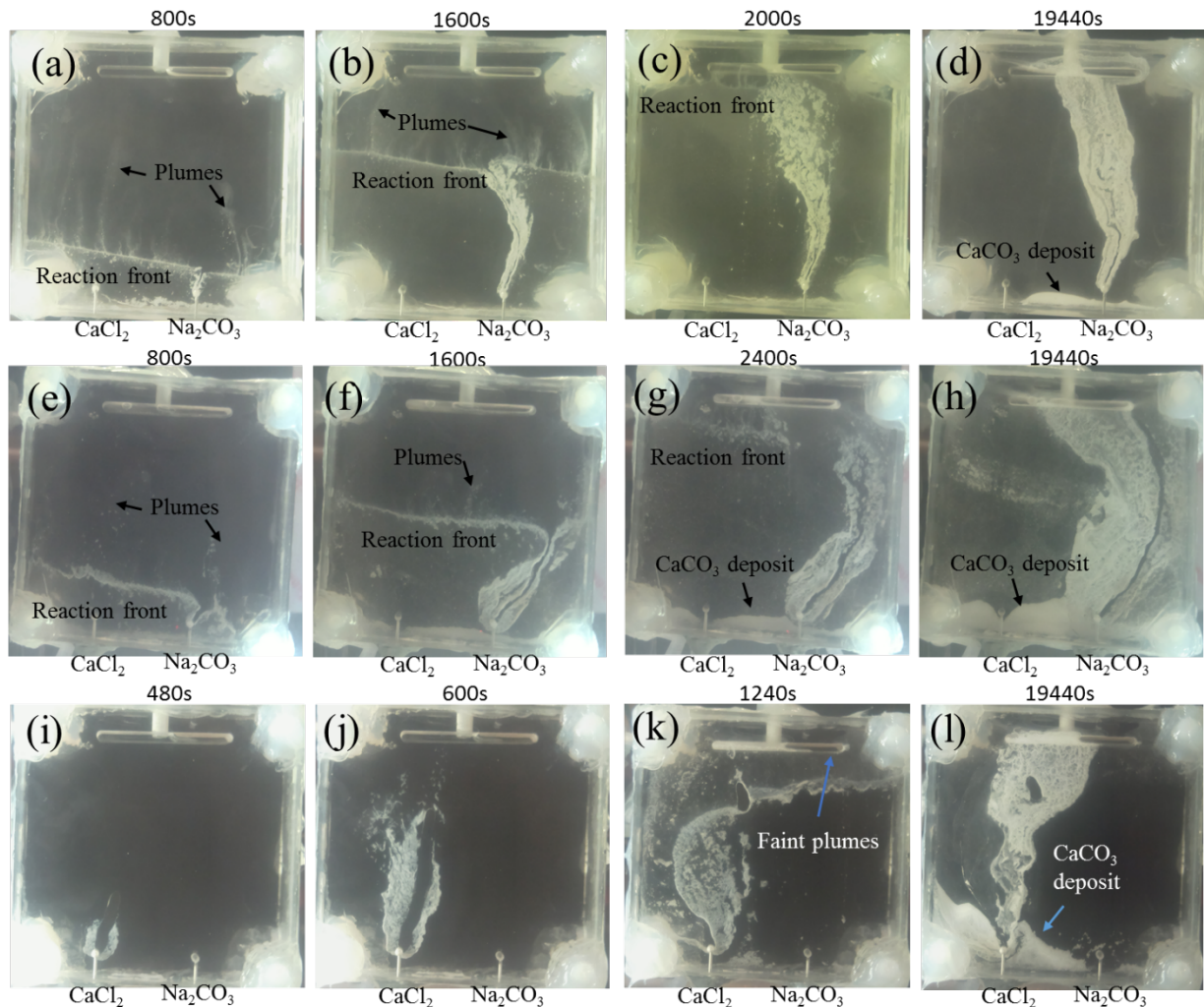


Figure 3.23 Different stages of the uniform aperture fracture precipitation after start pumping both solutions for  $\rho_1/\rho_2=1.07$ : (a) 800s; (b) 1600s; (c) 2000s; (d) 19440s; for  $\rho_1/\rho_2=1.04$ : (e) 800s; (f) 1600s; (g) 2400s; (h) 19440s; for  $\rho_1/\rho_2=1$ : (i) 480s; (j) 600s; (k) 1240s; (l) 19440s. Inclination angle is  $90^\circ$ ; aperture is 2 mm; pumping rate is 0.17 ml/min for both Solution 1 and 2

Figure 3.23 (a) – (d) show the different stages of precipitation in a uniform aperture fracture for  $\rho_1/\rho_2=1.07$ . The whitish faint plumes emanating from the reaction front are observed in Figure 3.23 (a) and (b). The fine finger plumes flow along the stream lines of the system. Some precipitates fall from the reaction front to the bottom inlet similar to what was shown in section 3.3.1.2. As the experiment continues, precipitation increases on the side of  $\text{Na}_2\text{CO}_3$ . At the end of the experiment, a curved precipitation pattern originates from the  $\text{Na}_2\text{CO}_3$  port and is narrow in

lateral extent (covers 13% of the entire area), which is consistent with the phenomenon observed in section 3.3.1.2 and 3.3.2.2.

Figure 3.23 (e) – (h) show the different stages of precipitation in a fracture for  $\rho_1/\rho_2=1.04$ . The entire process is similar to the  $\rho_1/\rho_2=1.07$  case, however the fine finger plumes are less apparent, and the precipitation path is wider than for  $\rho_1/\rho_2=1.07$ . The pattern of the precipitation covers a larger area (29.9% of the entire area) than for  $\rho_1/\rho_2=1.07$ . The only difference between these two experiments is the density of **Solution 2**, which results in different spatial distributions of precipitates.

Figure 3.23 (i) – (l) show the different stages of precipitation for  $\rho_1/\rho_2=1$ . The result of this experiment differs from the previous two experiments. The location of the precipitates is different. For the previous two experiments, precipitates are produced on the side of  $\text{Na}_2\text{CO}_3$  along the runlet of less dense solution, while for  $\rho_1/\rho_2=1$ , precipitates are produced on the side of denser solution  $\text{CaCl}_2$ . It is ascribed to the equal density of the two solutions. Since there was no density difference, the later injection of the  $\text{CaCl}_2$  solution reacts with the initially saturated  $\text{Na}_2\text{CO}_3$  directly and gradually spreads out to react with the newly injected  $\text{Na}_2\text{CO}_3$  solutions. Nevertheless, the pattern of the precipitation is similar to the previous two cases, but on the opposite side (covers 30.7% of the entire area). This suggests that where precipitates form in a fracture can be controlled by adjusting the density contrast of two fluids.

These 3 experiments show that the density difference of the two reactive solutions will also influence the shape and the location of the precipitation formed inside the fracture. Meanwhile, the curved pattern of the precipitation is caused by the streamlines near the outlet.

### 3.3.4 Influence of Pumping Rate

The last parameter examined is the pumping rate of less dense fluid. As mentioned in the references [11-13], flow rate affects resident time of fluids in fracture and can affect precipitates formation. To investigate the influence of less dense fluid pumping rate, all other properties such as aperture, density contrast, fracture inclination angle were maintained constant. The parameters are listed in Table 3.11.

Table 3.11 Parameters for studying influence of pumping rate.

<b>Aperture (mm)</b>	<b>2</b>	<b>Pumping rate of Solution 2 (ml/min)</b>
<b>Density of Solution 1 (kg/m<sup>3</sup>)</b>	1111	0.04
<b>Density of Solution 2 (kg/m<sup>3</sup>)</b>	1031.8	0.08
<b>Viscosity of Solution 1 (Pa.s)</b>	1.20x10 <sup>-3</sup>	0.17
<b>Viscosity of Solution 2 (Pa.s)</b>	1.11x10 <sup>-3</sup>	0.34
<b>Fracture inclination angle (°)</b>	90	0.68
<b>Pumping rate of Solution 1 (ml/min)</b>	0.17	1.36

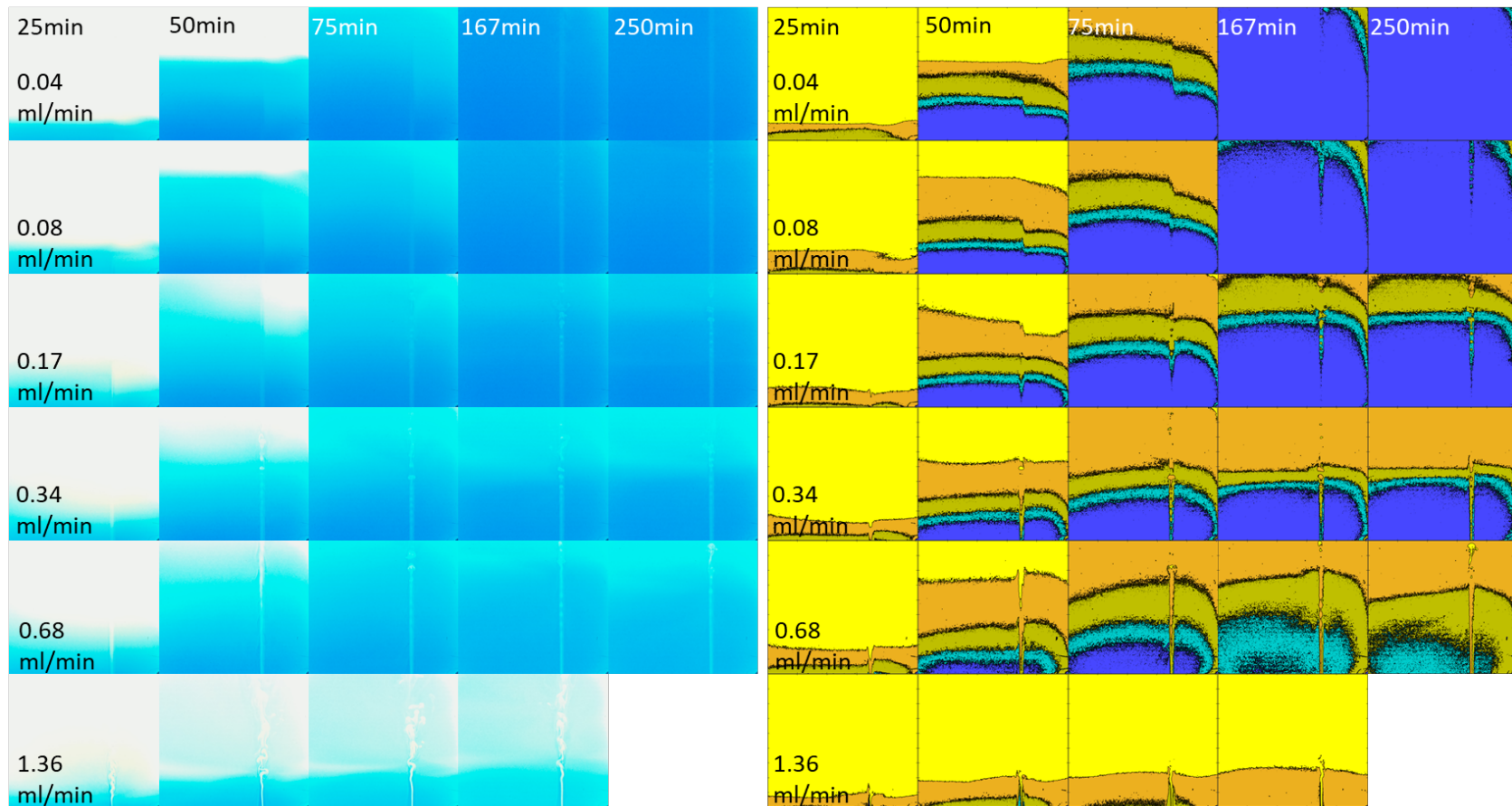


Figure 3.24 (left) Digital images from non-reactive miscible fluid mixing experiments. (right) Processed images from non-reactive miscible fluid mixing experiments. Fluids have been represented with 5 range concentration of Solution 1: Yellow: <25%; Orange: 25%-50%; Olive: 50%-75%; Cyan:75%-100%; Blue:~100%. Each row shows images from different pumping rates of Solution 2.

Each column represents different times during the experiments (25, 50, 75, 167 and 250 mins after start pumping both fluids). Inclination angle is  $90^\circ$ ; aperture is 2 mm; pumping rate is 0.17 ml/min for Solution 1; density contrast is 1111/1031.8. The case of 1.36ml/min pumping rate missing last image because it ran out of fluid due to the size limit of syringe (300 ml).

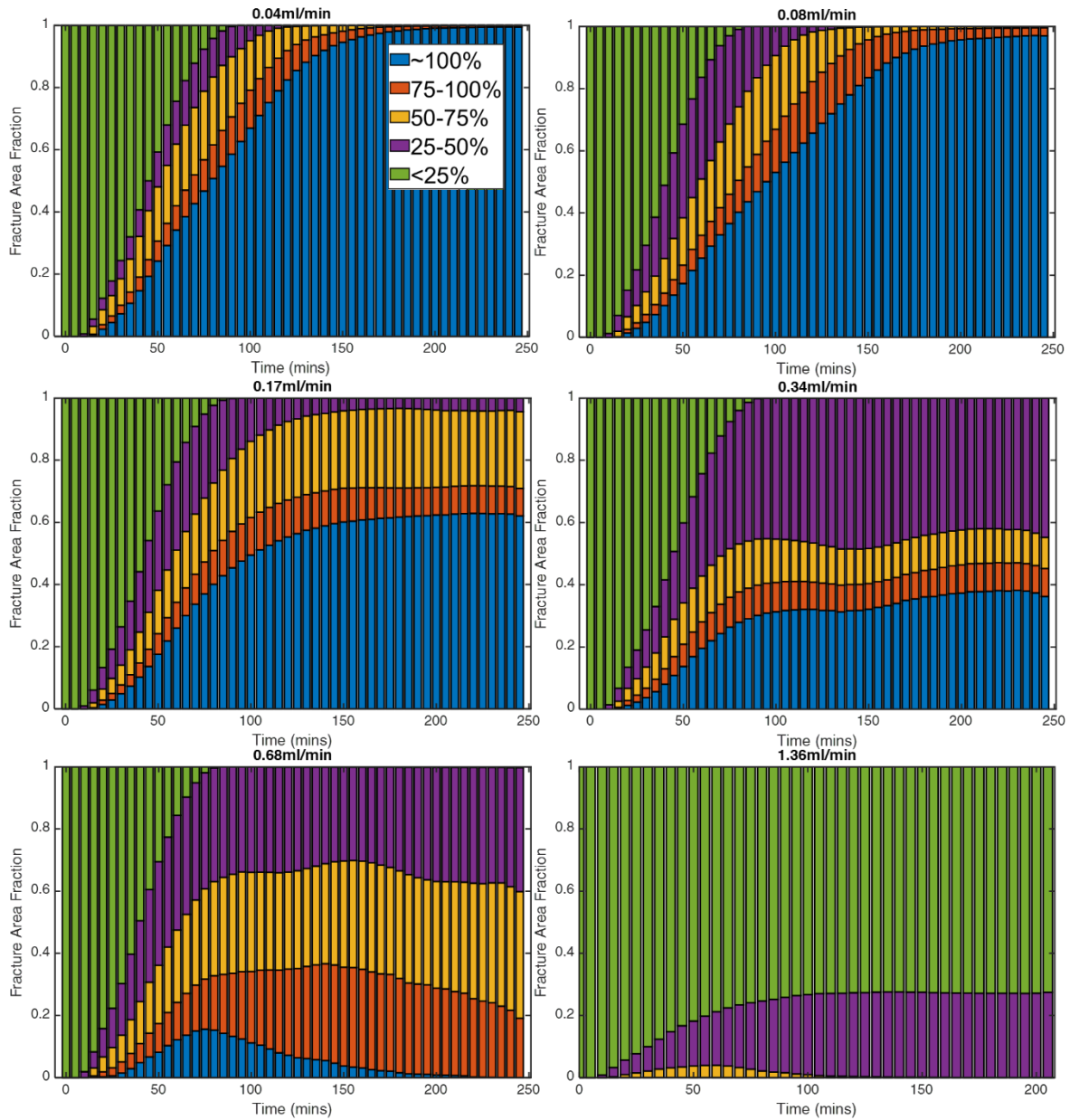


Figure 3.25 Fracture area fraction of different concentration fluids in terms of Solution 1 by weight over time for different pumping rates of Solution 2. Inclination angle is 90°; aperture is 2 mm; pumping rate is 0.17 ml/min for Solution 1; density contrast is 1111/1031.8.

It can be clearly seen that as the pumping rate of lighter fluid increased, the area of more diluted fluids increased. Smaller pumping rates of less dense fluid created a more stable environment for the heavier fluid to sink down and accumulated on the bottom of the fracture, instead of mixing with the lighter fluid. At the same time, since the flow rate of less dense fluid is

smaller than denser fluid (0.04ml/min and 0.08ml/min cases), the amount of less dense fluid flow in the fracture is smaller compared to denser fluid, which leads to mixing fluid with a higher concentration of denser fluid. Larger pumping rates of the lighter fluid increased the perturbation of the denser fluid in the fracture around the less dense fluid runlet, and by momentum exchange, mixed with them and also flowed out of the fracture. The case of 1.36ml/min pumping rate had a shorter experimental time because it ran out of fluid due to the size limit of syringe (300 ml).

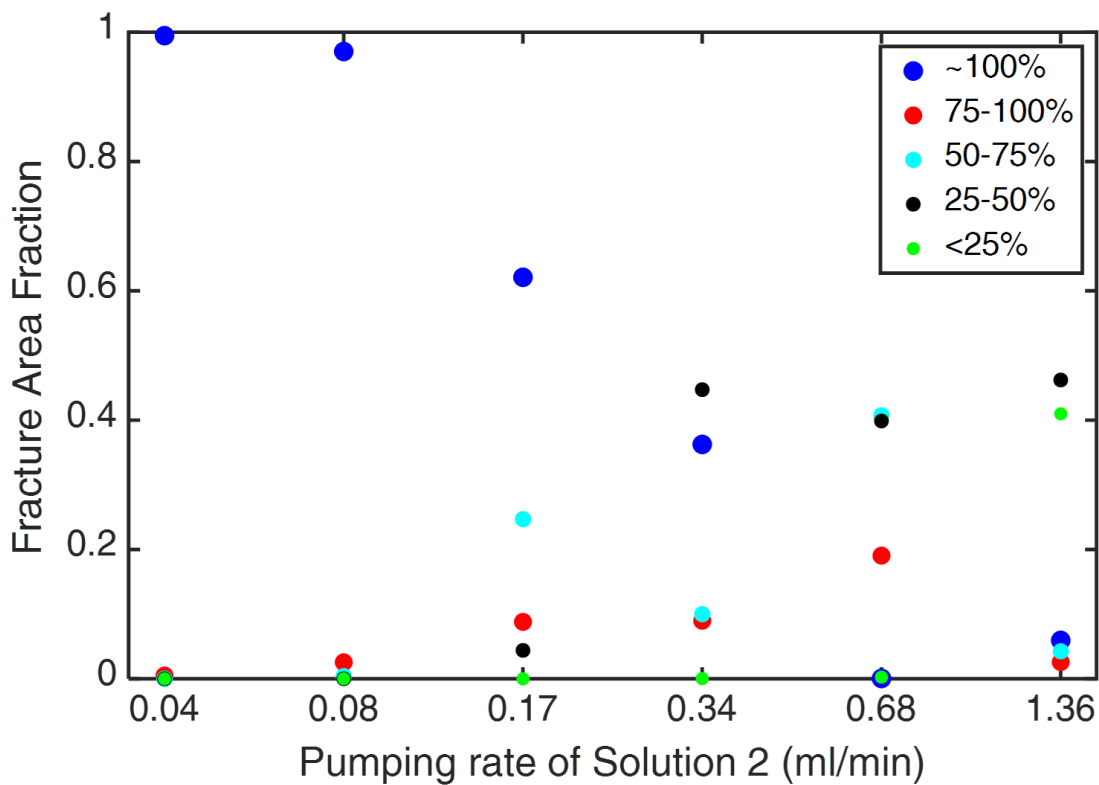


Figure 3.26 Fracture Area Fraction at T=250 minutes for different pumping rate of Solution 2. Aperture is 2 mm; pumping rate is 0.17 ml/min for Solution 1; density contrast is 1111/1031.8.

Figure 3.26 shows the fraction of different fluid concentration filling the fracture at the end of the experiments (T=250 min). The result indicates that with the increase of pumping rate, fluid mixing increases. In larger pumping rate promotes the momentum exchange between the two

fluids, therefore increases the mixing. Recall Figure 3.17 that at 1.36ml/min pumping rate, turbulence occurred, which is also a sign of increase in mixing.

In summary, inclination angles affected the shape of the light fluid runlet. With the decrease of angles of inclination, the area of the lighter fluid's runlet increased, indicating a better mixing and potential larger area of precipitation formation in a reactive fluid mixing case. The aperture affected the time each concentration fluids can exist in the fracture before finally several dominate concentration fluids covered the entire fracture. Larger aperture allowed longer existing time for different concentration fluids due to the larger space, which took longer time to replace one concentration fluid with another. Pumping rate affected the fluid mixing by changing the velocity of lighter fluid relative to heavier fluid and also by bringing more or less fluids outside of the fracture in the same period of time. At low pumping rate, higher concentration of heavier fluid dominated the fracture, while in large pumping rate, lighter fluid dominated. Density contrast affected the width of lighter fluid runlet in the non-reactive mixing by increasing the width with a larger density contrast.

## CHAPTER 4. SEISMIC RESPONSE TO CaCO<sub>3</sub> PRECIPITATION IN SYNTHETIC FRACTURES

### 4.1 Introduction

Compressional and shear waves have been shown to be sensitive to the size and spatial distributions of voids and contact area in a fracture [9]. Kendall et al. [10] used ultrasonic waves to monitor stationary and sliding surfaces, and were able to successfully distinguish the area of contact. Few studies have examined the effect of precipitates or grains in a fracture on compressional and shear wave transmission. Acosta-Colon & Pyrak-Nolte [27] performed a laboratory study of P and S waves across a synthetic uniform aperture fracture filled with glass beads. The acoustic response depended on the scale of grain relative to a wavelength  $l$ . The prime indicators of a sub porosity (i.e. layer of grain) was dispersion, interference nulls, and wave speeds for fracture-filling material that ranged from  $0.08l$  to  $2.85l$  at 1MHz. Precipitates in a fracture can fill the pores or adhere to the surface of rock, both of which can increase the contact area and reduce fracture apertures. In this study, experiments were performed to study wave propagation across fractures with precipitates induced by reactive flow. One of the goals of this study is to determine if elastic waves can detect the presence of mineral precipitates in fractures, where the precipitate size is much, much less than a  $l$  or  $\sim 0.025l$ .

### 4.2 Simulation Results

From wave propagation theory, and applying solid-solid and solid-liquid boundary conditions, simulation codes were created to simulate waves propagated across layers of different media to represent a fracture either partially or fully-filled with precipitates in a liquid. The derivation is based on reference [28] and the details are given in Appendix A. Wave velocity in a medium and the density of the medium are not independent. Simulations were performed for a

range of matrix and precipitates properties for fully and partially precipitate-filled fracture represented by a 3 layer model. Only normal incident waves were considered. The compressional, P-wave velocity is  $\alpha = \sqrt{\frac{K}{\rho}}$ , where K is the bulk modulus and  $\rho$  is the density. The bulk modulus is 2.2 GPa for water and 77 GPa for calcite [29]. The density of water is 1000 kg/m<sup>3</sup> and for calcite 2710 kg/m<sup>3</sup>. Therefore, values of K ranged from 1 GPa to 81 GPa, while the density of the fracture filling material ranged from 1000 kg/m<sup>3</sup> to 9000 kg/m<sup>3</sup>.

#### **4.2.1 Model Verification on One Solid Uniform Block with Different Properties**

The simplest case for testing the simulation is wave transmission through a solid uniform block (Figure 4.1 (a)). It was achieved by setting the properties for the 3 layers equal. A transmitted signal propagated through water from the laboratory experiments was used as the input signal in the simulation (see Figure 4.2 cyan signal). In simulation 1, the P wave velocity in the block and travel path length were held constant (4000 m/s and 10 mm) and the density of the block was varied from 1000 kg/m<sup>3</sup> to 9000 kg/m<sup>3</sup>, to explore the influence of the density of the block on the transmitted waves. Then in simulation 2, the density of the block and travel path of the acoustic waves were held constant (3000 kg/m<sup>3</sup> and 10mm), and the P wave velocity in the block was varied from 1000 m/s to 9000 m/s with an interval of 1000 m/s. Finally, the density and wave velocity were held constant (3000 kg/m<sup>3</sup> and 4000 m/s), and the travel path length was varied from 10 mm to 50 mm in length, to explore the influence of the thickness of medium on the transmitted wave. The parameters for each simulation are shown on

Table 4.1 and their corresponding maximum amplitudes of transmitted signals are shown on

Figure 4.3 Thickness' influence on transmitted signal in one-layer medium.

Table 4.2.

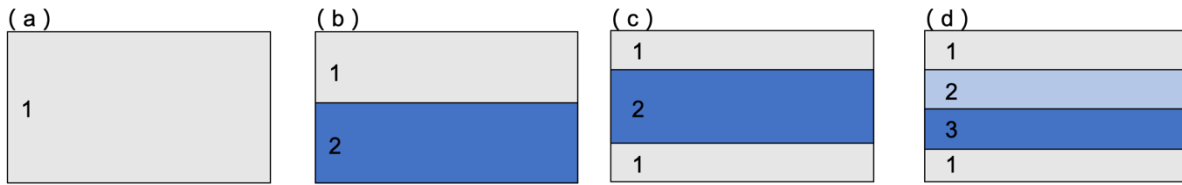


Figure 4.1 (a) One solid block model; (b) Two solid uniform blocks model; (c) Two solid uniform blocks form 3 layers model; (d) Four-layer model.

The simulation results from Figure 4.2 showed that density of the material does not affect the transmitted wave when the velocity is held constant. A decrease in arrival time occur when the P-wave velocity in material increased as expected.

Travel path length affects the arrival time and amplitude of the transmitted waves as can be seen from Figure 4.3. As expected, a longer travel length results in an increase in arrival time and a decrease in wave amplitude, and also affects the frequency components of the signal.

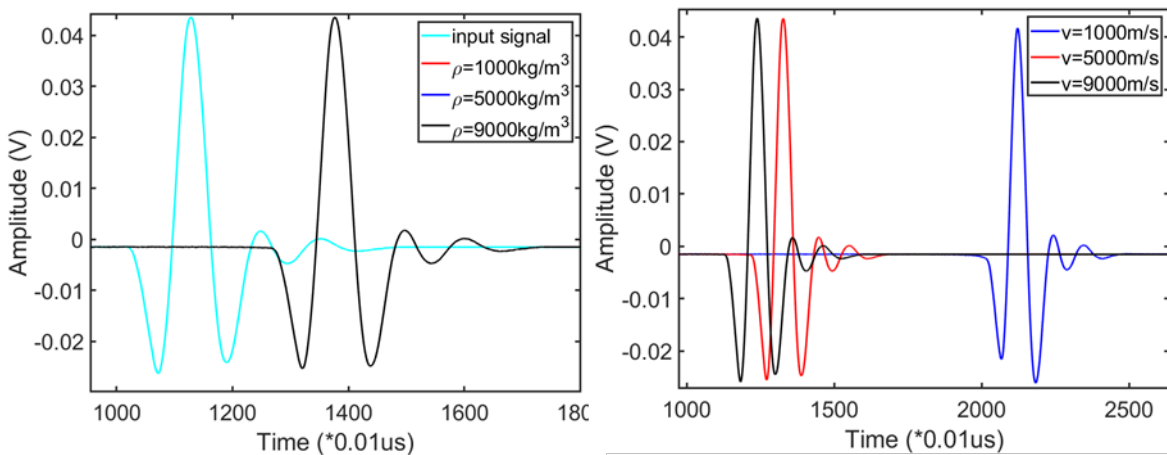


Figure 4.2 (left) Density's influence on transmitted signal in one-layer medium; (right) Acoustic velocity's influence on transmitted signal in one-layer medium.

Table 4.1 Parameters for studying influence of matrix properties.

Parameters	Simulation 1	Simulation 2	Simulation 3
<b>Velocity (m/s)</b>	4000	1000-9000, with increment of 1000	4000
<b>Density (kg/m<sup>3</sup>)</b>	1000-9000, with increment of 1000	3000	3000
<b>Thickness (mm)</b>	10	10	10 and 50

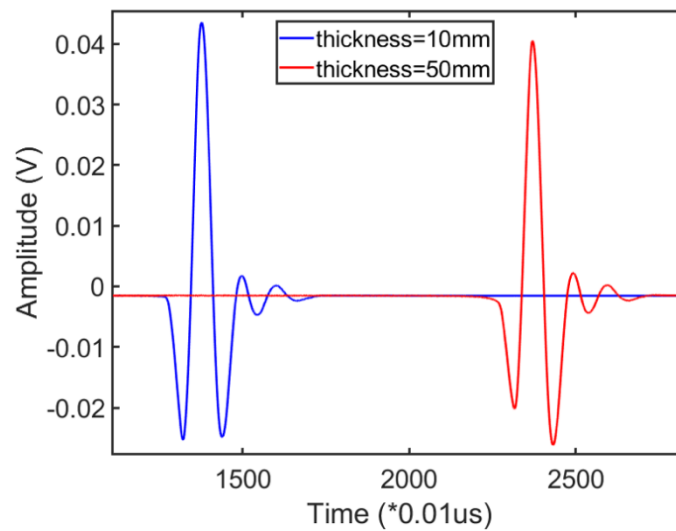


Figure 4.3 Thickness' influence on transmitted signal in one-layer medium.

Table 4.2 Transmitted signal maximum amplitude.

<b>Max Amp relative to input signal</b>							
<b>Simulation 1</b>	<b>Density: 1000 kg/m<sup>3</sup></b>	<b>Density: 5000 kg/m<sup>3</sup></b>	<b>Density: 9000 kg/m<sup>3</sup></b>	<b>Simulation 2</b>	<b>Velocity: 1000 m/s</b>	<b>Velocity: 5000 m/s</b>	<b>Velocity: 9000 m/s</b>
<b>Thickness: 10 mm</b>	99.77%	99.77%	99.77%	<b>Thickness: 10 mm</b>	95.64%	100%	100%
<b>Velocity: 4000 m/s</b>				<b>Density: 3000 kg/m<sup>3</sup></b>			
<b>Simulation 3</b>	<b>Thickness: 10 mm</b>	<b>Thickness: 50 mm</b>					
<b>Velocity: 4000 m/s</b>	100%	92.89%					
<b>Density: 3000 kg/m<sup>3</sup></b>							

#### 4.2.2 Two Solid Uniform Blocks with Different Properties

Next, two solid uniform blocks with different thickness were placed in contact to study the effects of block density and P-wave velocity of the block on the transmitted signal. The upper block is defined as block 1 and the lower block as block 2 (Figure 4.1 (b)). The total thickness of the two blocks was set to 10 mm. In the simulation, the density and velocity of the acoustic waves in block 1 and the density of block 2 were held constant (4000m/s and 3000 kg/m<sup>3</sup>), and the wave velocity in block 2 was varied from 1000 to 5000, to 9000m/s to examine the effect of wave velocity on energy partitioning. Then, simulations were also performed with the properties of block 1 and block 2 reversed. The wave velocity was fixed in block 2 to be 4000m/s, and the density of block 2 to be 1000, 5000 and 9000m/s, to explore the influence of the density. Finally, block 1 density and wave velocity were set to 3000kg/m<sup>3</sup> and 4000m/s, and its thickness was set to be 2 mm. The properties of block 2, were varied from 4000m/s, 1000kg/m<sup>3</sup> to 4000m/s, 9000kg/m<sup>3</sup> to 1000m/s, 3000kg/m<sup>3</sup> to 9000m/s, 3000kg/m<sup>3</sup>.

The simulation parameters are showed in

Table 4.3.

Table 4.3 Transmitted signal maximum amplitude.

		<b>Max Amp relative to input signal</b>						
		<b>Simulation 1</b>				<b>Simulation 2</b>		
<b>Block2</b>		<b>Velocity:4000 m/s, Thickness:5 mm</b>				<b>Density:3000 kg/m<sup>3</sup>, Thickness:5 mm</b>		
<b>Block1</b>		<b>Density: 1000 kg/m<sup>3</sup></b>	<b>Density: 3000 kg/m<sup>3</sup></b>	<b>Density: 5000 kg/m<sup>3</sup></b>	<b>Density: 9000 kg/m<sup>3</sup></b>	<b>Velocity: 1000m/s</b>	<b>Velocity: 5000m/s</b>	<b>Velocity: 9000m/s</b>
<b>Thickness: 5 mm</b>								
<b>Velocity: 4000 m/s</b>		73.85%	99.77%	93.35%	73.85%	61.70%	98.62%	84.63%
<b>Density: 3000 kg/m<sup>3</sup></b>								
		<b>Simulation 3</b>						
<b>Block2</b>		<b>Velocity:4000 m/s Thickness:8 mm</b>		<b>Density:1000 kg/m<sup>3</sup> Thickness:8 mm</b>				
<b>Block1</b>		<b>Density: 1000 kg/m<sup>3</sup></b>	<b>Density: 9000 kg/m<sup>3</sup></b>	<b>Velocity: 1000 m/s</b>	<b>Velocity: 9000 m/s</b>			
<b>Thickness: 2 mm</b>								
<b>Velocity: 4000 m/s</b>		74.08%	74.08%	60.78%	84.63%			
<b>Density: 3000 kg/m<sup>3</sup></b>								

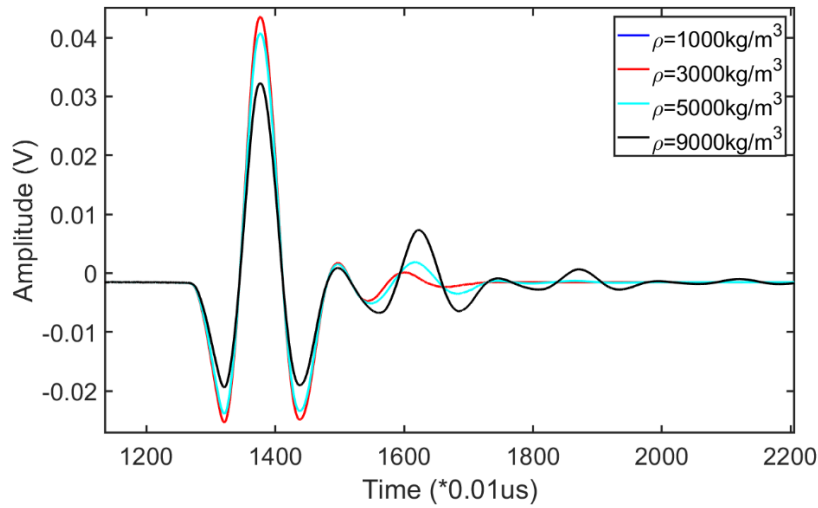


Figure 4.4 Transmitted signal as a function of density of block 2. The density of block 1 was set to  $3000 \text{ kg/m}^3$  and the wave velocity of block 1 and 2 are  $4000 \text{ m/s}$ .

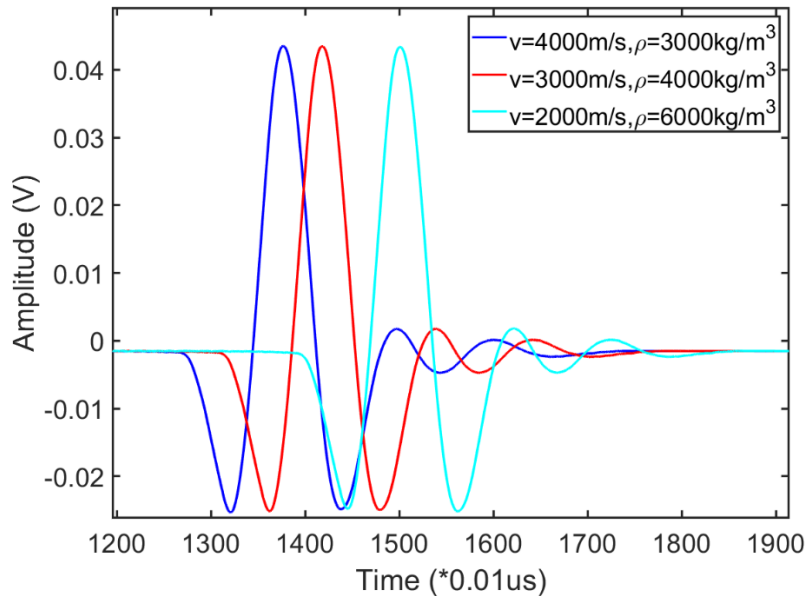


Figure 4.5 Transmitted signal as a function of properties of block 2 for impedance matching. The density of block 1 is  $3000 \text{ kg/m}^3$  and wave velocity of block 1 is  $4000 \text{ m/s}$ .

Figure 4.4 shows the transmitted signal as a function of density of block 2. As expected, the signal amplitude increased as the difference in impedance ( $\rho \cdot v$ ) decreased. Here, when block 1 and 2 have the same property, the maximum amplitude of transmitted signal is achieved. Figure 4.5 shows a signal comparison for impedance matching between block 1 and 2 using different  $v$

and  $\rho$  with the product the same. It illustrates that when the impedance matches, the maximum amplitude of transmitted signal is almost the same, regardless of the different combination of  $v$  and  $\rho$ . Arrival time of the signal differs because it is determined only by the P-wave velocity.

#### 4.2.3 Four Layer Model Representing a Mineral-Filled Fracture in a Rock Matrix

A parameter study was performed to examine the effect of the matrix material (density and wave velocity) on wave transmission across a fracture represented by a four-layer model (Figure 4.1 (d)), since in the experiments, a four-layered system, composed of poly-urethane (matrix material), liquid, precipitate, and poly-urethane can be represented by this model. The results will be used as part of this research to compare with the experimental data to aid in the understanding of the effect of precipitation on the seismic response of fractures. In the simulation, the travel path of the acoustic waves was held constant (3mm). The properties of the matrix material are listed in Table 4.4. Three different fracture apertures were used: 0.5mm, 1mm and 1.5mm. Medium 1 refers to the matrix, and medium 2 refers to liquid inside the fracture, and medium 3 refers to the precipitate in the fracture.

Table 4.4 Parameters for studying influence of matrix properties.

	<b>Matrix</b>	<b>Liquid</b>	<b>Precipitate</b>
<b>Velocity (m/s)</b>	1000-3000, with increment of 10	1480	1750
<b>Density (kg/m<sup>3</sup>)</b>	1000-2000, with increment of 10	1000	1700

The P-wave velocity and density of the precipitate and liquid in the fracture were fixed and only the P-wave velocity and density of the matrix material was changed. The fracture was assumed to be fully-filled with precipitate. The results are shown in Figure 4.6.

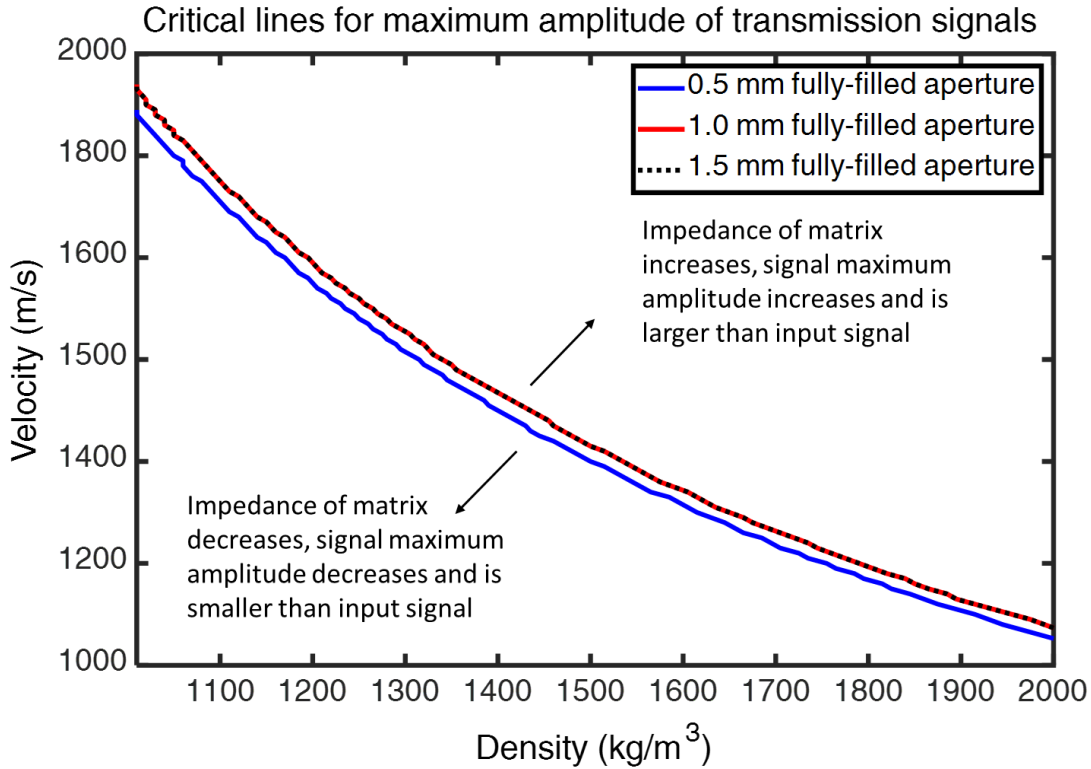


Figure 4.6 Critical lines for maximum amplitude of transmitted signals as a function of matrix material (red line overlaps the black line). The lines show the boundary between transmitted amplitude that is smaller and larger than the amplitude of the input signal.

From Figure 4.6, the upper right region represents a high impedance matrix material relative to the impedance on the curve. In this region, transmitted amplitudes will be greater than that of the incident wave. The lower left region of Figure 4.6 represents the response of a lower impedance matrix material relative to the impedance on the curve which results in a smaller maximum amplitude for the transmitted signal than incident signal. The impedance of the precipitate used in this study is  $Z(\text{precipitate})=V_{p1}*\rho_1=2.975*10^6(\text{kg/m}^2\text{s})$ . The boundary lines lie around  $Z(\text{matrix})=2.04*10^6(\text{kg/m}^2\text{s})$ , where the maximum amplitude of transmitted signal is nearly 100% of the input signal. The ratio of impedances is  $Z(\text{matrix})/Z(\text{precipitate})=0.69$  along the line. As long as  $Z(\text{matrix})/Z(\text{precipitate})>0.69$ , no matter what  $\rho$  or  $V_p$  is for the matrix, the transmitted signal will exhibit a larger amplitude than the incident wave.

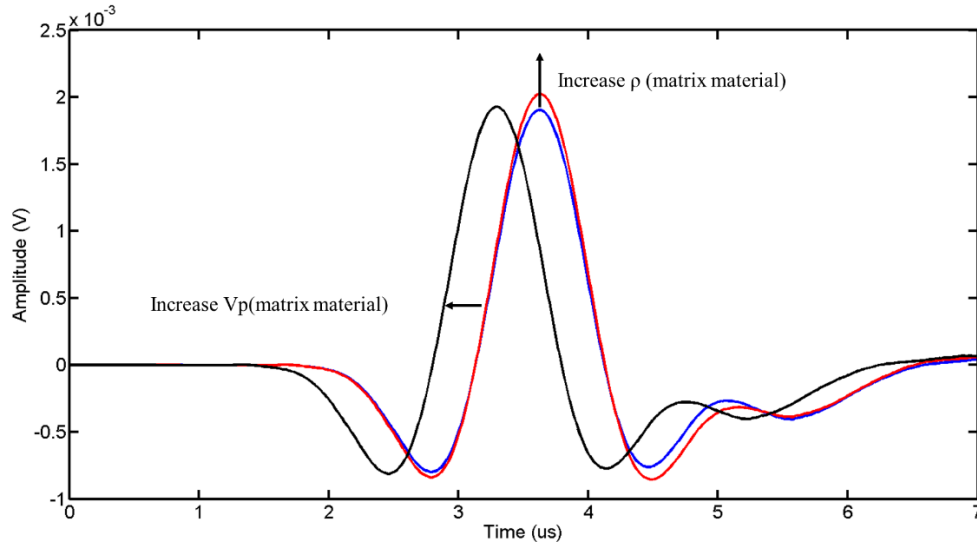


Figure 4.7 Trend of transmitted waveform change with matrix material's properties. Blue signal is for  $V_p(\text{matrix material})=1100$  m/s. Red signal is for keeping  $V_p(\text{matrix material})=1100$  m/s while increasing  $\rho(\text{matrix material})$ . Black signal is for increasing  $V_p(\text{matrix material})$  while keeping  $\rho(\text{matrix material})$  unchanged.

Figure 4.7 shows the effect of the matrix material on the transmitted wave for a fracture filled with precipitate. An increase in the  $V_p$  of the matrix material results in a decrease in travel time, and the wave will arrive earlier. It also increases the maximum amplitude of the signal, because the increase in velocity also increases the impedance, making it closer to the impedance of precipitates. In this figure, the blue curve is for  $V_p=1100$  m/s. An increase in the density of the matrix material results in a larger impedance which is closer to the impedance of precipitation, and thus generates a larger amplitude signal, which is consistent with the results in Figure 4.6.

Another 3 simulations on 0.5 mm, 1 mm and 1.5 mm aperture fractures were performed to examine the effects of thickness of precipitate on transmitted signal. The only variable is the thickness of precipitate. The properties of the matrix, liquid and precipitate are listed in Table 4.5.

Table 4.5 Parameters for studying influence of precipitate thickness.

$V_{p1}$ (m/s)	$V_{p2}$ (m/s)	$V_{p3}$ (m/s)	$\rho_1$ (kg/m <sup>3</sup> )	$\rho_2$ (kg/m <sup>3</sup> )	$\rho_3$ (kg/m <sup>3</sup> )
2200	1480	1750	1073	1000	1500

By applying the parameters above, the effects of precipitates on transmitted signals are obtained.

For a 0.5 mm aperture fracture, the maximum amplitude, first and second troughs all increase slightly with an increase in the thickness of the precipitate. Figure 4.8 shows three simulated signals when the fracture is filled with water, 0.2 mm and 0.4 mm filled with precipitate. The arrival time of the signals monotonically decreases as precipitate thickness increases. The decrease in arrival time is 0.01  $\mu$ s and 0.035  $\mu$ s for 0.2 mm and 0.4 mm of precipitate, respectively.

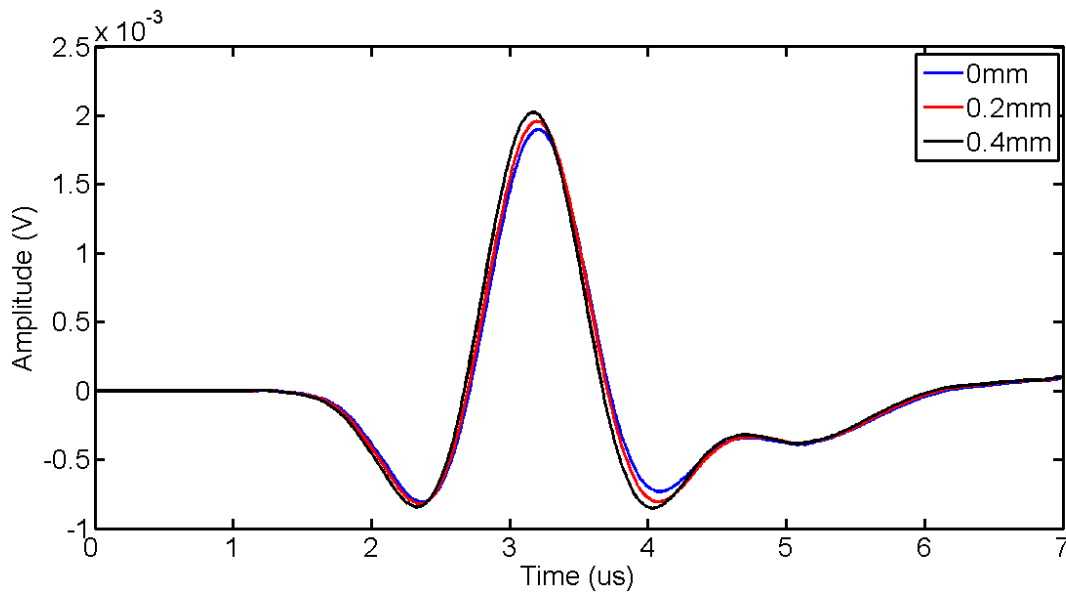


Figure 4.8 Transmitted signals for water saturated (blue), 0.2 mm thickness of precipitate filled (red) and 0.4 mm thickness of precipitate (black) in a 0.5 mm fracture.

In the 1 mm aperture fracture, a thin layer of precipitates causes a slightly decrease in amplitude for all components of the signal (see Figure 4.9 red waveform). As the precipitate continues accumulating, the signal amplitude starts to increase and eventually is larger than the signal from the saturated fracture (see Figure 4.9 black waveform). The second trough increases more than the first trough. The arrival time monotonically decreases with increasing thickness of precipitate by 0.08  $\mu\text{s}$ .

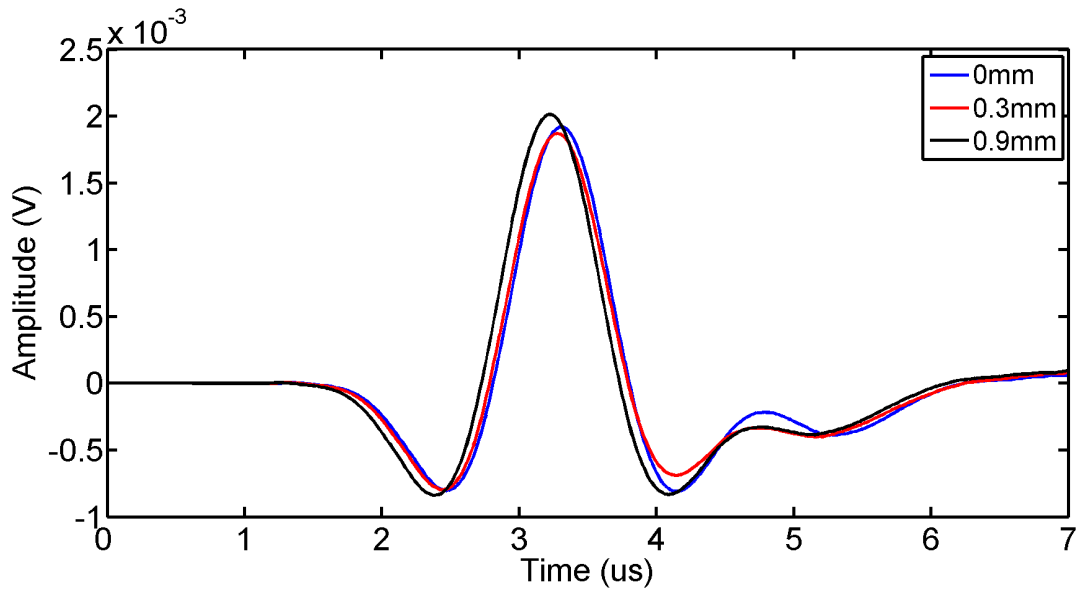


Figure 4.9 Transmitted signals for water saturated (blue), 0.3 mm thickness of precipitate filled (red) and 0.9 mm thickness of precipitate filled (black) 1 mm fracture.

In the 1.5 mm aperture fracture, initially, the amplitude of the signal decreases and then increases as precipitate thickness increases (Figure 4.10). The decrease in arrival time is greater for the 1.5 mm case than the 1.0 mm aperture fracture because the layer of precipitates is thicker than in the 1.0 mm case.

It is also noticeable that as the fracture size increases, the second trough of the initial signal (fracture filled with water) increases. In the 0.5 mm fracture case, the second trough is observed

to be shallower than the first trough; while in 1 mm and 1.5 mm fracture cases, the second trough is almost at the same amplitude as the first trough.

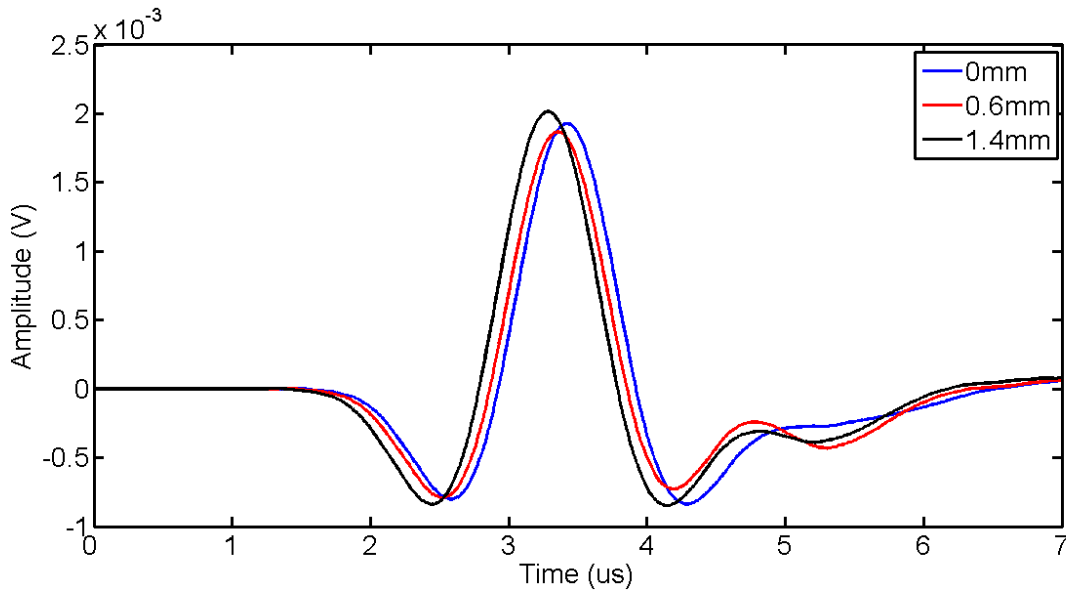


Figure 4.10 Transmitted signals for water saturated (blue), 0.6 mm thickness of precipitate filled (red) and 1.4 mm thickness of precipitate filled (black) 1.5 mm fracture.

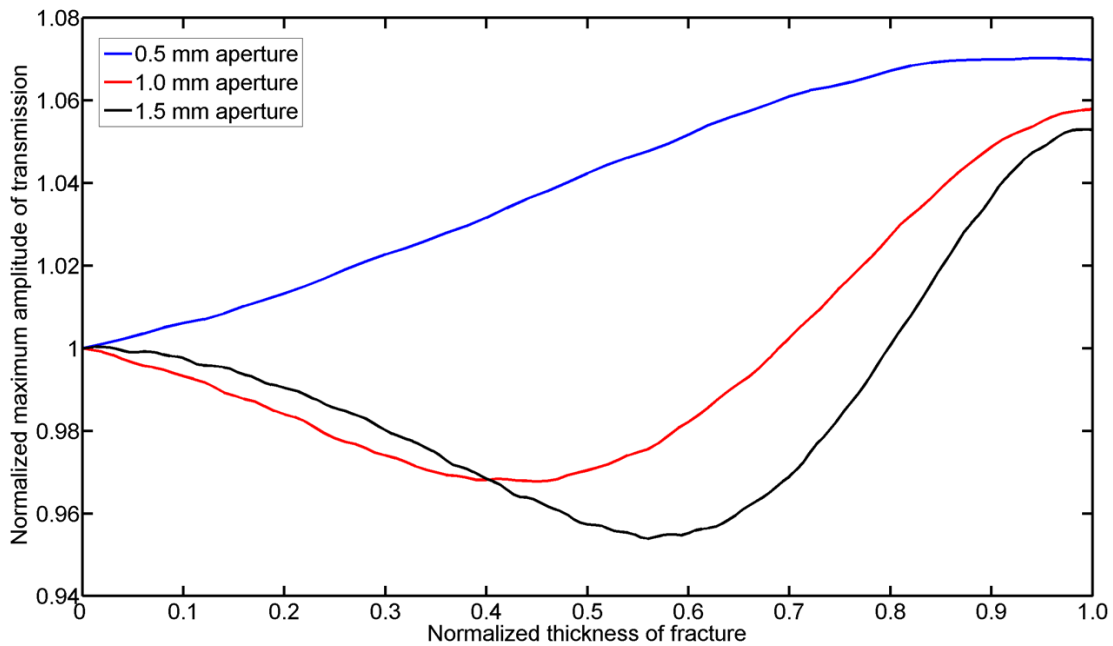


Figure 4.11 Normalized maximum amplitude of transmitted signal as a function of normalized thickness of fracture.

Figure 4.11 shows the normalized maximum amplitude of transmitted signal as a function of normalized thickness of fracture. The signals were normalized by the maximum amplitude of transmitted signal through the same aperture that filled with only water. This figure shows that the size of the aperture and the thickness of precipitates affect the transmitted signal amplitude. For example, in a 0.5 mm aperture fracture, an increase in thickness of precipitation results in a monotonic increase in the transmitted amplitude. In the 1 mm and 2 mm aperture fracture, an increase in precipitate thickness causes an initial decrease in amplitude and then an increase in transmission. Therefore, even for the same thickness of precipitation, the transmitted wave amplitude may be larger or smaller than the initial signal when the fracture is filled with a liquid. Both the aperture and the fraction of aperture filled with precipitate affect the transmitted wave amplitude. This also demonstrates that the change in amplitude is on the order of  $\pm 6\%$ .

The results from layered model provide a good tool to predict the effect of precipitate thickness on wave amplitude and arrival time.

### 4.3 Experiment results

#### 4.3.1 A Uniform Aperture Fracture Filled with CaCO<sub>3</sub> Powder and Water

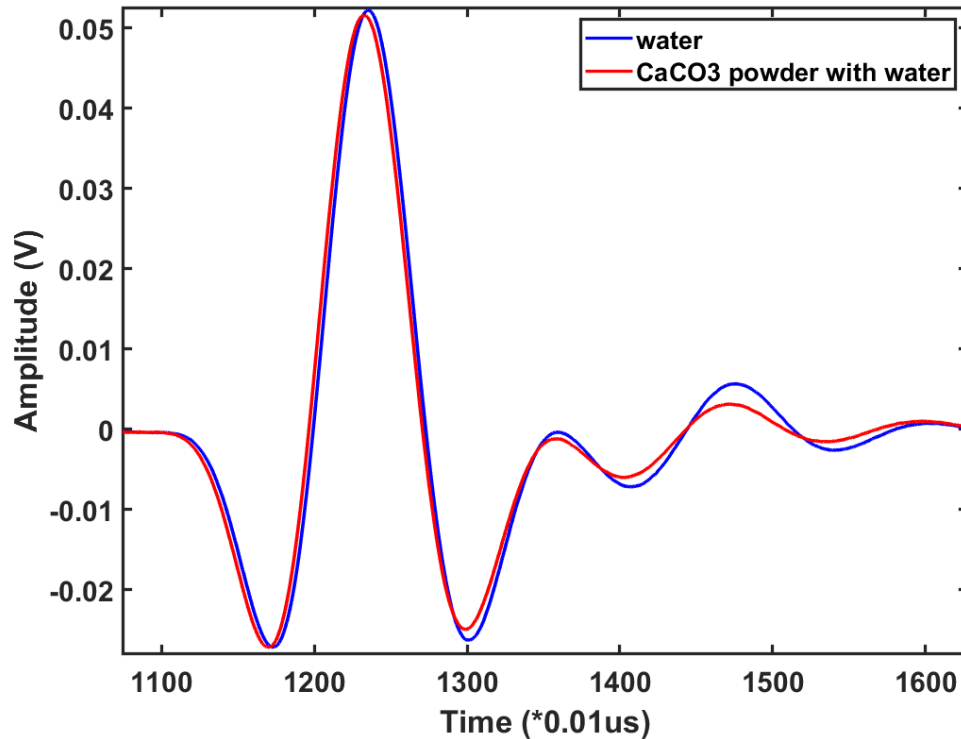


Figure 4.12 Transmitted signal through black resin-water-black resin and black resin-CaCO<sub>3</sub> powder and water mixture-black resin samples.

Figure 4.12 provides a comparison of the transmitted signals through a black resin-water-black resin and black resin-CaCO<sub>3</sub> powder and water mixture-black resin samples. The arrival time decreased slightly with CaCO<sub>3</sub> and water filling the fracture compared to the water filling fracture, which is consistent with the simulation.

#### 4.3.2 Reactive Mixing in a Uniform Aperture Fracture

Transmitted signals across a uniform aperture with reactive fluid mixing showed a slight decrease in arrival time as the experimental time increased (Figure 4.14). Simulation results with ~0.2 mm precipitates layer in a 4 mm aperture exhibited a similar behavior. The presence of precipitates on transmitted waves is more evident in the second arrival around 21  $\mu$ s in the

experimental data (see Figure 4.13 (b)). The second arrival is the transmitted wave with one reflection in the fracture (Figure 4.13 (b)). From the X-ray CT scan, the thickness of the precipitate is  $\sim 0.6$  mm (see Figure 4.15 ). The difference between the simulation and experiment is due to the fact that the precipitate is not uniformly solid material; the precipitate particles may not be in contact or compact, resulting in different properties that would affect the wave velocity.

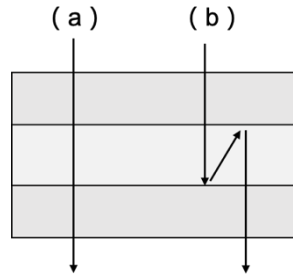


Figure 4.13 Sketch of (a) direct wave transmission through layers of media; (b) transmission wave with once reflection on the fracture

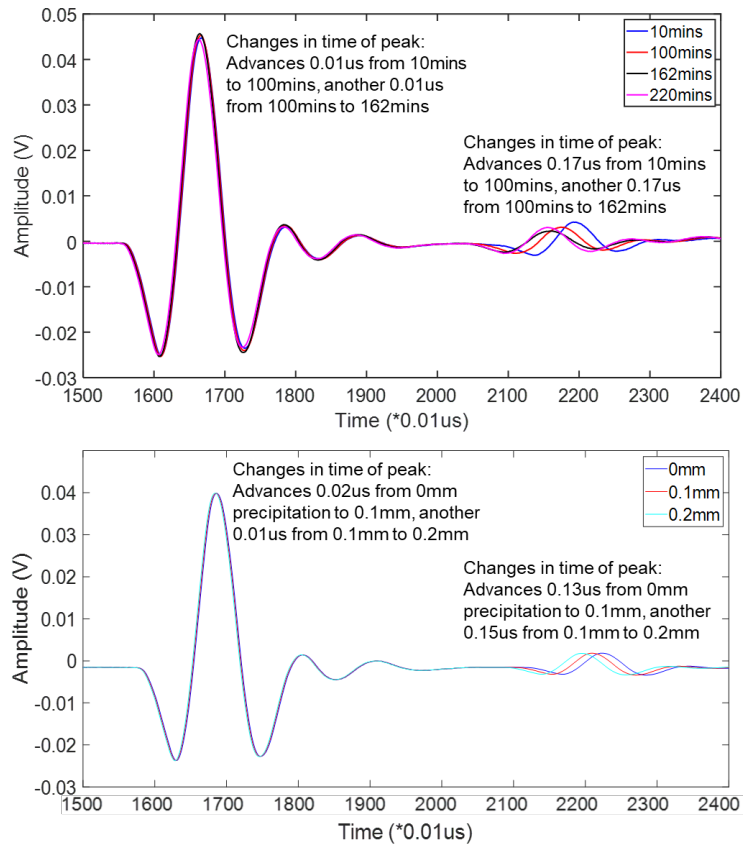


Figure 4.14 Comparison between experimental signal and simulated signal.

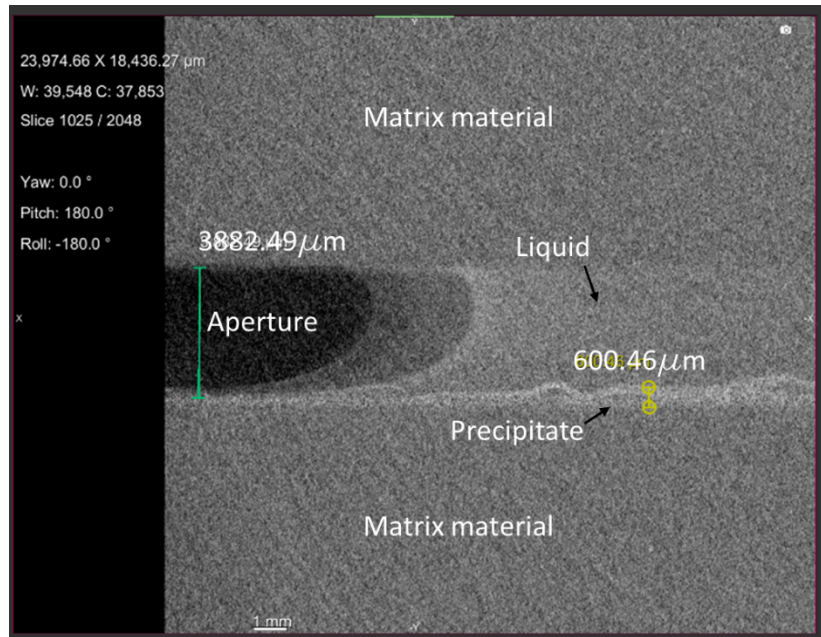


Figure 4.15 X-ray CT scan of mineral precipitation formed in the uniform aperture fracture.

### 4.3.3 Pore-filling Precipitation in a Variable Aperture Fracture

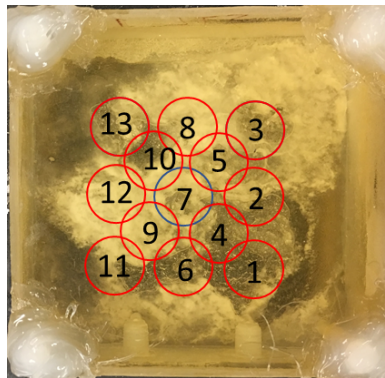


Figure 4.16 Transducer layout.

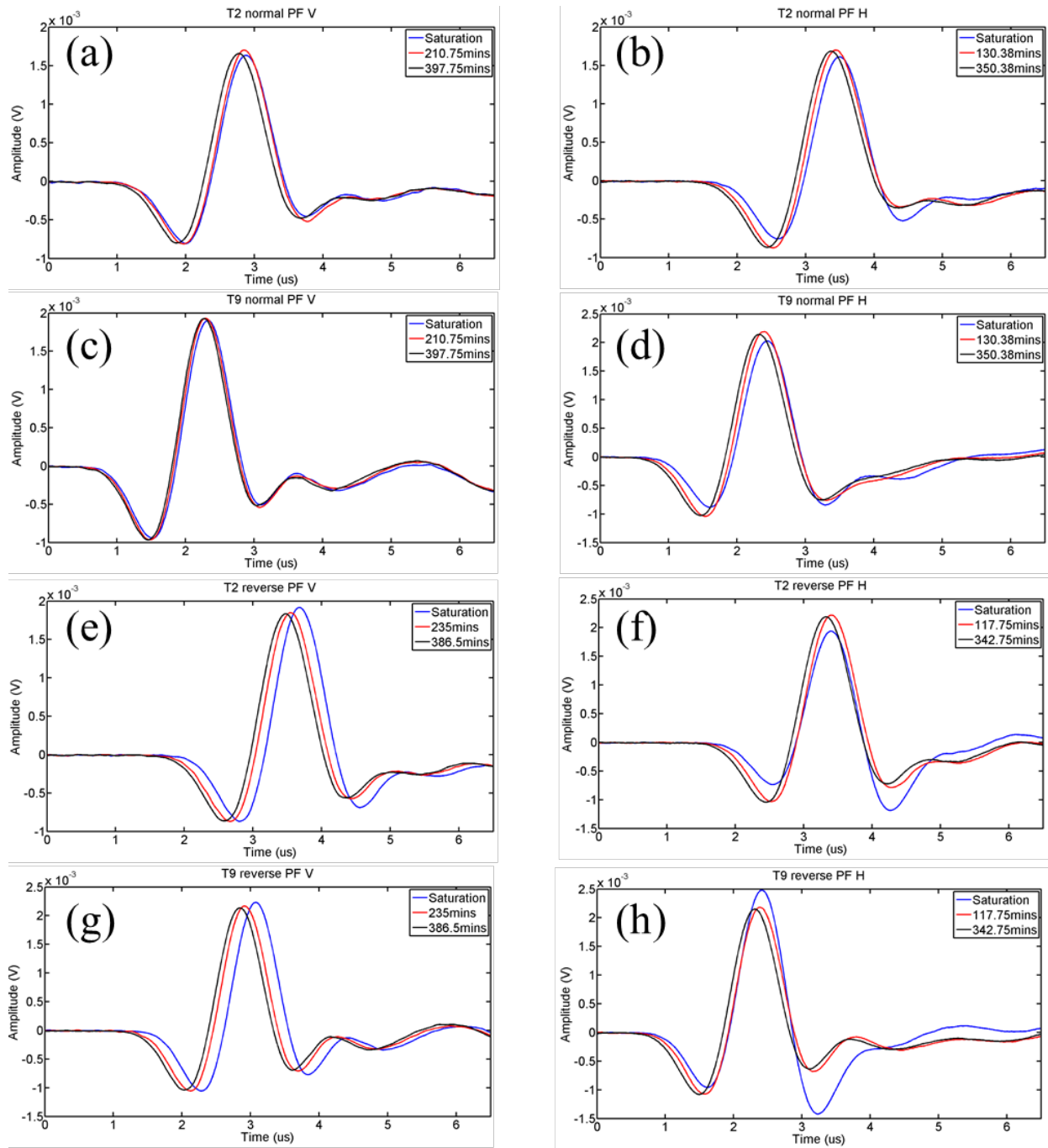


Figure 4.17 Individual signals during the saturation period (blue), reaction period (red) and the end of the experiment (black) of the pore-filling precipitation for transducer 2 and 9 in normal order (a) (c) vertical and (b) (d) horizontal fracture, and pore-filling precipitation for transducer 2 and 9 in reverse order (e) (g) vertical and (f) (h) horizontal fracture, respectively.

Figure 4.17 (a) and (c) show the signals recorded during the saturation period, the reaction period (210.75mins) and at the end of an experiment (397.75mins) for the normal order pore-filling precipitation in a vertical fracture (see 2.1.1 for description of experiments). Figure 4.17 (b) and (d) contain the same information but for the horizontal fracture. By comparing the signals, in both cases, the arrival time decreases, but the signals from horizontal pore-filling precipitation case decrease more (0.13-0.21 $\mu$ s) than signals from the vertical fracture. This is ascribed to thicker precipitation in the horizontal fracture (see Figure 3.1 (c)), which would have a longer travel path through the precipitates than water. The horizontal pore-filling precipitation also change the trend of the first and second troughs. The first trough increased in amplitude while the second decreased, indicating phase interference.

Figure 4.17 (e) and (g) show the signals recorded during the saturation period, the reaction period and the end of the experiment for the reverse order pore-filling precipitation in the vertical fracture. Figure 4.17 (f) and (h) shows signals from the horizontal fracture. By comparing the signals, it can be seen that in the vertical pore-filling experiment, the signal arrival time decreases (0.16 $\mu$ s). While in the horizontal pore-filling experiment, the arrival time decreased (0.13 $\mu$ s) and the 2 troughs change trend: first trough increased while second decreased in amplitude. The decrease in transmitted amplitude might be because of the thickness of precipitate. Recall the maximum transmitted amplitude in Figure 4.11, when the thickness of precipitate is small, the transmitted amplitude will be smaller than that during saturation period.

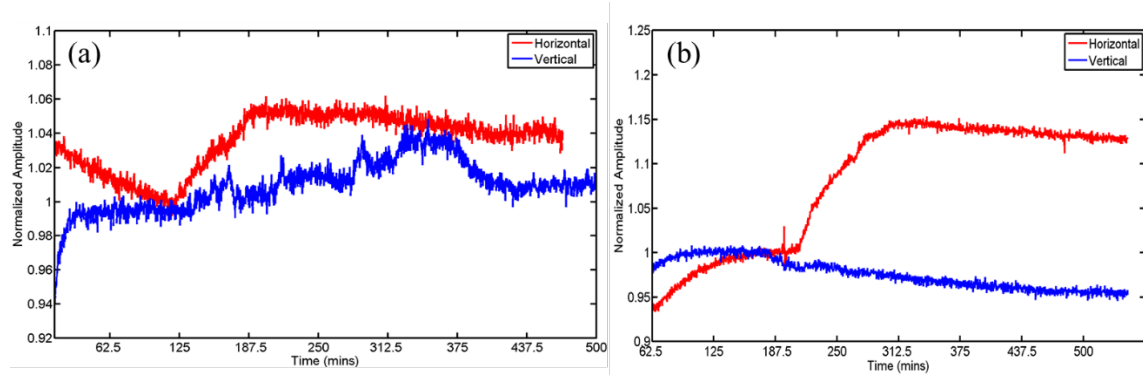


Figure 4.18 Maximum amplitude of transmitted signals as a function of time for transducer 2 for (a) normal order pore-filling precipitation and (b) reverse order pore-filling precipitation.

Figure 4.18 shows the maximum amplitude of transmitted signals as a function of time for transducer 2 for both normal order and reverse order pore-filling precipitation. The amplitude is normalized to the one from before the initiation of pumping of both solutions. In both cases, the amplitude from the signal for the horizontal fracture increases more than for the vertical fracture which is attributed to the good mixing of two reactive flow and thicker precipitate.

### 4.3.4 Surface adhering Precipitation in a Variable Aperture Fracture

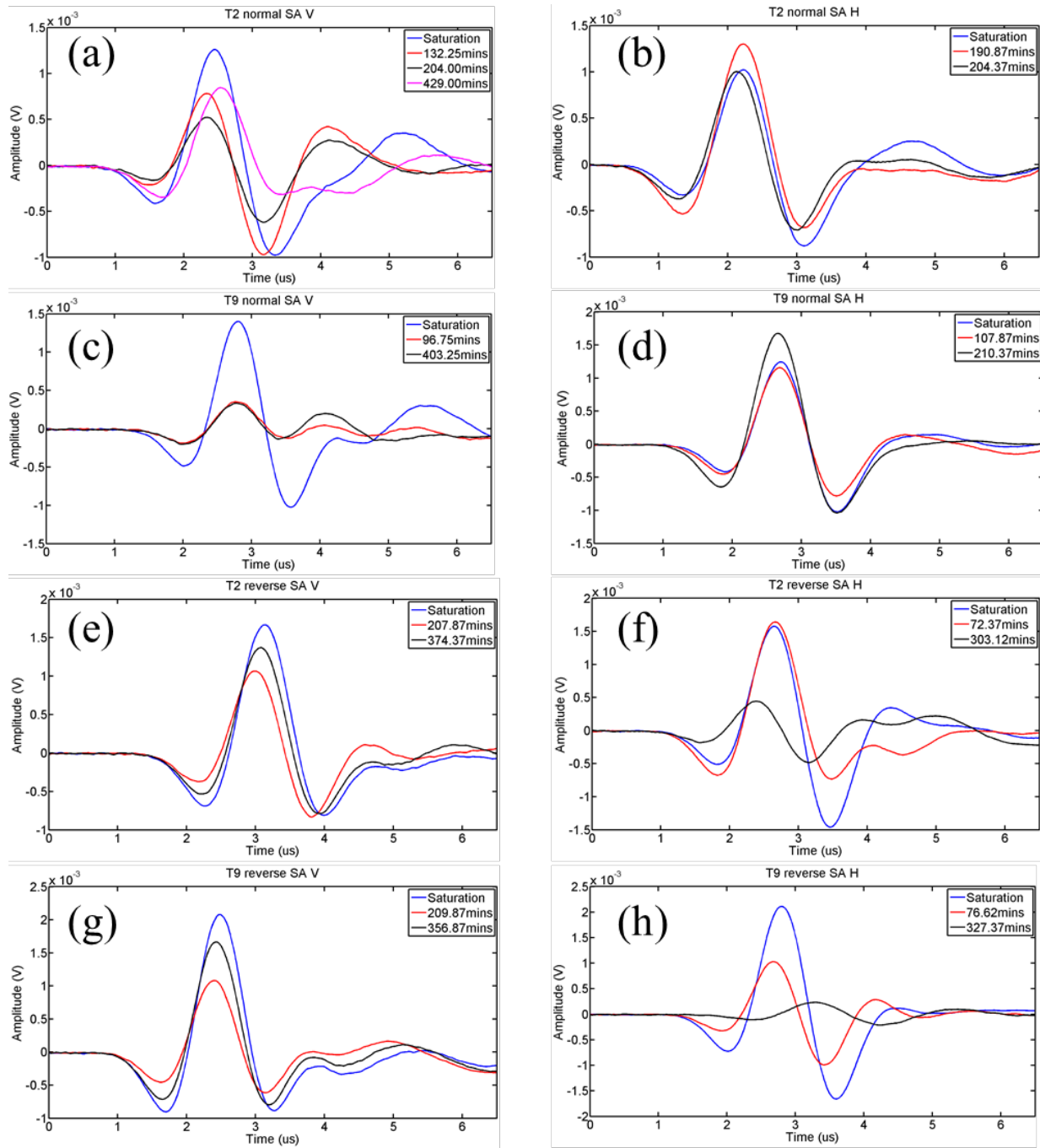


Figure 4.19 Individual signals during the saturation period (blue), reaction period (red) and the end of the experiment (black; pink in(a)) of the normal order surface adhering precipitation for transducer 2 and 9 in (a) (c) vertical and (b) (d) horizontal fracture, respectively.

Figure 4.19 (a) and (c) show the signals recorded during the saturation period, reaction period and the end of the experiment of the normal order surface adhering precipitation in the vertical fracture. Figure 4.19 (b) and (d) show the same signals from the horizontal fracture. In the horizontal fracture experiment, the signal arrival time decreases much more ( $0.11 \mu\text{s}$ ) than in the vertical fracture experiment ( $0.02 \mu\text{s}$ ). The difference between the 1st and 2nd trough is smaller after precipitation in horizontal fracture experiment (a decrease of 39%). Figure 4.20 shows the signal frequency component change corresponding to Figure 4.19 (a) and (b). Figure 4.20 (a) shows that all frequency components decreased but the signal at 132.25 minutes and 204 minutes lost more frequency component  $<0.5\text{MHz}$ . The signal at 429 minutes recovered some frequency component  $<0.5\text{MHz}$  compared to the signal at 204 minutes. Figure 4.20 (b) shows that all frequency component of horizontal fracture first increased at 190.87 minutes and then decreased at 204.37 minutes.

Figure 4.19 (e) and (g) show the signals recorded during the saturation period, reaction period and the end of the experiment of the reverse order surface adhering precipitation in the vertical fracture. Figure 4.19 (f) and (h) show the signals from the horizontal fracture. In the vertical fracture experiment, the arrival time also increases ( $0.05 \mu\text{s}$ ). As for the horizontal fracture experiment, the signal arrival time decreases and the pattern of the two troughs also changes: the difference becomes smaller. The amplitude decrease is due to gas bubbles because the arrival time does not change. The random generation of gas bubbles results in different interference on transmission.

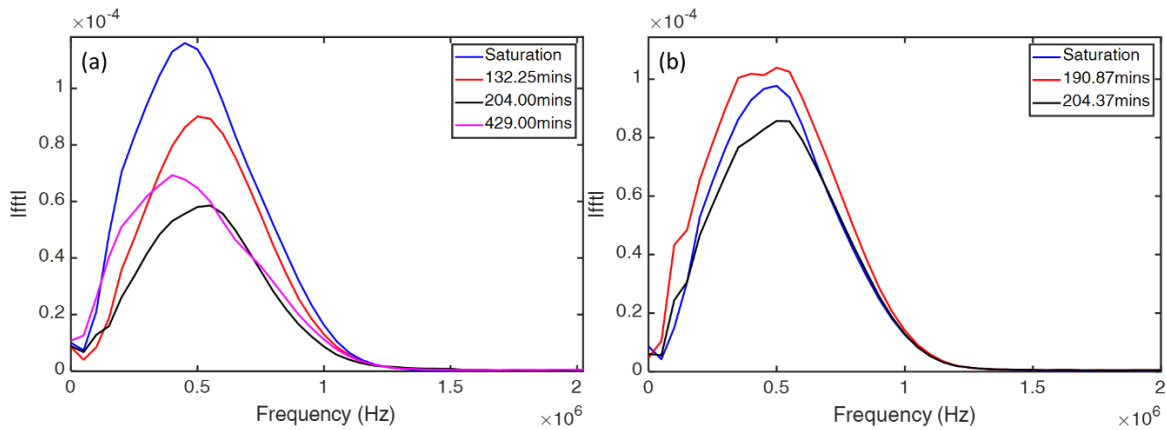


Figure 4.20 FFT of the signals at normal order surface-adhering experiment for transducer 2. The frequency components are corresponding to Figure 4.19 (a).

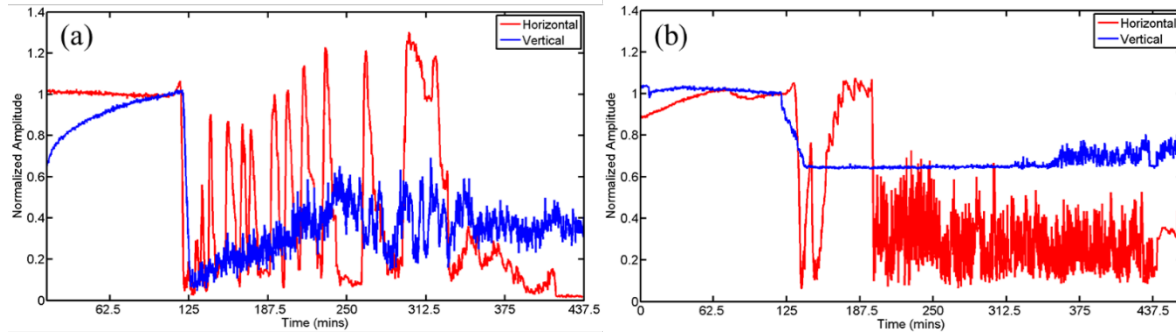


Figure 4.21 Maximum amplitude of transmission signals as a function of time for transducer 2 for (a) normal order surface adhering precipitation and (b) reverse order surface adhering precipitation.

Figure 4.21 shows the maximum amplitude of transmission signals as a function of time for transducer 2 for both normal order and reverse order surface adhering precipitation. The amplitude is normalized by the amplitude from before the pumping of both solutions into the fracture. The amplitude in horizontal fracture experiment increases more than in the vertical fracture (see the peaks of red signals) in both normal order and reverse order cases. The huge fluctuations are caused by  $\text{CO}_2$  gas generation during the reaction.

In summary, for pore-filling precipitation, without the interference of  $\text{CO}_2$  gas bubbles, changes in the arrival time can be used to determine the thickness of precipitates in a fracture, and

the aperture of fracture can be speculated from the transmitted amplitude change by referring to the maximum amplitude curve as shown in Figure 4.11 (given the information of the properties of the fluids and precipitates). For surface-adhering precipitation, if CO<sub>2</sub> gas bubble generation is fierce, transmitted signals would be interrupted by the gas bubbles. The fact that the precipitate adheres to the fracture surface and may change the impedance of the fracture cannot be interpreted the signal.

## CHAPTER 5. CONCLUSION AND FUTRUE WORK

In this dissertation, the mixing of two non-reactive or reactive fluids inside a fracture was studied. Influential factors like density contrast between the fluids, pumping rate, angles of inclination, and fracture aperture were varied to examine the contribution from each factor on spatial distribution of concentration of mixed fluids and precipitates.

From the studies with non-reactive and reactive fluids, a density contrast between two fluids causes the lighter fluid to be confined to a narrow path, a runlet, by the denser fluid and also leads to stratification in fluid concentrations under the influence of gravity. The width and shape of the runlet is affected by the fracture inclination angles. A minimum runlet width occurs at a 90° inclination angle (vertical fracture), while a 0° inclination angle (horizontal fracture leads to complete mixing across the entire fracture plane. The formation of a runlet that increases in width with decreasing fracture inclination angle affects the distribution of precipitates that form from the mixing of two fluids. The distribution of precipitates is controlled by the density contrast between the two fluids and the fracture inclination angle. For fracture inclinations  $\leq 30^\circ$ , precipitate formation and sedimentation occurred across the entire fracture plane. For  $30^\circ < \text{angles} < 90^\circ$ , precipitate distribution initially occurred across the entire fracture plane but the coefficient of friction between the precipitates and fracture plane was not big enough such that the precipitates “rained down” to the bottom of the fracture, and any additional formation of precipitates was limited to the runlet. At 90°, the only formation of precipitates occurred along the runlet. These results suggest that trying to seal fractures in-situ must account for fracture orientation and the density contrast between the fluids. Horizontal fractures were observed to be easier to seal than

vertical fractures because complete mixing can occur in horizontal fractures where the less dense fluid rides on top of the high density fluid.

The aperture and pumping rate of fluids affected the residence time of each fluids in the fracture. Large apertures and low pumping rates resulted in relatively longer residence time which resulted in the formation of more precipitates. For small aperture fractures, precipitates can block the mixing lines even in a horizontal fracture, leading to poor sealing. This finding suggests that when using a low pumping rate, the sealing of a large aperture fracture would be more probable than a smaller aperture fracture.

The spatial distribution of the two fluids, instead of the fracture roughness, was found to dominate the mixing of two fluids with different densities. The spatial distribution for the majority of precipitation formation and the transport of precipitates can accordingly be predicted by the properties of the two reactive fluids. For example, when two reactive fluids mix in a vertical fracture, the majority precipitation will form near and along the path of lighter fluid (i.e. the runlet) because of confinement of the lighter fluid by the denser fluid to a narrow runlet. The location of the runlet can be controlled by tuning the density contrast between the two fluids. Finally, while the major focus of this study was on pore-filling (homogeneous) precipitation, the observations were found to apply to location of surface adhering (heterogeneous) precipitation in fractures with inclination angles of  $0^\circ$  and  $90^\circ$ . However, the main difference is that surface adhering precipitates are less likely to result in particle transport through sedimentation or fluid transport.

Future work on fluid mixing fractures should include the use of natural fractures or induced fractures in rock. In this study, chemical reactions with sample matrix were eliminated to focus on the behavior of mixing in uniform aperture fractures. Rocks that are common in CO<sub>2</sub> storage sites would be a natural place to start as one trapping mechanisms is forming minerals that “lock” in

the CO<sub>2</sub>. Another area for future work is the development of computational models that can simulate density contrasts, precipitate formation and particle transports. The complexity of coupling miscible reactive fluids mixing and particle transport in a 3D model generates various difficulties such as the requirements for multidisciplinary knowledge, disparate time-steps to capture chemical reactions versus particle transport, and how to reduce the computational expense.

## APPENDIX A. WAVE PROPAGATION THEORY

### A.1 Wave Propagation in Elastic Material

Mineral precipitates in a fracture can lead to layers with higher density than the surrounding material, i.e. a condition that cannot be analyzed by the displacement discontinuity theory for wave propagated across a fractures [30-32]. In this section, a layered approach is used to model a precipitate filled or partially-filled fracture.

By solving the wave equation in an elastic material

$$\rho \frac{\partial^2 \vec{u}}{\partial t^2} = (\lambda + \mu) \nabla(\nabla \cdot \vec{u}) + \mu \nabla^2 \vec{u}. \quad \text{Equation A-1}$$

two kinds of waves solutions are obtained. The first solution is for a longitudinal wave, usually referred to as a P wave or compressional, or longitudinal wave that exhibits displacement in the same direction as wave propagation or k vector. The wave velocity is

$$\alpha = \sqrt{\frac{\lambda + 2\mu}{\rho}}, \quad \text{Equation A-2}$$

where  $\rho$  is the mass density,  $\lambda$  and  $\mu$  are Lamé's constants ( $\mu$  is shear modulus).

The second body wave is the shear or transverse wave, usually referred to as an S wave. The S wave displacement is perpendicular to the direction of wave propagation. The S wave can be categorized as SH wave (polarization direction is perpendicular to the plane formed by the propagation direction and the normal to the interface) and SV wave (polarization is in the plane formed by the propagation direction and the normal to the interface). The velocity of the S wave is given by

$$\beta = \sqrt{\frac{\mu}{\rho}}. \quad \text{Equation A-3}$$

### A.1.1 Boundary Conditions

To understand the wave propagation across different materials, boundary conditions are indispensable. The simplest boundary conditions includes welded (solid-solid, solid-fluid), non-welded and free surfaces. These boundary conditions are described in the following sections.

#### *Welded Boundaries*

A weld interface is described by boundary conditions that require continuity in particle displacements and stresses. At an interface ( $z=0$ ):



Figure 5.1 Sketch of the boundary.

$$[u_x] = [u_y] = [u_z] = 0, \quad \text{Equation A-4}$$

$$[\sigma_{zx}] = [\sigma_{zy}] = [\sigma_{zz}] = 0, \quad \text{Equation A-5}$$

where  $u$  is the displacement, and  $\sigma$  is the stress. The brackets represent the difference in the displacements or stresses above and below the interface [33].

The stress can be expressed in terms of displacement:

$$[\sigma_{zx}] = \mu \left( \frac{\partial u_x}{\partial z} + \frac{\partial u_z}{\partial x} \right), \quad \text{Equation A-6}$$

$$[\sigma_{zy}] = \mu \frac{\partial u_y}{\partial z}, \quad \text{Equation A-7}$$

$$[\sigma_{zz}] = \lambda \left( \frac{\partial u_x}{\partial x} + \frac{\partial u_z}{\partial z} \right) + 2\mu \frac{\partial u_z}{\partial z}. \quad \text{Equation A-8}$$

### ***Solid-Fluid Boundaries***

For solid-fluid interfaces, such as rock-water, the boundary conditions are similar to welded case, except no lateral slip is allowed along the boundary. Thus, the only component of displacement is normal to the boundary and is continuous. Stresses are also still continuous.

$$[u \cdot n] = 0, \quad \text{Equation A-9}$$

$$[\sigma_{xx}] = [\sigma_{yy}] = [\sigma_{zz}] = 0, \quad \text{Equation A-10}$$

where  $n$  is the unit vector perpendicular to the interface [33].

### ***Free Surface***

For free surface boundary conditions, the tractions on the boundary are taken to be zero. There is no restriction on displacements [33].

$$\sigma_{ij} \cdot n_j = 0. \quad \text{Equation A-11}$$

### ***Non-Welded Boundaries***

Non-welded boundaries, also known as displacement discontinuity boundary conditions, have been used to represent a fracture with different rheological responses, such as a spring, a dashpot, a Kelvin material with a spring and dashpot in parallel, or a Maxwell material with a spring and dashpot in series [30-32]. The displacements across the interface are discontinuous, but the stresses are continuous.

$$[u_x] = \mathcal{S}_x \sigma_{xx}, \quad \text{Equation A-12}$$

$$[u_z] = \mathcal{S}_z \sigma_{zz}, \quad \text{Equation A-13}$$

$$[\sigma_{xx}] = [\sigma_{yy}] = [\sigma_{zz}] = 0. \quad \text{Equation A-14}$$

Fractures in the subsurface are highly variable in terms of being open, closed, partially filled by minerals or fluids. The different filling of a fractures results in different boundary conditions for wave propagation across a fracture. For example, when the fracture is filled with mineral

precipitation, it may be treated as a welded boundary. If the fracture is filled with liquid, then it can be treated as a Kelvin interface. But, the non-welded condition is not appropriate when a fracture is filled with a high density material, higher than the matrix density.

In this thesis, a multilayer model is used with solid-solid and solid fluid interfaces to perform a parameter study on the effect of precipitate thickness and properties on compressional wave propagation.

## A.2 Reflection and Transmission of Plane Waves on Different Interface

In the next section, the derivation of the scattering matrix is given for reference. This is based on the work found in [28]. This scattering matrix depends on partitioning of energy into P and S waves.

### A.2.1 SH Wave Incident on a Welded Interface

First, consider the scattering of a plane SH wave at the interface between two solid half-spaces. Figure A.1 shows all the possible reflected and transmitted waves with labels for their coefficients.

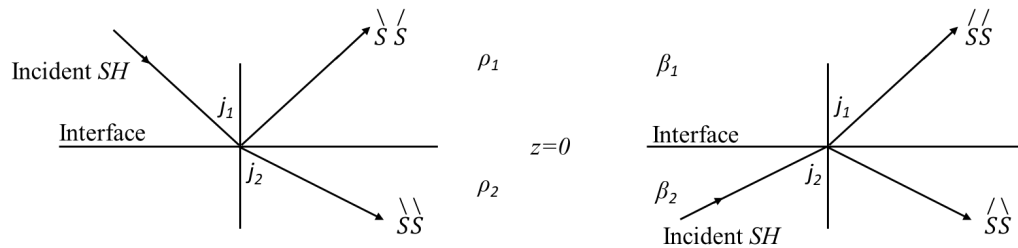


Figure A.1. Notation for the four possible reflection/transmission coefficients for incident SH-wave (redraw from [28]).

In Figure A.2, the x and z directions are tangential to the interface and y is normal to the surface. The upper half-space is denoted as 1 with  $z < 0$  and the lower half-space is denoted as 2

with  $z > 0$ . Stress components  $zx$  and  $zz$  are not excited by any of the incident/reflected/transmitted  $SH$  displacements, such that the only nontrivial dynamic boundary condition is continuity of stress of  $yz$  across  $z = 0$ . The  $y$ -component of displacement is also continuous, and the elements of the scattering matrix are

$$\begin{pmatrix} \overset{\backslash}{S} \overset{/}{S} & \overset{/}{S} \overset{/}{S} \\ \overset{\backslash}{S} \overset{\backslash}{S} & \overset{/}{S} \overset{\backslash}{S} \end{pmatrix}, \quad \text{Equation A- 15}$$

$$\overset{\backslash}{S} \overset{/}{S} = \frac{\rho_1 \beta_1 \cos j_1 - \rho_2 \beta_2 \cos j_2}{\Delta},$$

$$\overset{/}{S} \overset{/}{S} = \frac{2\rho_2 \beta_2 \cos j_2}{\Delta},$$

$$\overset{\backslash}{S} \overset{\backslash}{S} = \frac{2\rho_1 \beta_1 \cos j_1}{\Delta},$$

$$\overset{/}{S} \overset{\backslash}{S} = -\overset{\backslash}{S} \overset{/}{S},$$

$$\Delta = \rho_1 \beta_1 \cos j_1 + \rho_2 \beta_2 \cos j_2, \quad \text{Equation A-16}$$

This scattering matrix contains reflection and transmission coefficients of a  $SH$  wave incident from above and below the interface.  $S$  in symbol  $\overset{\backslash}{S} \overset{/}{S}$  indicates that the wave is a shear wave and the superscript represents the direction of propagation. The first  $S$  represents the incident  $S$  wave and the second  $S$  represents the reflected or transmitted  $S$  wave. For example,  $\overset{\backslash}{S}_1 \overset{/}{S}_2$  stands for the reflection coefficient of a shear wave impinging onto an interface from the upper half-space, and  $\overset{\backslash}{S}_1 \overset{\backslash}{S}_2$  stands for the transmission coefficient of a shear wave impinging onto an interface from the upper half-space and transmitted into the lower half-space.  $\rho$ ,  $\beta$ ,  $j$  are the density, shear wave

velocity and the angle between the shear wave propagation direction and the normal to the interface. Subscripts 1 and 2 define the half-space in which these parameters are used. The parameter  $p$  which appears in Table A.1 is the slowness in  $x$  direction [28].

Table A.1 Displacement for incident and scattered waves [28].

Incident Wave		Scattered Wave	
Type	Displacement	Type	Displacement
<b>Downgoing SH</b>	$(0, S, 0) \exp[i\omega(px + \frac{\cos j_1}{\beta_1} z - t)]$	<b>Upgoing SH</b>	$(0, S, 0) S S \exp[i\omega(px - \frac{\cos j_1}{\beta_1} z - t)]$
		<b>Downgoing SH</b>	$(0, S, 0) S S \exp[i\omega(px + \frac{\cos j_2}{\beta_2} z - t)]$
<b>Upgoing SH</b>	$(0, S, 0) \exp[i\omega(px - \frac{\cos j_2}{\beta_2} z - t)]$	<b>Upgoing SH</b>	$(0, S, 0) S S \exp[i\omega(px - \frac{\cos j_1}{\beta_1} z - t)]$
		<b>Downgoing SH</b>	$(0, S, 0) S S \exp[i\omega(px + \frac{\cos j_2}{\beta_2} z - t)]$

### A.2.2 SH Wave Incident on a Solid-Fluid Interface

Fluids do not support shear stress, while shear waves are not transmitted across a solid-fluid interface, reflected waves are generated.

### A.2.3 P-SV Wave Incident on a Welded Interface

The scattering of a P-SV wave at a welded interface is described by the following scattering matrix

$$\begin{pmatrix} \overset{\backslash}{P}\overset{/}{P} & \overset{\backslash}{S}\overset{/}{P} & \overset{\backslash}{P}\overset{\backslash}{P} & \overset{\backslash}{S}\overset{\backslash}{P} \\ \overset{\backslash}{P}\overset{/}{S} & \overset{\backslash}{S}\overset{/}{S} & \overset{\backslash}{P}\overset{/}{S} & \overset{\backslash}{S}\overset{/}{S} \\ \overset{\backslash}{P}\overset{\backslash}{P} & \overset{\backslash}{S}\overset{\backslash}{P} & \overset{\backslash}{P}\overset{\backslash}{P} & \overset{\backslash}{S}\overset{\backslash}{P} \\ \overset{\backslash}{P}\overset{\backslash}{S} & \overset{\backslash}{S}\overset{\backslash}{S} & \overset{\backslash}{P}\overset{\backslash}{S} & \overset{\backslash}{S}\overset{\backslash}{S} \end{pmatrix}, \quad \text{Equation A-17}$$

Notations of the sixteen reflections and transmission elements are shown in Figure A.2 and given below:

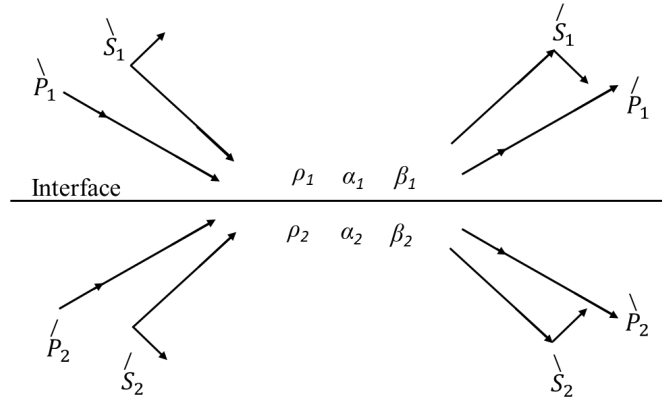


Figure A.2 The complete system of incident and scattered plane P-SV waves, in terms of which the scattering matrix can quickly be found. Short arrows show the direction of particle motion; long arrows show the direction of propagation (redraw from [28]).

Elements in scattering matrix are given by [28]:

$$\overset{\backslash}{P}\overset{/}{P} = \left[ \left( b \frac{\cos i_1}{\alpha_1} - c \frac{\cos i_2}{\alpha_2} \right) F - \left( a + d \frac{\cos i_1}{\alpha_1} \frac{\cos j_2}{\beta_2} \right) H p^2 \right] / D,$$

$$\overset{\backslash}{P}\overset{/}{S} = -2 \frac{\cos i_1}{\alpha_1} \left( ab + cd \frac{\cos i_2}{\alpha_2} \frac{\cos j_2}{\beta_2} \right) p \alpha_1 / (\beta_1 D),$$

$$\overset{\backslash}{P}\overset{\backslash}{P} = 2 \rho_1 \frac{\cos i_1}{\alpha_1} F \alpha_1 / (\alpha_2 D),$$

$$\overset{\backslash}{P}\overset{\backslash}{S} = 2 \rho_1 \frac{\cos i_1}{\alpha_1} H p \alpha_1 / (\beta_2 D),$$

$$\overset{\backslash}{S} \overset{/}{P} = -2 \frac{\cos j_1}{\beta_1} (ab + cd \frac{\cos i_2}{\alpha_2} \frac{\cos j_2}{\beta_2}) p \beta_1 / (\alpha_1 D),$$

$$\overset{\backslash}{S} \overset{/}{S} = -[(b \frac{\cos j_1}{\beta_1} - c \frac{\cos j_2}{\beta_2}) E - (a + d \frac{\cos i_2}{\alpha_2} \frac{\cos j_1}{\beta_1}) G p^2] / D,$$

$$\overset{\backslash}{S} \overset{\backslash}{P} = -2 \rho_1 \frac{\cos j_1}{\beta_1} G p \beta_1 / (\alpha_2 D),$$

$$\overset{\backslash}{S} \overset{\backslash}{S} = 2 \rho_1 \frac{\cos j_1}{\beta_1} E \beta_1 / (\beta_2 D),$$

$$\overset{/}{P} \overset{/}{P} = 2 \rho_2 \frac{\cos i_2}{\alpha_2} F \alpha_2 / (\alpha_1 D),$$

$$\overset{/}{P} \overset{/}{S} = -2 \rho_2 \frac{\cos i_2}{\alpha_2} G p \alpha_2 / (\beta_1 D),$$

$$\overset{/}{P} \overset{\backslash}{P} = -[(b \frac{\cos i_1}{\alpha_1} - c \frac{\cos i_2}{\alpha_2}) F + (a + d \frac{\cos i_2}{\alpha_2} \frac{\cos j_1}{\beta_1}) G p^2] / D,$$

$$\overset{/}{P} \overset{\backslash}{S} = 2 \frac{\cos j_2}{\alpha_2} (ac + bd \frac{\cos i_1}{\alpha_1} \frac{\cos j_1}{\beta_1}) p \alpha_2 / (\beta_2 D),$$

$$\overset{/}{S} \overset{/}{P} = 2 \rho_2 \frac{\cos j_2}{\beta_2} H p \beta_2 / (\alpha_1 D),$$

$$\overset{/}{S} \overset{/}{S} = 2 \rho_2 \frac{\cos j_2}{\beta_2} E \beta_2 / (\beta_1 D),$$

$$\overset{/}{S} \overset{\backslash}{P} = 2 \frac{\cos j_2}{\beta_2} (ac + bd \frac{\cos i_1}{\alpha_1} \frac{\cos j_1}{\beta_1}) p \beta_2 / (\alpha_2 D),$$

$$\hat{S} \hat{S} = [(b \frac{\cos j_1}{\beta_1} - c \frac{\cos j_2}{\beta_2})E + (a + d \frac{\cos i_1}{\alpha_1} \frac{\cos j_2}{\beta_2})Hp^2] / D,$$

where

$$a = \rho_2(1 - 2\beta_2^2 p^2) - \rho_1(1 - 2\beta_1^2 p^2),$$

$$b = \rho_2(1 - 2\beta_2^2 p^2) + 2\rho_1\beta_1^2 p^2,$$

$$c = \rho_1(1 - 2\beta_2^2 p^2) + 2\rho_2\beta_2^2 p^2,$$

$$d = 2(\rho_2\beta_2^2 - \rho_1\beta_1^2),$$

$$E = b \frac{\cos i_1}{\alpha_1} + c \frac{\cos i_2}{\alpha_2},$$

$$F = b \frac{\cos j_1}{\beta_1} + c \frac{\cos j_2}{\beta_2},$$

$$G = a - d \frac{\cos i_1}{\alpha_1} \frac{\cos j_2}{\beta_2},$$

$$H = a - d \frac{\cos i_2}{\alpha_2} \frac{\cos j_1}{\beta_1},$$

$$D = EF + GHp^2. \quad \text{Equation A-18}$$

#### A.2.4 P-SV Wave Incident on a Solid-Fluid Interface

The scattering of a P-SV wave at a solid-fluid interface can be described by eliminating the fourth row and fourth column of the previous matrix, because S waves do not propagate in a fluid.

A convenient way to obtain the solid-fluid P-SV scattering matrix is to use the welded interface P-

SV scattering matrix, but set the shear wave speed in the fluid medium equal to 0. This method was proposed by B.L.N.Kennett [34], which was developed to avoid additional derivation.

### A.3 Reflection and Transmission of Plane Waves in a Layered System

For waves propagating in a layered medium, the effect of interface and the thickness of each layer must be taken into account when studying changes in amplitude, phase and wave speed.

First only the effect of a welded interface between two half spaces on a propagating wave is considered. The D denotes the downgoing wave and U denotes the upgoing wave. r and t are the reflection and transmission coefficients.

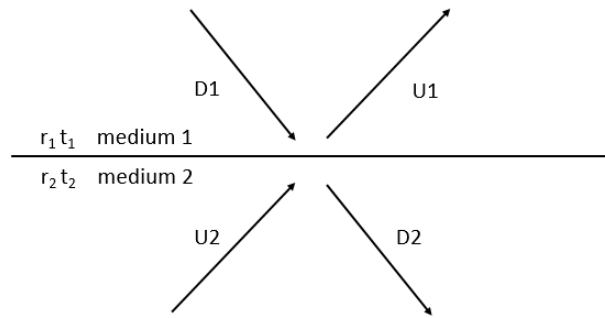


Figure A.3 Incident and scattered plane waves across two half spaces and one welded interface.

From Figure A.3:

$$U_1 = t_2 * U_2 + r_1 * D_1,$$

$$D_2 = r_2 * U_2 + t_1 * D_1, \quad \text{Equation A-19}$$

where U1, U2, D1 and D2 represented the upgoing and downgoing waves. Rearranging, the matrix form is

$$\begin{pmatrix} -t_2 & 0 \\ -r_2 & 1 \end{pmatrix} \begin{pmatrix} U_2 \\ D_2 \end{pmatrix} = \begin{pmatrix} -1 & r_1 \\ 0 & t_1 \end{pmatrix} \begin{pmatrix} U_1 \\ D_1 \end{pmatrix}, \quad \text{Equation A-20}$$

From the relation  $t_1 * t_2 - r_1 * r_2 = 1$  and  $r_1 = -r_2$ ,

finally,

$$\begin{pmatrix} U_2 \\ D_2 \end{pmatrix} = 1/t_2 \begin{pmatrix} 1 & r_2 \\ r_2 & 1 \end{pmatrix} \begin{pmatrix} U_1 \\ D_1 \end{pmatrix}. \quad \text{Equation A-21}$$

Next, the influence of the layer thickness is considered (Figure A.4). A phase shift is required to account for layer with thickness,  $h$ . Let  $Z=e^{i\omega T}$ , where  $T=h\cos j/\beta$  is the two-way travel time, multiplication by  $\sqrt{z}$  is equivalent to delaying a function by  $T/2$ , the travel time across the layer.

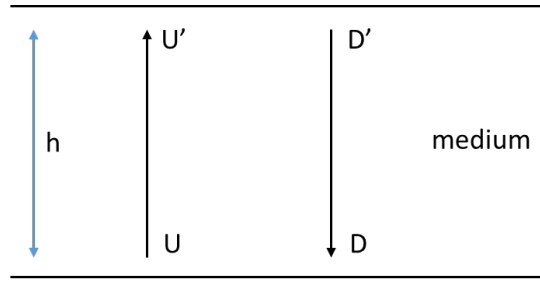


Figure A.4 Waves travel through the medium.

Using primed letters to denote the waves that travel through the entire layer but have not reach the interface, the following relation can be obtained:

$$\begin{pmatrix} U' \\ D' \end{pmatrix} = \begin{pmatrix} 1/\sqrt{z} & 0 \\ 0 & \sqrt{z} \end{pmatrix} \begin{pmatrix} U \\ D \end{pmatrix}. \quad \text{Equation A-22}$$

Combine this with the previous relation (2.21):

$$\begin{pmatrix} U_2 \\ D_2 \end{pmatrix} = \frac{1}{\sqrt{z}t_2} \begin{pmatrix} 1 & r_2z \\ r_2 & 1 \end{pmatrix} \begin{pmatrix} U_1 \\ D_1 \end{pmatrix}, \quad \text{Equation A-23}$$

Or:

$$\begin{pmatrix} U_1 \\ D_1 \end{pmatrix} = \frac{1}{t_1} \begin{pmatrix} 1 & t_2 \\ r_1 & 1 \end{pmatrix} \begin{pmatrix} 1/\sqrt{z} & 0 \\ 0 & \sqrt{z} \end{pmatrix} \begin{pmatrix} U_2 \\ D_2 \end{pmatrix} = M \begin{pmatrix} U_2 \\ D_2 \end{pmatrix}. \quad \text{Equation A-24}$$

Therefore, for a system with k layers, the reflected and transmitted waves are obtained by substituting  $U_k D_k$  in to equation A.3-6. Note there are k layers, k+1 interface and k+2 media:

$$\begin{pmatrix} U_1 \\ D_1 \end{pmatrix} = M_1 M_2 \dots M_k \begin{pmatrix} 1 & t_{k+1} \\ r_{k+1} & 1 \end{pmatrix} \begin{pmatrix} U_{k+2} \\ D_{k+2} \end{pmatrix} = M \begin{pmatrix} U_{k+2} \\ D_{k+2} \end{pmatrix}, \quad \text{Equation A-25}$$

where  $M = M_1 M_2 \dots M_{k+1}$ .

If there is only a downgoing wave incident from the top and no upgoing wave incident from the bottom, then

$$\begin{pmatrix} U_1 \\ D_1 \end{pmatrix} = M \begin{pmatrix} 0 \\ D_{k+2} \end{pmatrix}. \quad \text{Equation A-26}$$

Therefore, the reflection and transmission coefficients are:

$$R = \frac{U_1}{D_1} = \frac{M_{12}}{M_{22}}, \quad \text{Equation A-27}$$

$$T = \frac{D_{k+2}}{D_1} = \frac{1}{M_{22}}. \quad \text{Equation A-28}$$

#### A.4 SH Wave Propagation in a Layered System

Only solid layers with welded interface boundary conditions are considered because an S wave cannot travel in a fluid. Consider an upgoing SH wave incident from the bottom of the layered system and a downgoing SH wave incident from the top of the system. The condition would be exactly the same as the general case discussed above in section A.2.4. Thus, for a k layers system:

$$M_k = \frac{1}{\begin{matrix} \backslash & / \\ S & S_k \end{matrix}} \begin{pmatrix} 1 & \begin{matrix} / & / \\ S & S_k \end{matrix} \\ \begin{matrix} \backslash & / \\ S & S_k \end{matrix} & 1 \end{pmatrix} \begin{pmatrix} 1/\sqrt{z} & 0 \\ 0 & \sqrt{z} \end{pmatrix}, \quad \text{Equation A-29}$$

$$M = M_1 M_2 \dots M_{k+1},$$

$$R = \frac{U_1}{D_1} = \frac{M_{12}}{M_{22}}, \quad \text{Equation A-30}$$

$$T = \frac{D_{k+2}}{D_1} = \frac{1}{M_{22}}. \quad \text{Equation A-31}$$

### A.5 P-SV Wave Propagation in a Layered System

For P-SV wave propagation, the situation is more complicated. There will be P wave and SV wave conversions at an interface. Since the result for solid-fluid boundary conditions can be obtained by setting the S wave velocity in the fluid medium equal to zero, the derivation starts with the welded interface boundary condition. First consider only one layer:

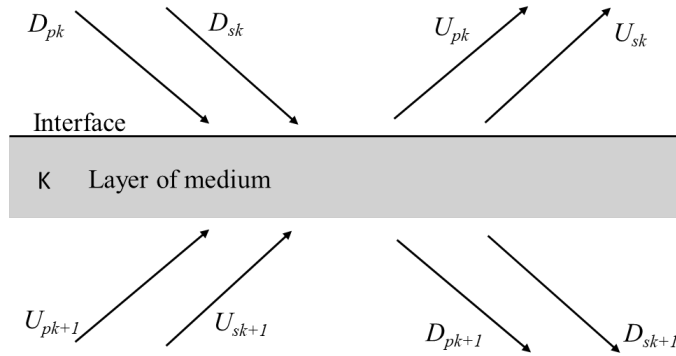


Figure A.5 Complete components for possible incident P-SV waves with reflection and transmission.

When the wave interacts with an interface and travels through one layer,

$$\begin{pmatrix} D_{pk} \\ D_{sk} \\ U_{pk} \\ U_{sk} \end{pmatrix} = M_k \begin{pmatrix} D_{pk+1} \\ D_{sk+1} \\ U_{pk+1} \\ U_{sk+1} \end{pmatrix}. \quad \text{Equation A-32}$$

Given the reflection and transmission coefficients and phase delay caused by the layer ( $Z=e^{i\delta pk}$ ,  $\delta pk=wh\cos i_{k+1}$ ), the following relationships are obtained:



$$M_k(3,3) = (PP(SPPS-SSPP) + SP(PSP-PPPS) + PP(PSS-SSP))e^{i\delta_k} / (PSS-SSP),$$

$$M_k(3,4) = (PP(SPSS-SSSP) + SP(PSSP-SSPP) + SP(PSS-SSP))e^{i\delta_k} / (PSS-SSP),$$

$$M_k(4,1) = (PSSS-SSPS)e^{i\delta_k} / (PSS-SSP),$$

$$M_k(4,2) = (SSPP-PSSP)e^{i\delta_k} / (PSS-SSP),$$

$$M_k(4,3) = (PS(SPPS-SSPP) + SS(PSP-PPPS) + PS(PSS-SSP))e^{i\delta_k} / (PSS-SSP),$$

$$M_k(4,4) = (PS(SPSS-SSSP) + SS(PSSP-SSPP) + SS(PSS-SSP))e^{i\delta_k} / (PSS-SSP),$$

$$\delta_{pk} = \omega h_k \cos(i_k) / \alpha_k \quad \delta_{sk} = \omega h_k \cos(j_k) / \beta_k. \quad \text{Equation A-34}$$

For waves on the both side of the last interface,  $M_{k+1}$  is the same as  $M_k$  except  $\delta_{pk+1}$  and  $\delta_{sk+1}$  are zero.

Therefore, for a system with k layers:

$$\begin{pmatrix} D_{p1} \\ D_{s1} \\ U_{p1} \\ U_{s1} \end{pmatrix} = M_1 M_2 \dots M_k M_{k+1} \begin{pmatrix} D_{pk+2} \\ D_{sk+2} \\ U_{pk+2} \\ U_{sk+2} \end{pmatrix} = M_k \begin{pmatrix} D_{pk+2} \\ D_{sk+2} \\ U_{pk+2} \\ U_{sk+2} \end{pmatrix}. \quad \text{Equation A-35}$$

When only a P wave incident on the top of the system is considered, then:

$$D_{p1} = M(1,1)D_{pk+2} + M(1,2)D_{sk+2},$$

$$0 = M(2,1)D_{pk+2} + M(2,2)D_{sk+2}. \quad \text{Equation A-36}$$

Hence the transmission coefficients for P-P and P-SV waves are given by:

$$t_{pp} = D_{pk+2} / D_{p1} = -M(2,2) / (M(1,2)M(2,1) - M(1,1)M(2,2)),$$

$$t_{psv} = D_{sk+2} / D_{p1} = M(2,1) / (M(1,2)M(2,1) - M(1,1)M(2,2)). \quad \text{Equation A-37}$$

The equations represent tpp and tpsv for the case of solid-fluid boundary condition case, just as in the laboratory experiments (see Chapter 3).

## **APPENDIX B. IMAGES SHOWING EXPERIMENT REPEATABILITY**

The following images are fracture area fraction of different concentration fluids in terms of Solution 1 by weight over time with different variables.

For non-reactive mixing at different inclination angles (Section 3.3.1.1):

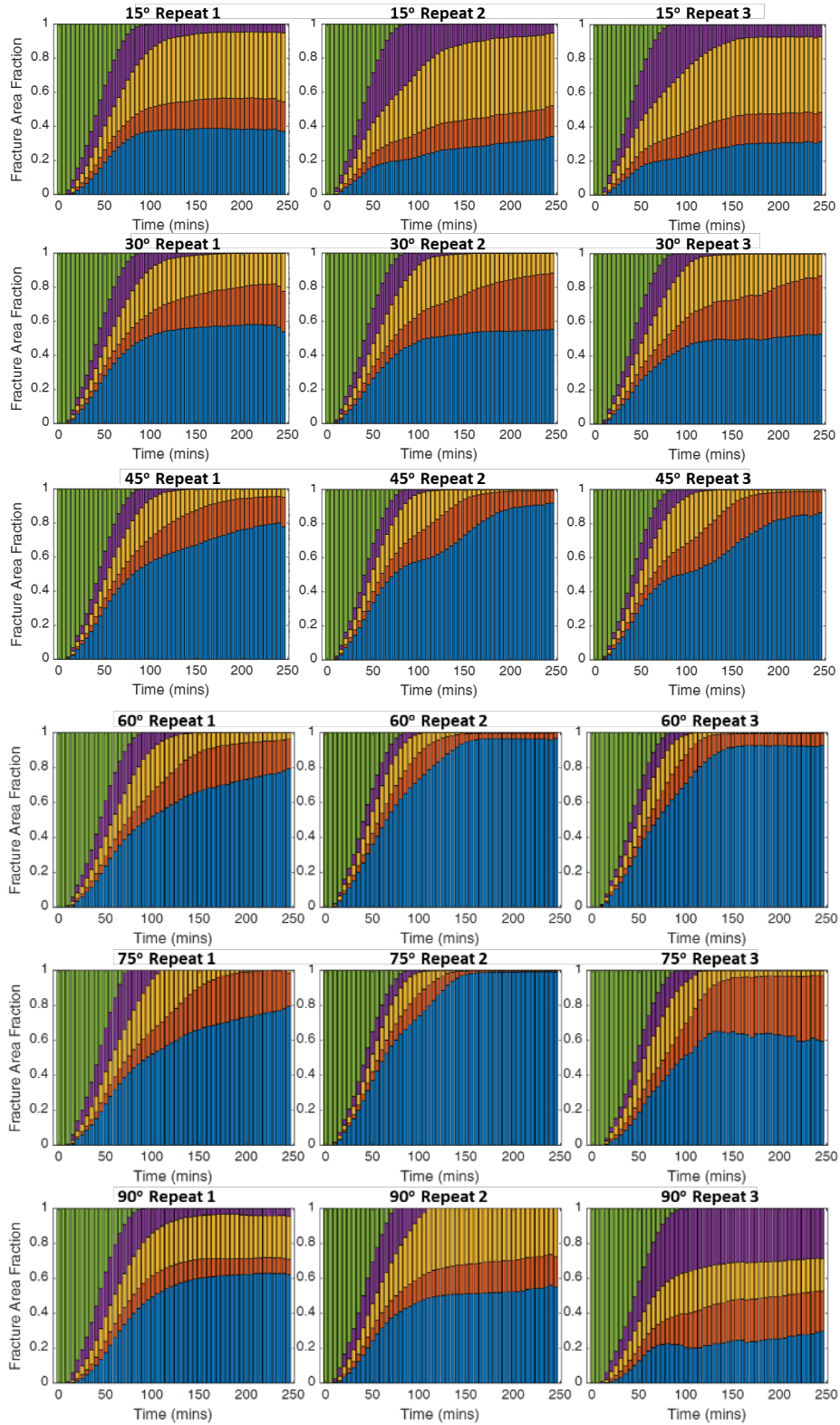


Figure B.1 Fracture area fraction of different concentration fluids in terms of Solution 1 by weight over time for different inclination angles. Aperture is 2 mm; pumping rate is 0.17 ml/min for both Solution 1 and 2; density contrast is 1111/1031.8.

For non-reactive mixing at different apertures (Section 3.3.2.1):

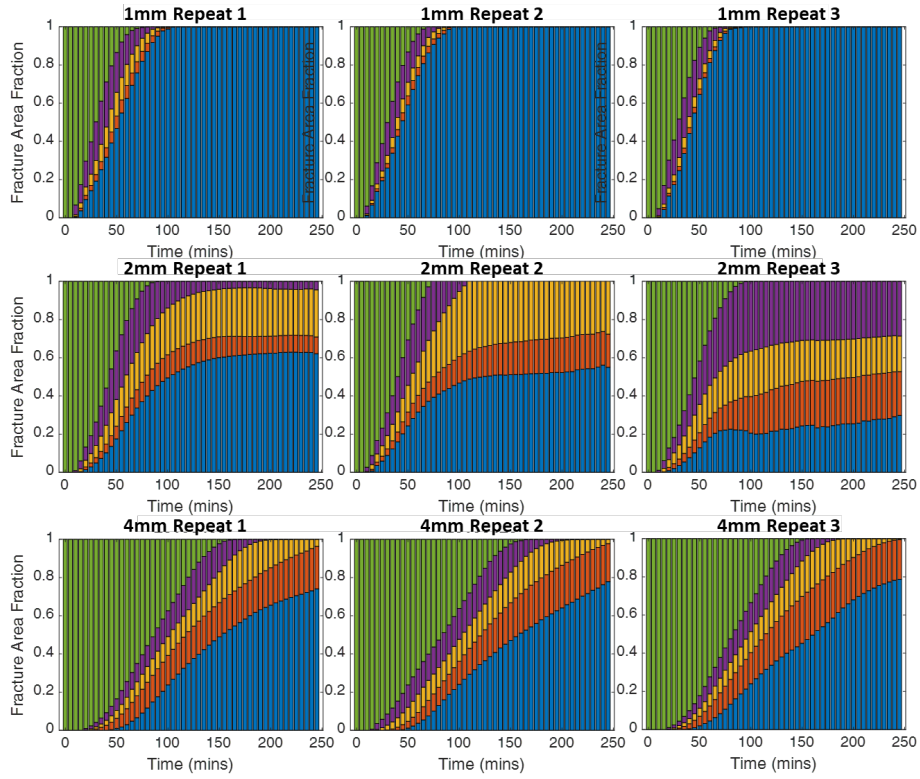


Figure B.2 Fracture area fraction of different concentration fluids in terms of Solution 1 by weight over time for different apertures. Inclination angle is  $90^\circ$ ; pumping rate is 0.17 ml/min for both Solution 1 and 2; density contrast is 1111/1031.8.

For non-reactive mixing at different pumping rate (Section 3.3.4):

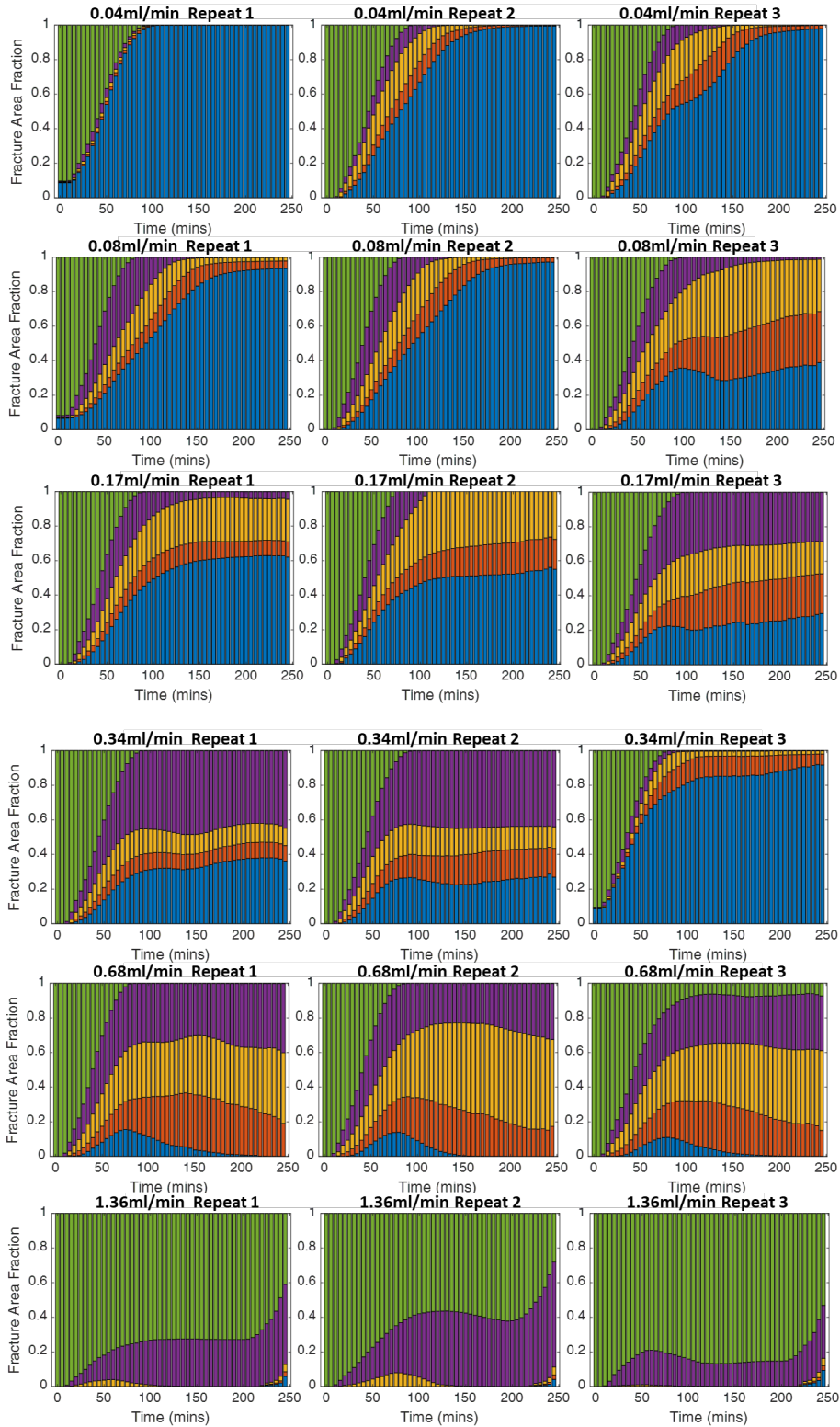


Figure B.3 Fracture area fraction of different concentration fluids in terms of Solution 1 by weight over time for different pumping rates of Solution 2. Inclination angle is 90o; aperture is 2 mm; pumping rate is 0.17 ml/min for Solution 1; density contrast is 1111/1031.8.

## APPENDIX C. OTHER MEASUREMENTS OF FLUIDS PROPERTIES

### METHODS FOR MEASURING VISCOSITY

AR-G2 rheometer (TA Instruments) was used to measure the viscosity of the fluids. Cone plate was used in the test. 8 solutions each with 30 ml volumes were prepared for the measurement.

Detailed procedure can be found at

[https://cse.wvu.edu/files/AMSEC/Instrumentation/Rheometer\\_SOPs.pdf](https://cse.wvu.edu/files/AMSEC/Instrumentation/Rheometer_SOPs.pdf)

The solutions' components and viscosities are:

Table C.1 Component and viscosity measurement of different solutions

<b>Solution number</b>	<b>Component</b>	<b>viscosity (Pa-s)</b>
1	CaCl <sub>2</sub> *2H <sub>2</sub> O (14.7g), H <sub>2</sub> O (96.4g)	1.23x10 <sup>-3</sup>
2	CaCl <sub>2</sub> *2H <sub>2</sub> O (14.7g), H <sub>2</sub> O (96.4g), Bromocresol purple (0.03g)	1.19x10 <sup>-3</sup>
3	Na <sub>2</sub> CO <sub>3</sub> (11.1g), H <sub>2</sub> O (100g)	1.57x10 <sup>-3</sup>
4	Na <sub>2</sub> CO <sub>3</sub> (11.1g), H <sub>2</sub> O (100g), Bromocresol green (0.03g)	1.63x10 <sup>-3</sup>
5	Na <sub>2</sub> CO <sub>3</sub> (2.07g), NaCl (9g), H <sub>2</sub> O (100g),	1.19x10 <sup>-3</sup>
6	Na <sub>2</sub> CO <sub>3</sub> (2.07g), NaCl (9g), H <sub>2</sub> O (100g), Bromocresol green (0.03g)	1.20x10 <sup>-3</sup>
7	Na <sub>2</sub> CO <sub>3</sub> (3.18g), H <sub>2</sub> O (100g)	1.08x10 <sup>-3</sup>
8	Na <sub>2</sub> CO <sub>3</sub> (3.18g), H <sub>2</sub> O (100g), Bromocresol Green (0.03)	1.11x10 <sup>-3</sup>

### METHODS FOR MEASUREING INTERFACIAL TENSION

A CSC Scientific Tensiometer-Du Nouy (Figure C.1) was used to measure the interfacial tension between the fluid and air at 23°C. The procedures are: 1. Merge the platinum-iridium ring in the fluid in the Petri dish; 2. Lower the liquid sample table with the sample table adjusting screw; 3. When the ring is on the liquid surface and close to a break point, adjust the graduated dial until

the ring breaks up with fluid surface; 4. Record the dynes readings. Each fluid was measured 5 times. The results are listed below:

Table C.2 Component and interface tension measurement of different solutions

Solution number	Component	Interface tension (dynes/cm)					Average (dynes/cm)
1	Na <sub>2</sub> CO <sub>3</sub> (3.18g), H <sub>2</sub> O (100g)	60.5	59.3	58.5	58.5	58.4	59.04
2	NaHCO <sub>3</sub> (5.04g), H <sub>2</sub> O (100g)	66.0	63.9	64.3	65.0	62.0	64.24
3	CaCl <sub>2</sub> *2H <sub>2</sub> O (14.7g), H <sub>2</sub> O (96.4g)	69.6	68.8	69.3	68.7	68.0	68.88



Figure C.1 CSC Scientific Tensiometer-Du Nouy

## REFERENCES

1. Weart, S. *The Carbon Dioxide Greenhouse Effect*. Available from: <https://history.aip.org/climate/co2.htm>.
2. Change, U.N.F.C.o.C. *Summary of the Paris Agreement*. Available from: <http://bigpicture.unfccc.int/#content-the-paris-agreemen>.
3. INSTITUTE, G.C., *THE GLOBAL STATUS OF CCS | 2016 SUMMARY REPORT*. 2006.
4. Wikipedia. *Carbon sequestration*. Available from: [https://en.wikipedia.org/wiki/Carbon\\_sequestration](https://en.wikipedia.org/wiki/Carbon_sequestration).
5. Juerg M. Matter, M.S., Sandra Ó. Snæbjörnsdóttir, Eric H. Oelkers, Martin Stute, Sandra Ó. Snæbjörnsdóttir, Eric H. Oelkers, and E.S.A. Sigurdur R. Gislason, Bergur Sigfusson, Ingvi Gunnarsson, Holmfrídur Sigurdardóttir, Einar Gunnlaugsson, Gudni Axelsson, Helgi A. Alfredsson, Domenik Wolff-Boenisch, Kiflom Mesfin, Diana Fernandez de la Reguera Taya, Jennifer Hall, Knud Dideriksen, Wallace S. Broecker, *Rapid carbon mineralization for permanent disposal of anthropogenic carbon dioxide emissions*. *Science*, 2016. **352**(6291).
6. Laubach, S.E. and M.E. Ward, *Diagenesis in porosity evolution of opening-mode fractures, Middle Triassic to Lower Jurassic La Boca Formation, NE Mexico*. *Tectonophysics*, 2006. **419**(1-4): p. 75-97.
7. Appold, M.S., et al., *Numerical modeling of the origin of calcite mineralization in the Refugio-Carneros fault, Santa Barbara Basin, California*. *Geofluids*, 2007. **7**(1): p. 79-95.
8. Eichhubl, P., N.C. Davatzes, and S.P. Becker, *Structural and diagenetic control of fluid migration and cementation along the Moab fault, Utah*. *AAPG Bulletin*, 2009. **93**: p. 653-681.
9. Hopkins, D.L., N.G.W. Cook, and L.R. Myer, *Normal joint stiffness as a function of spatial geometry and surface roughness*. In *International Symposium on Rock Joints*. Loen, Norway, 1990.
10. Kendal, K. and D. Tabor, *An ultrasonic study of the area of contact between stationary and sliding surfaces*. *Proceedings of the Royal Society of London. A. Mathematical and Physical Sciences*, 1971. **323**(1554): p. 321-340.
11. Dijk, P. and B. Berkowitz, *Precipitation and dissolution of reactive solutes in fractures*. *Water resources research*, 1998. **34**: p. 457-470.
12. Zhao, C., et al., *Mineral precipitation associated with vertical fault zones: the interaction of solute advection, diffusion and chemical kinetics*. *Geofluids*, 2007. **7**(1): p. 3-18.

13. Cao, P., Z.T. Karpyn, and L. Li, *Self-healing of cement fractures under dynamic flow of CO<sub>2</sub>-rich brine*. Water Resources Research, 2015. **51**: p. 4684-4701.
14. Luquot, L., H. Abdoulghafour, and P. Gouze, *Hydro-dynamically controlled alteration of fractured Portland cements flowed by CO<sub>2</sub>-rich brine*. International Journal of Greenhouse Gas Control, 2013. **16**: p. 167-179.
15. Arvidson, R.S. and F. Mackenzie, *The dolomite problem; control of precipitation kinetics by temperature and saturation state*. American Journal of Science, 1999. **299**: p. 257-288.
16. Kull, H.J., *Theory of the Rayleigh-Taylor instability*. Physics Reports, 1991. **206**(5): p. 197-325.
17. Tchelepi, H.A., *Viscous fingering, gravity segregation and permeability heterogeneity in two-dimensional and three dimensional flows*, in *Department of Petroleum Engineering*. 1994, Stanford University.
18. Sahu, K.C., et al., *Linear stability analysis and numerical simulation of miscible channel flows*. Physics of Fluids, 2009. **21**(042104).
19. Pouliquen, O., J.M. Chomaz, and P. Huerre, *Propagating Hombœ waves at the interface between two immiscible fluids*. J. Fluid Mech, 1994. **266**(277).
20. Cushman-Roisin, B., *Environmental Fluid Mechanics*. 2014: John Wiley & Sons, Inc.
21. Sahu, K.C., et al., *Pressure-driven miscible two-fluid channel flow with density gradients*. PHYSICS OF FLUIDS, 2009. **21**(043603).
22. Inc, C.T. *What are Castable Urethane Elastomers?* ; Available from: <http://www.crosslinktech.com/articles/what-are-castable-urethane-elastomers.html>.
23. Meignin, L., et al., *Gap size effects for the Kelvin-Helmholtz instability in a Hele-Shaw cell*. Physical Review E, 2001. **64**(2).
24. Emmanuel, S. and B. Berkowitz, *Mixing-induced precipitation and porosity evolution in porous media*. Advances in Water Resources, 2005. **28**(4): p. 337-344.
25. Fernandez, J., et al., *Wavelength selection of fingering instability inside Hele-Shaw cells*. Physics of Fluids, 2001. **13**(11): p. 3120.
26. Wikipedia. *Beer-Lambert law*. Available from: [https://en.wikipedia.org/wiki/Beer%E2%80%93Lambert\\_law](https://en.wikipedia.org/wiki/Beer%E2%80%93Lambert_law).
27. Acosta-Colon, A., L.J. Pyrak-Nolte, and M. Olander. *Seismic Response of In-filled Fractures*. in *American Geophysical Union, Fall Meeting 2008*. 2008.

28. Aki, K. and P.G. Richards, *Quantitative Seismology second edition*. 2009.
29. Mavko, G.; Available from:  
<https://pangea.stanford.edu/courses/gp262/Notes/5.Elasticity.pdf>.
30. Schoenberg, M., *Elastic wave behavior across linear slip interfaces*. Journal of the acoustical society of america, 1980. **68**(5).
31. Pyrak-Nolte, L.J., L.R. Myer, and N.G.W. Cook, *Transmission of seismic waves across single natural fractures*. Journal of Geophysical Research, 1990. **95**(B6).
32. Pyrak-Nolte, L.J., B. Abell, and S. Shao, *Elastic Wave Propagation in Fractured Anisotropic Media Chapter 11*. Rock Mechanics and Engineering Volume 1: Principles. 2016.
33. Nowack, R.L. *Introduction to Seismology*. Available from:  
<http://web.ics.purdue.edu/~nowack/geos557/lecture13a-dir/lecture13a.htm>.
34. Kennett, B.L.N., *The seismic wavefield volume 1: introduction and theoretical development*. 2001. 256.